Elucidating the Structural Dynamics of Muscle Myosin Using Novel Methods in Electron Paramagnetic Resonance

A DISSERTATION
SUBMITTED TO THE FACULTY OF THE GRADUATE SCHOOL
OF THE UNIVERSITY OF MINNESOTA
BY

Benjamin Paul Binder

IN PARTIAL FULFILLMENT OF THE REQUIREMENTS
FOR THE DEGREE OF
DOCTOR OF PHILOSOPHY

David D. Thomas, Advisor

November, 2016

ACKNOWLEDGEMENTS

Throughout these past five years, I have been blessed beyond measure with truly exceptional company. Without a doubt, this work could not have been completed without the enduring support and crucial assistance of many outstanding individuals—my cherished friends, mentors, and colleagues. To do them all justice, I'd need another volume with a thicker spine than this one; I'll try to make do with a few pages here at the start.

First mention goes to my redoubtable PI and thesis advisor, **Dr. David D. Thomas**. Dave is a fellow clarinet player, so his position at the top of this section was naturally guaranteed from the start—but during my years in graduate school, I have grown to appreciate him for so much more than a shared love of music. Many have remarked on Dave's unwavering investment in his students, and I am proud to say I have experienced that investment firsthand. His commitment to mentorship is nothing short of superhuman, and I will never forget the countless hours he spent with me one-on-one, as we slowly beat the essence of my project into being together. Dave has taught me how to be a better scientist in every regard, and I will endeavor to take his lessons to heart. Dave: thank you for inviting me into this family, and raising me well.

To **Dr. Meg Titus**, chair of my thesis committee, I also owe immense thanks. I have known Meg as a camp counselor, course instructor, scientific collaborator, and trusted advisor, and I have never met a more compelling role model for any of these positions. Meg has played a vital part in every phase of my graduate career, and at every point, she has inspired

me to do better. Meg: thank you for all the chats, the wisdom, and the resources—and above all, thank you, sincerely, for the care with which these gifts were given.

Many thanks as well to **Dr. Deb Ferrington**, and **Dr. Joe Metzger** for sticking with me on my committee to the bitter end—your thoughtful comments through the years have challenged and shaped me, and I am grateful for everything you've done to help prepare me for the world of science.

I would never have started this journey in the first place without outstanding undergraduate mentors, and here I want to especially thank **Dr. Laura Listenberger** and **Dr. Jenny Klein**. Laura, your support and encouragement helped me take the initiative to pursue research at the graduate level, and my experience in your lab gave me a solid foundation to meet the challenges I would find there. Jenny, without you I never would have found my place in the Thomas lab, and our chats during those first years were invaluable in helping me settle in.

I've had the privilege of working with some of the greatest labmates in the universe, and I'd be remiss not to acknowledge them as well. First and foremost, to **Dr. Rebecca Moen** and **Dr. Ryan Mello**: huge thanks for your mentorship in those first months, and your ongoing support and friendship afterwards. I couldn't have asked for better emissaries from the realm of biophysics. Thanks also to **Dr. Jesse McCaffrey** and **Dr. Zach James** for (mostly) keeping me out of trouble on the EPR magnets during my first few years, and also to **Dr. Andrew Thompson** for dispelling the mysteries of DEER and agreeing to brave another BSL-related project with me. Of all the EPR vets, Jesse gets special mention for not

immediately abandoning me after I broke that dewar in front of him on my first solo run. To **Dr. Piyali Guhathakurta** and **Dr. Ewa Prochniewicz**, who shared their bench space and expansive knowledge of actin and myosin with me: thanks so much for your company and wisdom, as well as for putting up with my tendency to leave dishes everywhere. Thanks to **Dr. Robyn Rebbeck** as well, for helping me re-learn good technique in molecular biology, for sage advice on assembling my dissertation, and for all the tea.

There are a huge number of names I should list among my contemporaries in the graduate program, but here I especially want to thank **Jonathan Crain**, **Mike Fealey**, **Peter Martin**, and **Yahor Savich**, who have all given me unique and crucial support. Jonathan, thanks for affirming that science isn't just a means to an end, and that a balanced life is worth fighting for. Mike, thanks for all the great conversations about teaching in science, especially how meticulously-crafted PowerPoint animations are totally worth it—can't wait to work together next semester. Peter, thanks for the many discussions over meals and coding sessions at Dogwood—I shudder to think what my computational approach would've looked like without your input. Yahor, thanks for taking up the mantle with such enthusiasm, and pushing forward into the next set of aims for this project. So many others deserve my thanks for productive discussions and solid friendship throughout my time here—especially **Megan McCarthy**, **Karl Petersen**, and **Sarah Nelson**.

During my graduate studies, it's also been my honor to work with some really exceptional undergraduate scientists in both the research lab and the classroom. I can't stress it enough—**Doug Deitchler**, **Katie Tuininga**, **Maram Essawy**, **Emily Ruan**, and **Livia**

Songster: you guys are the reason I'm in science. Thanks for helping to make me a better mentor, and godspeed on all your future endeavors.

The lab would surely cease to function—and I'd be short a fair number of dear friends—if not for the incredible staff and technicians working in the Thomas and Titus labs. **Sarah Blakely** and **Octavian Cornea**: thank you so much for accomplishing unimaginable feats behind the scenes every day just to keep us on track with grants, manuscripts, and orders. **Sinziana Cornea**, **Santiago Martinez**, and **Norma Jimenez Ramirez**: thank you for all your work in expressing and purifying so many of the proteins our lab depends on, especially the Dicty constructs that have been so vital to my work. **Holly Langer**, **Allison Hilgendorf**, **Corrin Laposki**, and **Meg Ryan**: thank you for always keeping everything so clean and well-stocked. **Kurt Peterson** and **Ben Grant**, thanks for making me feel welcome in the scary world of fluorescence, and thanks to Ben especially for his impeccable bonfire-lighting skills. Last but certainly not least, heartfelt thanks to **Samantha Yuen**, who, quite apart from her formidable skills in the wetlab, has fed each of us our weight in chocolate at least once within the last year alone. Sam, you've been a beacon of morale for us—thank you, sincerely, for all the food, company, and friendship.

To fellow grad students **Jaimee Hoefert**, **Jenny Mohn** and **Estella Yee**: we may be scattered to the four winds right now, but each of you has made a tremendous impact on my life during these last five years—thanks so much for the support, camaraderie, and love. To the Skull Mountain boys, **Tim Erkel**, **Alex Girard**, **Jeff Largent**, and **Will Roberts**: I would never have made it this far without your friendship—thanks for all the memories

in high school, Asheville, and beyond. And finally, to **Joe Funk**, my esteemed partner in cinema and lifelong friend since age 4: what can I possibly say, except here's to 24 more years of good times.

Finally, and most sincerely of all, I want to thank my family. These folks have provided respite, food, shelter, company, and inspiration for me during these five years, and for all the years that came before. Without a doubt, they have listened to more of my many frustrations and misgivings than anyone else could bear—and yet, through it all, they always did whatever they could to keep my spirits up. **Dawn**, **Paul**, and **Patrick Binder**: this work is dedicated to you.

DEDICATION

For Dawn, Paul, and Patrick

ABSTRACT

Muscle contraction is fundamentally driven by an interaction between two proteins: actin and myosin. Myosin is a molecular motor, and assumes the active role in this relationship, coupling energy from hydrolysis of ATP with conformational changes to generate force on actin. In the context of a muscle fiber, this force causes filaments of myosin and actin to slide past one another in an ordered lattice, drawing the ends of individual contractile units (called sarcomeres) together. Concerted shortening of sarcomeres along the length of a fiber results in large-scale shortening of the entire fiber.

Although muscle myosin has been the focus of intense study for many years, crucial details regarding its mechanism remain unknown. In particular, few structures of actin and myosin together have been reported—this is largely due to the inherent difficulties of handling large, filamentous protein complexes in traditional methods for structure determination. Myosin's interactions with actin are absolutely essential for macroscopic function, and this lack of structural information has created a knowledge gap: there is an abundance of functional and kinetic data for myosin in both normal and pathological states, but often no direct insight into the underlying structural causes for the observed behavior.

In the present work, I seek to address this knowledge gap by providing high-resolution insight into the structural states of actin-bound myosin. My work is based on the hypothesis

that allosteric coupling in myosin's catalytic domain (the domain responsible for actin binding, ATP hydrolysis, and initiation of force-generating conformational change) is accomplished via subtle internal rearrangements of individual structural elements. Furthermore, I hypothesize that these changes can be detected and quantified by innovative applications of site-directed spectroscopy. In Chapter 4, I establish a method using electron paramagnetic resonance (EPR) of a bifunctional spin label to probe nucleotide-dependent changes in the actomyosin complex. In Chapter 5, this method is expanded to include two complementary EPR techniques, ultimately providing sufficient constraints for direct modeling of nucleotide-dependent changes. Following these results, Chapter 6 addresses the ongoing development and further application of these methods within myosin and other protein systems.

TABLE OF CONTENTS

LIST OF TABLES

LIST OF FIGURES

List of Abbreviations

A	hyperfine coupling constant (or A-tensor)
$A'_{xx}, A'_{yy}, A'_{zz}$	A-tensor principle axis values
ADP	adenosine diphosphate
apo	nucleotide-free biochemical state
ATP	adenosine triphosphate
ATPase	adenosine triphosphatase
$\vec{B}$	magnetic field vector
B_0	magnetic field strength
B_{res}	resonance field position
BSL	bifunctional spin label
CD, S1dC	myosin catalytic domain
cryo-EM	cryo-electron microscopy
CW	continuous-wave
DEER	double electron-electron resonance
DHPR	dihydropyridine receptor
DTT	dithiothreitol
E	energy
EDTA	ethylenediaminetetraacetic acid
EGTA	ethylene glycol tetraacetic acid
EPR	electron paramagnetic resonance
F-actin	filamentous actin
FRET	Förster resonance energy transfer
FWHM	full width at half maximum
g	electron g-factor (or g-tensor)
$g'_{xx}, g'_{yy}, g'_{zz}$	g tensor principle axis values
h	Plank constant
$\hbar$	reduced Planck constant
$\mathcal{H}_{\text{EZ}}$	electron Zeeman interaction Hamiltonian
$\mathcal{H}_{\text{NZ}}$	nuclear Zeeman interaction Hamiltonian
$\mathcal{H}_{\text{HF}}$	nuclar hyperfine interaction Hamiltonian
HEPES	4-(2-hydroxyethyl)-1-piperazineethanesulfonic acid

HK	myosin helix K
HMM	heavy meromyosin
HW	myosin helix W
I	nuclear spin quantum number
$\vec{\hat{I}}$	nuclear spin operator
IASL	iodoacetamide spin label
K_{ATPase}	Michaelis-Menten constant for actin activation of myosin ATPase
L50	lower 50kDa domain
LCD	myosin light chain domain
LMM	light meromyosin
MD	molecular dynamics
m_I	nuclear magnetic moment quantum number
m_s	spin projection quantum number
MSL	maleimide spin label
MTS	methanethiosulfonate
MTSSL	methanethiosulfonate spin label
NADH	nicotinamide adenine dinucleotide
NMR	nuclear magnetic resonance
PLB	phospholamban
PSD	phase-sensitive detection
R	rotational diffusion tensor
RMD	restrained molecular dynamics
RyR	ryanodine receptor
$\vec{\hat{S}}$	electron spin operator
S1	subfragment-1
S2	subfragment-1
SDSL	site-directed spin labeling
SERCA	sarco(endo)plasmic reticulum calcium adenosine triphosphatase
SLE	stochastic Liouville equation
SR	sarcoplasmic reticulum
TCEP	tris(2-carboxyethyl)phosphine
TOAC	2,2,6,6-tetramethyl-N-oxyl-4-amino-4-carboxylic acid

U50	upper 50kDa domain
UV/Vis	ultraviolet/visual
V_0	EPR absorption spectrum
V_1	EPR derivative absorption spectum
$V_{\max}$	maximum enzymatic turnover rate
x_N, y_N, z_N	nitroxide frame coordinate axes
γ	gyromagnetic ratio
μ_B	Bohr magneton
$\vec{\mu}_s$	electron magnetic moment
ν	microwave frequency
nu_{pump}	pump frequency in DEER
nu_{pump}	observe frequency in DEER
θ_{AH}	tilt angle between actin and helix axes
θ_{NA}, ϕ_{NA}	polar angles of actin filament orientation in the nitroxide frame
θ_{NB}, ϕ_{NB}	polar angles of $\vec{B}$ in the nitroxide frame
θ_{NH}, ϕ_{NH}	polar angles of helix axis orientation in the nitroxide frame
τ_R	rotational correlation time

CHAPTER 1: MUSCLE ANATOMY AND PHYSIOLOGY

1.1 Muscle Types

The cellular anatomy of vertebrate muscle exhibits some of the greatest morphological specialization found in any tissue. As myocytes develop from their stem progenitors, they undergo a progressive maturation process that culminates in a fully integrated biological unit with a distinct muscle type and specific dimensions [1–3]. Skeletal myocytes mature into multinucleated, striated fibers that can be many inches in length, and respond primarily to signals from the somatic nervous system. Cardiac myocytes maintain their cell boundaries at maturity, but adopt a branched, fibrous morphology with gap junctions for rapid transference of electrochemical signals between cells. Smooth myocytes have a highly adaptive morphology that lacks regular striations, with contractile function instead delegated to a complex, disordered array within the cell interior. Of these three muscle types, skeletal muscle exhibits the greatest level of internal organization, with a macroscopic structure that approaches crystalline order along a fibers longitudinal axis.

1.2 Skeletal Muscle Cellular Anatomy

Mature, multinucleated skeletal myocytes are surrounded by a specialized plasma membrane known as the sarcolemma. Likewise, a highly specialized derivative of the endoplasmic reticulum, called the sarcoplasmic reticulum (SR), resides within the sarcolemma, spreading in a complex network along the radial periphery of the fiber that varies in form

according to the muscle type. Nuclei in healthy fibers are found on the periphery as well, as are mitochondria and other essential cellular organelles. The most distinctive structural feature of a mature muscle fiber is in the core, where a segmented, interdigitating array of polymeric protein filaments stretches along the length of the fiber. This array, known as the myofilament lattice, is responsible for driving the contractile function of skeletal and cardiac muscle tissue, and is composed primarily of two types of filaments: thin filaments containing F-actin and various associated regulatory proteins, and bipolar thick filaments composed primarily of myosin (Figure 1.1). The lattice is partitioned along its axis into individual contractile units called sarcomeres, which are organized by a variety of scaffolding and support proteins such that thin filaments are anchored at either end, and thick filaments are anchored in the center [4]. Individual muscle fibers bundle into distinct groups under the control of a single motor neuron; these motor units are activated asynchronously during a contraction event within the bulk tissue, allowing the relatively slow nerve stimulus rate to render smooth, sustained macroscopic motion [5]. Multipotent myocytes known as satellite cells remain dispersed throughout mature skeletal muscle tissue through adulthood, providing a means for repairing damage and for the generation of additional muscle fibers in hypertrophy [6].

1.3 Excitation-Contraction Coupling and Thin Filament Regulation

The initiation and actuation of muscle contraction on the cellular level is a complex and highly regulated series of events, beginning at the sarcolemma when an electrical impulse from an associated motor neuron depolarizes the membrane (Figure 1.2) [1, 7]. In both skeletal and cardiac muscle, deep invaginations in the sarcolemma occur at regular intervals along the fiber, bringing the membrane into close proximity with the SR, and thus providing a localized interface between the two organelles and their embedded proteins. Depolarization opens several voltage-gated channels embedded in the sarcolemma, including the dihydropyridine receptor (DHPR). In all muscle types, the immediate downstream effect of membrane depolarization is a rapid efflux of calcium ions from the SR, but the mechanism for this release varies depending on muscle type. In skeletal muscle, the DHPR is physically connected through binding interactions with a large calcium channel known as the ryanodine receptor (RyR), and membrane depolarization causes a conformational change in the DHPR that is allosterically coupled to an opening of the RyR. In cardiac muscle, there is no physical connection between the DHPR and RyR, and RyR opening is instead induced by a small but significant influx of calcium from the extracellular matrix through the DHPR, which is chelated by RyR-bound calmodulin proteins and causes the requisite conformational change (calcium-induced calcium release). In either case, the opening of the RyR causes a rapid spike in intracellular calcium, which diffuses into the core of the fiber to interact with the myofilament lattice.

Actin and myosin in the myofilament lattice readily associate in the absence of other

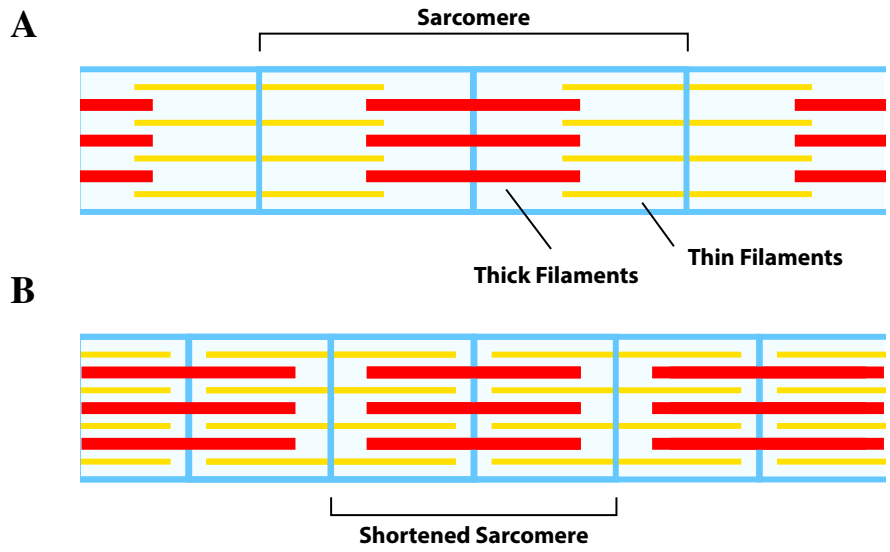

Figure 1.1. The contractile function of sarcomeres. A: Diagram of a muscle fiber in relaxation, with thick filaments (red) anchored in the center of each sarcomere, and thin filaments (yellow) anchored at the ends. B: The same muscle fiber in contraction, with sarcomere ends having been drawn together by repeated crossbridge cycling between thick and thin filaments.

regulatory proteins, but in a relaxed muscle fiber the binding site for myosin on actin is blocked by the troponin/tropomyosin complex on the thin filament (Figure 1.2). When troponin-C binds calcium, a subtle conformational shift is propagated along the length of the coiled-coil protein tropomyosin, causing it to shift its position relative to the actin polymer helix and exposing myosin-binding sites. Efficient mechanical contraction can thus begin, as myosin in the bipolar thick filaments successively binds and generates force on the actin in the thin filaments, drawing the opposing ends of the sarcomere together. Shortening sarcomeres along the length of the fiber leads to contraction of the entire fiber [8–10].

Muscle relaxation is accomplished by the depletion of calcium ions from the cytoplasm. This process is driven primarily by the sarco/endoplasmic reticulum calcium ATPase (SERCA), a calcium pump embedded in the SR: when stimulation of the RyR ceases, SERCA rapidly restores intracellular calcium to pre-activated levels, sequestering calcium back within the SR lumen. This causes the troponin/tropomyosin complex to release bound calcium and revert the thin filament to its blocked state. The activity of SERCA is carefully regulated in different tissues by the presence of regulatory binding partners, including phospholamban (PLB) in cardiac muscle. Unmodified phospholamban has an inhibitory effect on SERCA, but phosphorylation of phospholamban can relieve this inhibition. Thus, both contraction and relaxation processes are tied into a complex network of modulatory signaling pathways that adjust muscle activity due to environmental factors, endocrine stimulation, and resource availability.

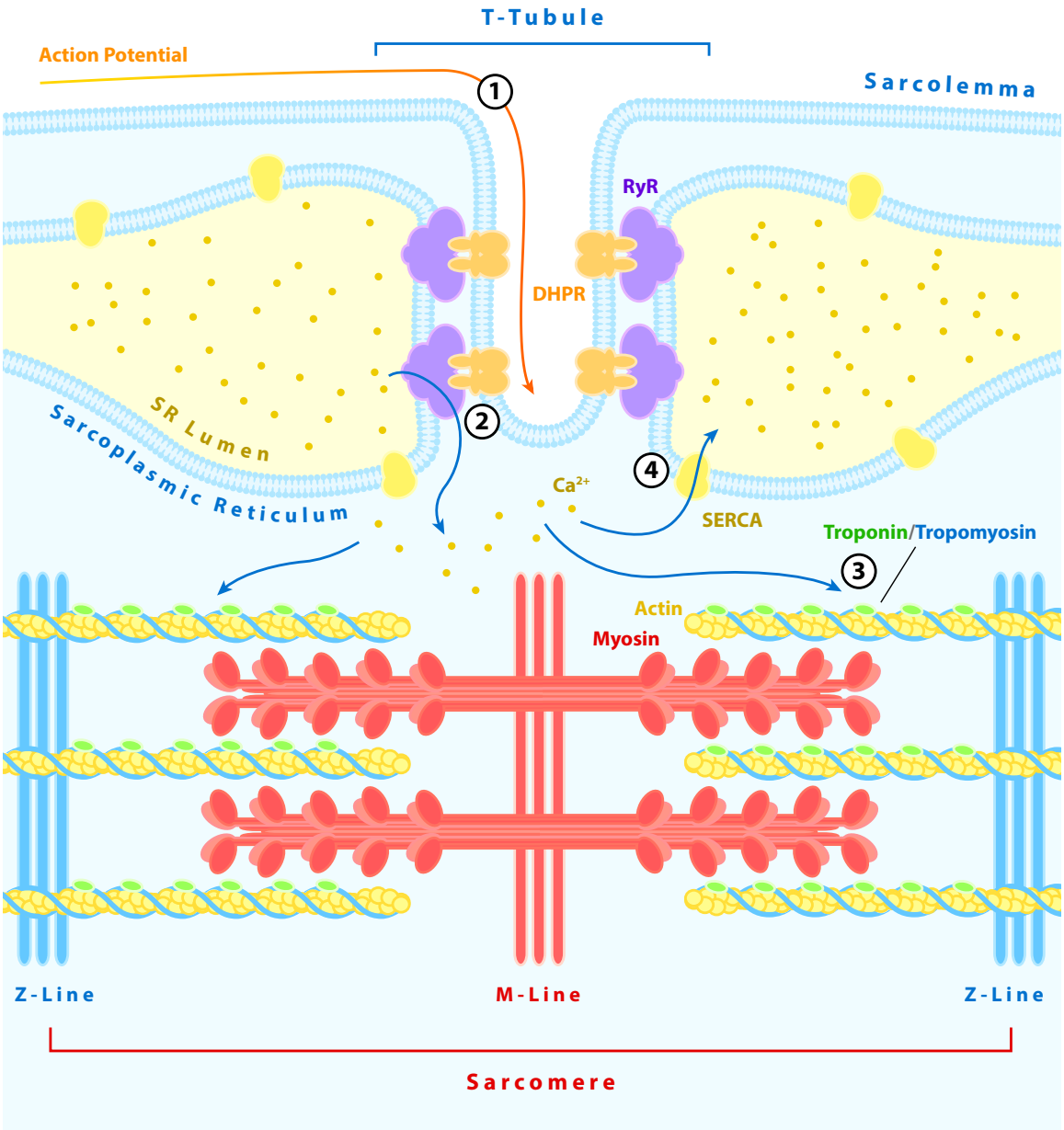

Figure 1.2. The major steps in excitation-contraction coupling. The diagram represents events that take place in a skeletal muscle fiber, starting with propagation of an action potential along the sarcolemma (1). The dihydropyridine receptor (orange) and ryanodine receptor (violet) mediate release of calcium from the sarcoplasmic reticulum (2), which induces a conformational shift in the troponin/tropomyosin complex (green/blue) on myofibrillar thin filaments (3). Myosin is subsequently able to bind, and contraction of the sarcomeres ensues. Calcium is re-sequestered mainly by SERCA, resulting in relaxation after neuronal stimulation ends (4).

CHAPTER 2: MYOSINS

2.1 Classes of Myosin

The myosins are a diverse family of actin-binding ATPase enzymes marked by their ability to transduce biochemical changes (e.g. the hydrolysis of nucleotide) into mechanical changes that serve a productive function within the cell. The myosin family currently contains 35 distinct classes of myosins, and while they are often generally labeled as molecular motors, there are many examples of both non-motile and motile classes [11–14]. The Class I myosins, for instance, are single-motor variants that may serve as membrane-associated tension-sensing anchors of variable strength, whereas the Class V and Class VI myosins dimerize to form processive transporters of cellular cargo [15–18]. ATPase activity, actin-binding affinity, and the presence or absence of auxiliary domains all demonstrate careful tuning of function through evolutionary mechanisms, resulting in a versatile collection of cytoskeletal proteins.

The best-studied myosins are of Class II, known often as "conventional" or muscle myosins. Class II myosins are composed of two dimerized heavy chains, and associated sets of two calmodulin-like light chains. The heavy chain includes a globular catalytic domain (CD) on its N-terminus with actin-binding loops and a P-type ATP-binding pocket; a light chain binding domain (LCD) with two IQ-binding motifs for the association of light chains; and a long α-helical rod domain that facilitates dimerization with another heavy chain and subsequent assembly of dimers into bipolar filaments (Figure 2.1). As

with most other myosins, the CD is responsible for the essential coupling of conventional myosins' ATPase cycle to actin binding, as well as for the transduction of chemical energy into mechanical work. The LCD functions mechanically as a lever arm, propagating subtle structural changes in the CD into a large arced rotation that ultimately generates sliding force between actin and myosin filaments.

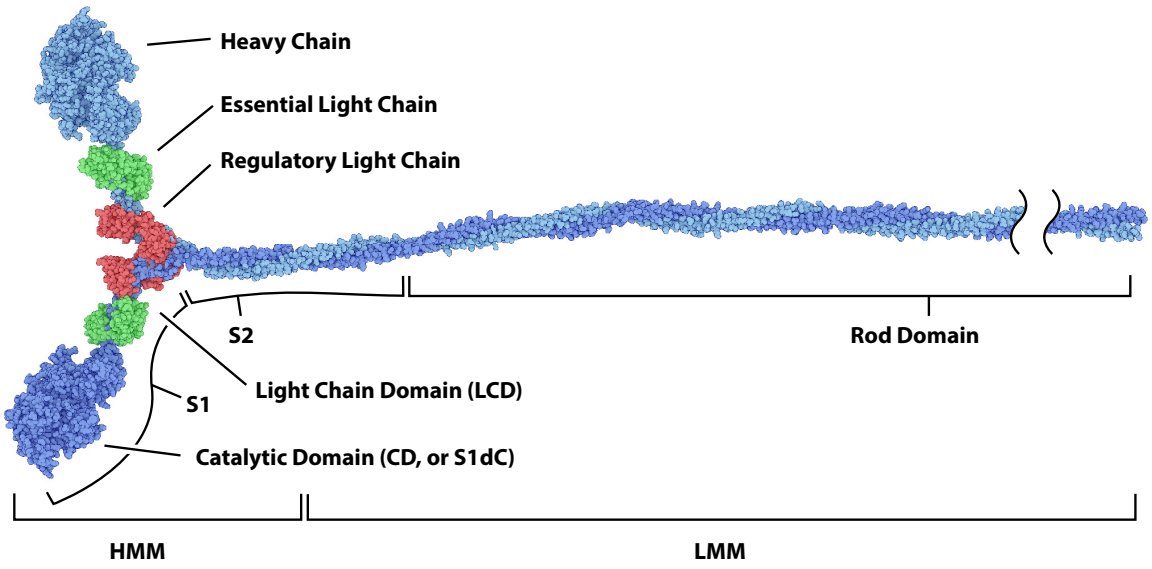

Figure 2.1. The structure of a typical Class II muscle myosin. Two dimerized heavy chains (light and dark blue) each bind an essential light chain (green) and a regulatory light chain (red). The heavy chain is broadly considered to have three functional domains: the catalytic, light chain, and rod domains (see labels below molecule). The heavy chain may also be divided into sections based on fragments obtained by enzymatic digestion. Tryptic digest yields two large fragments known as heavy meromyosin (HMM) and light meromyosin (LMM). Further digestion of HMM produces two subfragments, S1 (which contains the catalytic and light chain domains) and S2 (which contains the N-terminal portion of the rod domain, and is important for heavy chain dimerization). This model was built using elements from crystal coordinates 1MMA (catalytic domain) [19], 2BL0 (light chain domain and light chains) [20], 3JBH (heavy meromyosin) [21], and 2FXO (subfragment 2) [22]. Construction of the rod domain was based on the coiled coil motif of S2 found in 3JBH and 2FXO.

2.2 Myosin's Catalytic Cycle

A large body of literature has been devoted to understanding the nature of mechanochemical coupling between force generation and the catalytic hydrolysis of nucleotide in conventional myosins. In the absence of actin, the ATPase rate of all conventional myosins is very slow, but in the presence of increasing actin concentration, a classic cooperative activation of ATPase can be observed [23]. Thus myosin clearly requires coupled interactions with actin in order to work efficiently, and by measuring this actin-activated ATPase activity it is possible to calculate both a $V_{\max}$ for myosin and its apparent binding affinity to actin. The general mechanism of myosin's catalytic cycle has been well established [24], although many details regarding the structural dynamics of both proteins are still unknown (Figure 2.2). Broadly, the hydrolytic cycle begins when ATP binds in myosin's CD, reducing the affinity of myosin for actin and dissociating the complex. Hydrolysis of nucleotide is coupled to structural changes in the CD which move the lever arm into a cocked, "pre-powerstroke" position (this rearrangement is known as the "recovery stroke") [23, 25]. These changes alter actin-binding affinity slightly, allowing myosin to re-associate with actin. Once bound to actin again, the force-generating "powerstroke" occurs with a second large-scale movement of the lever arm, straightening the LCD while myosin undergoes a weak-to-strong binding transition with actin [23, 25]. Kinetic studies indicate that subsequent release of phosphate from the nucleotide binding pocket locks the post-powerstroke conformation in place [26, 27]. In several myosins, it has been shown that the full powerstroke actually occurs in two distinct steps with associated rate constants,

and numerous hypotheses have arisen to explain this phenomenon [28–30]. Most recently, single-molecule studies have observed a second transition that correlates well with the observed rate of ADP release from the complex, suggesting that the biochemical transitions of phosphate and nucleotide release may be coupled more strongly to mechanical transitions of the lever arm than was previously believed [31, 32]. Dissociation of ADP leaves the actomyosin complex in a strongly bound "rigor" state, and allows a new molecule of ATP to bind to begin the cycle anew. In the context of the muscle myofilament lattice, the ensemble motion of cycling myosin cross-bridges generates a rapid, coordinated contraction of sarcomeres as thick and thin filaments are drawn past each other by successive asynchronous binding, force generation and release.

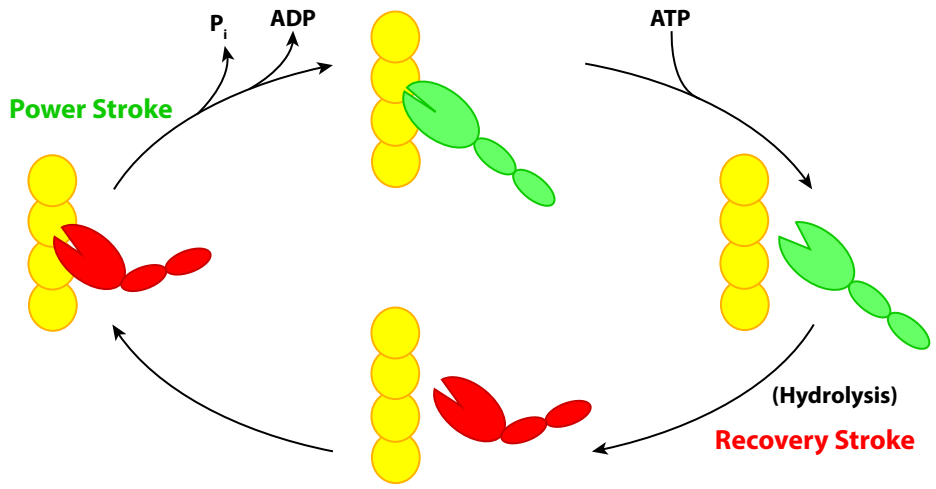

Figure 2.2. Overview of myosin's catalytic cycle. Clockwise from top: Myosin in rigor (top) binds ATP and dissociates from actin (right), before undergoing ATP hydrolysis and the recovery stroke (bottom). After hydrolysis and the recovery stroke, myosin may once again form a weak-binding complex with actin (left), before undergoing a powerstroke and releasing the hydrolysis products. Myosin is shown in red when assuming a weak actin-binding conformation with the lever arm bent ("pre-powerstroke"), and in green when assuming a strong actin-binding conformation with the lever arm straight ("post-powerstroke").

2.3 Roles of Conventional Myosins

In humans and other vertebrates, conventional myosins are found predominantly in the muscular tissue where they perform their previously described contractile function [14]. Numerous isoforms of the myosin II heavy chain occur with varying frequency across different muscle groups and types, however, and each exhibits distinct kinetic properties despite high sequence similarity ($> 80\%$ in humans) [33]. Expression of each isoform in skeletal muscle is carefully regulated to produce the appropriate ratio and slow and fast motors within each individual fiber (isoforms I, IIa, and IId/IIx in humans), and most bulk muscle contains a balanced mosaic of fast and slow fibers [34]. The composition of cardiac muscle is less diverse but contains its own unique distribution of isoforms, including a unique α isoform (expressed predominantly in the atria) and a β isoform (expressed in the ventricles, and analogous to skeletal isoform-I) [35].

While their role in muscle contraction is well-studied, Class II myosins perform many essential cellular functions outside of the context of the myofilament lattice [36]. The slime mold *Dictyostelium discoideum*, for instance, expresses a myosin II isoform highly similar to human muscle myosin, which has been observed to form bipolar filaments and is involved in many processes such as cell motility and contractile ring closing during cytokinesis [37]. In multicellular organisms, non-muscle myosin II often provides the driving force for cytoskeletal contraction during cellular development and differentiation [38]. High structural similarity to muscle isoforms, comparable ATPase activity, and relative ease of recombinant expression make these non-muscle isoforms attractive targets for structural

biology, and the *Dictyostelium* myosin in particular has been employed for many years as a standard model system for studying myosin II [39–41].

2.4 Structure and Function in the Myosin Catalytic Domain

Attempts to understand the intricate coupling of structural elements within the myosin CD are ongoing, with numerous structures from X-ray crystallography and cryo-electron microscopy having been published over the past 20 years. In order to support its multi-functional role, the structure of the myosin CD is necessarily complex, and virtually every subdomain has been identified as a potentially important contributor to effective catalytic coupling. In all myosins, the actin-binding interface is composed of a series of flexible loops spread across two large domains distal to the lever arm, known as the Upper and Lower 50kDa domains, respectively [42–44]. These two large domains are separated by a solvent-filled cavity known as the actin-binding cleft, which has been proposed to close when forming a high-affinity actomyosin complex [45]. The nucleotide-binding pocket is nestled just above the cleft in the Upper 50kDa domain, and occupies a central location within the CD. The opposite side of the Upper 50kDa domain is a flat and relatively well-structured region sometimes called the "mesa", which has been implicated in binding interactions with myosin binding protein C (another sarcomeric regulatory protein) as well as with myosin's own subfragment-2 region in the super-relaxed state [46–48]. A large 7-stranded β-sheet sits distal to the actin-binding loops, and an apparent twisting and straightening of the sheet during force generation has led to the proposal of its role as a

spring-like force transducer [49]. Furthest from the actin-binding cleft and adjacent to the LCD are the N-terminal and C-terminal domains, the latter of which often referred to as the converter domain for its proposed role in directly influencing lever arm position [50, 51]. Two notable α-helices extend into this force-generating region of the CD. The SH1 helix contains two highly conserved, reactive Cys residues (SH1 and SH2), which are essential for maintaining ATPase rates on the order of wild-type activity [52–54]. The relay helix, sitting adjacent to the SH1 helix, has a flexible C-terminus which appears in crystal structures to bend significantly when myosin occupies a nucleotide-bound state that would correlate with a cocked lever arm. Thus, a prevailing hypothesis is that the position of the relay helix C-terminus serves as a reporter for the position of the LCD [55, 56]. Finally, several classes of myosin (including the conventional myosins) contain an SH3-like domain between their N-terminus and the rest of their homologous N-terminal domain. While the function of this domain is unknown, its insertion radically alters the position of the N-terminus with respect to the rest of the CD. Isoforms which lack this SH3-like domain exhibit putative electrostatic interactions between the N-terminus and bound light chains on the LCD; such interactions are hypothesized to play an important role in tuning the load-dependent release of nucleotide, and subsequently conferring tension-sensing functionality to the motor [57, 58].

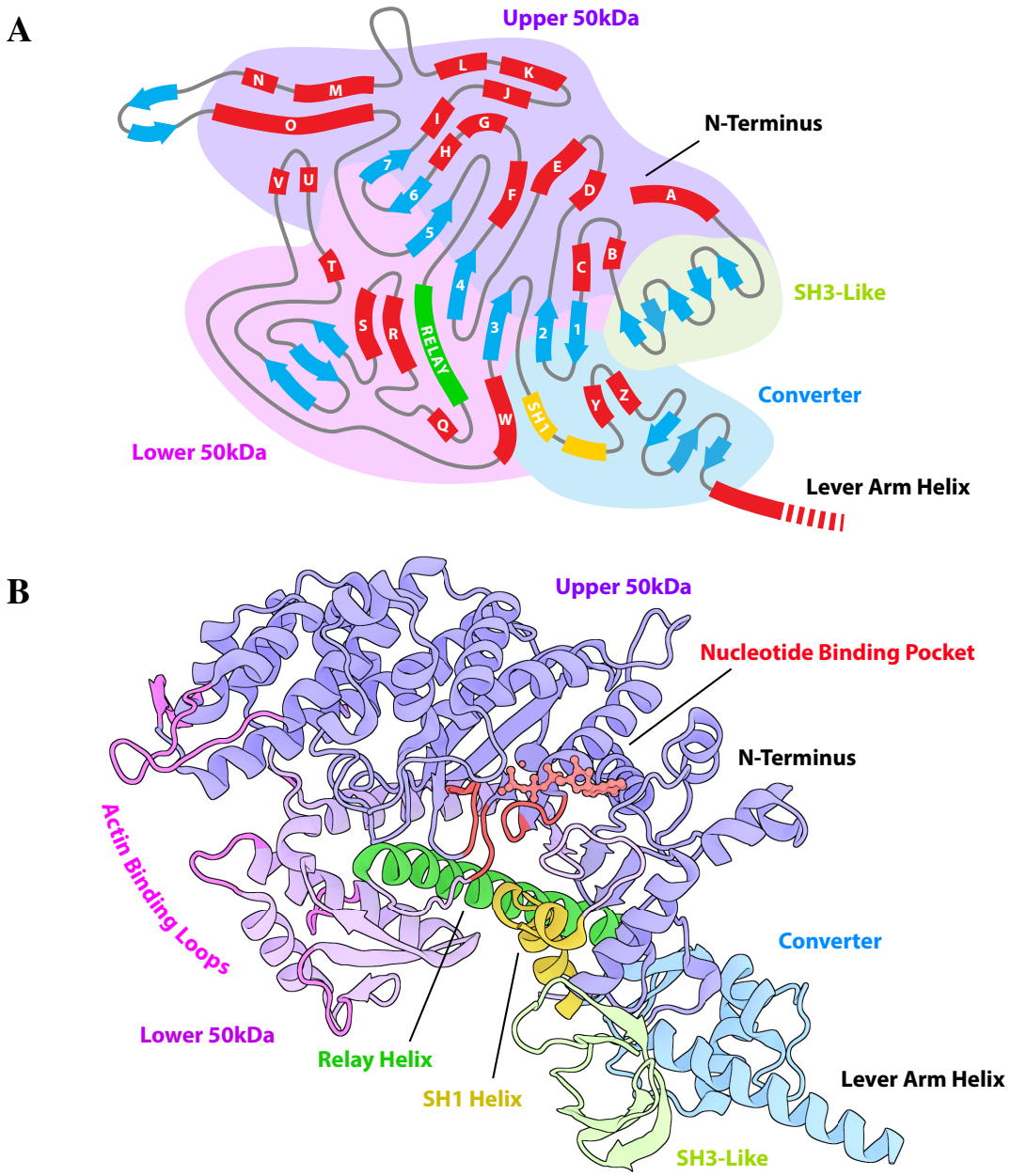

Figure 2.3. Structure of the myosin II catalytic domain. A: Topological view of the myosin CD, showing α-helices (red) and β-strands (blue). Color underlays designate subdomains: the Upper 50kDa domain (violet), Lower 50kDa domain (magenta), SH3-like domain (lime green) and Converter domain (cyan). The relay helix (green) and SH1 helix (yellow) are designated by name; all other helices are labeled according sequence position, by literature convention [59]. The 7 strands of the central β-sheet are also numbered [60]. B: Tertiary structure view of the myosin CD, with the same subdomain color codes as in A. Relay and SH1 helices are highlighted as in A; loops of the nucleotide binding pocket (red) and actin binding interface (pink) are also highlighted. ATP (red) is shown occupying the nucleotide binding pocket. Structure is a *Dictyostelium* myosin homology model similar to [61].

2.5 Motivation for Research (Part I)

The integrated mechanics [61] of the myosin CD are thus believed to be very elaborate, and elucidating the roles of the various subdomains has been the target of aggressive investigation. Numerous truncations, point mutations, and mixed-isoform chimeras have been meticulously studied in vitro by many approaches: motor function has been assessed by actin filament sliding assays and single-molecule force measurements [32, 62, 63]; ATPase rates have been measured using stopped-flow transient kinetics and photolysis of caged ATP [26, 64, 65]; and lever arm rotation has been quantified by fluorescence anisotropy and super-resolution microscopy [66–68]. Several of these techniques overlap and complement one another, collectively aiding in the assembly of a coherent portrait for myosin's mechanochemistry.

Ultimately, however, detailed interpretation of these functional assays typically depends on extensive references to data from crystallography or cryo-electron microscopy, because these techniques possess the requisite resolution to consider interplay between individual protein residues and secondary structural elements. Unfortunately, no crystal structures of myosin in the presence of actin have yet been reported, and thus no models of the entire actomyosin complex with true atomic resolution currently exist. Significant advances in cryo-EM methods have led to improved models for actomyosin at resolutions as low as ~ 3 angstroms, but sample heterogeneity in the presence of additional ligands poses problems for characterizing structural states other than rigor [49, 69]. As myosin radically

alters its enzymatic activity in the presence of actin, the difficulty in studying the structure of both proteins in complex constitutes a significant hurdle for understanding muscle mechanics at the molecular level. While both techniques will undoubtedly improve in the coming years, a greater intrinsic limitation remains: conventionally, both crystallography and cryo-EM produce static snapshots of proteins in frozen and/or crystalline environments. These conditions impose constraints that may cause the resulting structure to deviate significantly from its physiological form; moreover, neither technique can accurately render transitions between structural states, or quantify the amount of local disorder present in protein subdomains.

Determining the nature of such behaviors is essential for understanding structure-function relationships within myosin. No large-scale structural rearrangement of the CD is observed during the catalytic cycle, and thus the coupling of actin binding, nucleotide hydrolysis, and force generation is expected to occur via small internal transitions that affect the orientation and dynamics of individual structural elements. Likewise, many disease-causing mutations and deleterious post-translational modifications appear to render their effects via subtle re-tuning of myosin's mechanochemistry, rather than promotion of large-scale misfolding and aggregation [70]. With the usual methods for atomistic structure determination largely unsuitable or unavailable, site-directed spectroscopy represents an essential alternative for determining structural information at high resolution. Spectroscopic methods are not hampered by the presence of polymers like F-actin, and judicious experimental design enables precise characterization of multiple states within an ensemble. Thus,

site-directed fluorescence and electron paramagnetic resonance (EPR) have been employed as methods of choice in the detailed study of myosin's catalytic cycle. EPR in particular possesses exceptionally high spectral sensitivity to probe orientation, rotational dynamics, and inter-probe distances, making it ideally suited for multifaceted investigations at the molecular level.

CHAPTER 3: ELECTRON PARAMAGNETIC RESONANCE

3.1 Principles of EPR Spectral Acquisition

All forms of spectroscopy fundamentally rely on the absorption (and/or subsequent emission) of energy by a species of interest. Infrared spectroscopy activates vibrational modes between bonded atoms, UV/Vis spectroscopy excites electronic transitions, and electron paramagnetic resonance (EPR) uses microwave frequencies to flip the quantum spin states of unpaired electrons. Electronic spin is a binary quantum mechanical property of electrons, represented in classical mechanics as the precession of a magnetic moment about its axis in either the "spin up" or "spin down" configuration. In quantum mechanics, these two orientations correspond to spin projection quantum numbers $m_s = +½$ and $-½$, respectively. Two electrons sharing an orbital must occupy opposite spin states, but since the states are (normally) degenerate, simultaneous exchange occurs freely and the two electrons are thus practically indistinguishable. Free exchange is normally possible for an unpaired electron as well, as again the two states are degenerate. In the presence of a strong magnetic field ($\vec{B}$), however, this degeneracy is broken in a phenomenon known as the Zeeman Effect. As magnetic field strength (B_0) increases, one spin state "aligns with" the external field and thus lowers its interaction energy (assuming the so-called α state), while the other spin state "aligns against" the field and raises its interaction energy (assuming the so-called β state) (Figure 3.1A). A sufficient energy gap established in this way may be excited by absorption of microwaves, producing a spectrum which reflects the physical

and chemical properties of the sample.

In order to be EPR-active, an atom or molecule must contain an unpaired electron, and initial biophysical applications of EPR thus centered largely on proteins with metal-containing prosthetic groups. For proteins which do not contain native metal centers, the most common approach is to introduce stable nitroxide "spin labels" at locations of interest; this process is called site-directed spin labeling (SDSL), and is accomplished either via covalent reaction with side chains or by direct incorporation via solid-phase peptide synthesis. In the present work, all paramagnetic species employed are nitroxides introduced by the former mechanism, and thus the discussion of spectral properties that follows will often refer specifically to nitroxide radicals.

Conventional continuous-wave EPR (CW-EPR) is typically acquired by holding the microwave excitation frequency fixed while progressively increasing the strength of the external magnetic field, producing a classic field-swept spectrum (Figure 3.1B). Absorption peaks are observed wherever the energy gap between spin states matches the energy delivered by the microwave source. EPR spectrometers detect these absorption events by a method known as phase-sensitive detection (PSD), which dramatically increases instrument sensitivity to the relatively weak signal. Modulation coils surrounding the sample cavity confer a rapid, regular modulation on the magnetic field $\vec{B}$ as it is swept during acquisition, resulting in reflected microwaves which are amplitude-modulated at the same frequency. These reflected microwaves are received by a lock-in amplifier, which compares them to a

reference signal of matching modulation frequency. The amplifier is only sensitive to signals which match the reference frequency, and thus the true EPR signal is amplified, while other contributions such as noise and electrical interference are suppressed. A by-product of this comparative filtering approach is that the output of the lock-in amplifier, and thus the recorded EPR signal, is proportional to the *first derivative* of the absorption spectrum (often denoted V_1), rather than the absorption spectrum itself (V_0). A given position of maximum resonance is thus marked by a zero-crossing point in the field-swept EPR spectrum (Figure 3.1C).

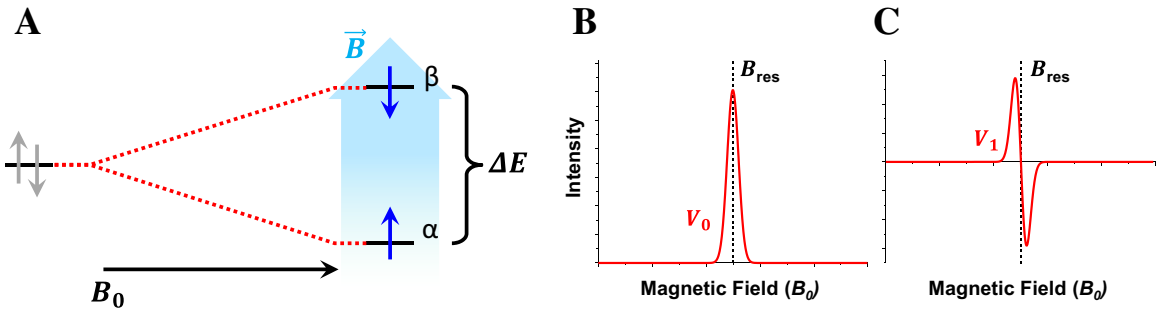

Figure 3.1. Overview of the EPR absorption phenomenon. A: Application of an external magnetic field ($\vec{B}$, blue) breaks the degeneracy of $+½$ and $-½$ electron spin states (gray), imposing a tendency for spins to align with the field (α state on right) or against the field (β state on right). The magnitude of the resultant energy gap (ΔE) is proportional to the strength of the applied field (B_0). B: Representative V_0 field-swept EPR spectrum, corresponding to the absorption of energy by an unpaired electron when the energy delivered by the microwave source matches the energy gap ΔE in A (i.e. when the magnetic field strength is at B_{res}, the resonance position). C: V_1 EPR spectrum, which is the first derivative of B, and represents the standard spectrum actually acquired by an EPR spectrometer thanks to the effects of the lock-in amplifier.

3.2 Orientation Dependence of EPR

Regardless of the specific application, the great power of conventional EPR as a biophysical tool ultimately stems from its high intrinsic sensitivity to the orientation of paramagnetic species within a sample. In order to understand how this orientational sensitivity arises, it is necessary to examine the physical nature of the spectrum in detail. Recall from the preceding section that the energy gap required for excitation is produced in EPR via application of an external magnetic field $\vec{B}$, which forces the degenerate $+½$ and $-½$ spin states of an unpaired electron apart (the Zeeman Effect). In order to determine the position of EPR absorption resonances, it is necessary to quantify that energy gap.

In the presence of an external magnetic field $\vec{B}$, the energy imparted to an electron's spin state by the Zeeman interaction is a function of the electron's magnetic moment (μ_s) and the external field vector $\vec{B}$ [71]. Specifically, the Hamiltonian for the Zeeman interaction is

$$\mathcal{H}_{\mathrm{EZ}} = -\vec{B} \cdot \vec{\mu}_s \tag{3.1}$$

As expected, Equation 3.1 shows that the energy of the Zeeman interaction is minimal when the magnetic moment is parallel to the external field, and maximal when the magnetic moment is aligned against the external field. The direction of $\vec{B}$ is arbitrary, but by convention it is typically defined along the positive z-axis of the reference frame, so that $\vec{B} \equiv [\,0\ 0\ B_0\,]$.

From quantum mechanics, the magnetic moment of an electron is equal to

$$\vec{\mu}_s = \gamma \cdot \hat{\vec{S}} \tag{3.2}$$

where γ is the gyromagnetic ratio and $\hat{\vec{S}}$ is the electron spin operator [72]. For the purposes of further derivation, it is useful to rewrite the gyromagnetic ratio in terms of an intrinsic magnetic property called the electron g-factor (g), with $\gamma = -\mu_B g/\hbar$. The g-factor will be treated as a scalar for now, but further discussion will reveal why this is not the case for unpaired electrons associated with molecules. The electron spin operator $\hat{\vec{S}}$ can be written as $\hat{\vec{S}} = [\hat{S}_x \ \hat{S}_y \ \hat{S}_z]$ where each $\hat{S}_i$ corresponds to the expectation value of the spin component along that axis. When the external magnetic field is strong enough (as is the case in EPR), spin z-axes achieve near-complete alignment with $\vec{B}$, and thus the transverse components of $\hat{\vec{S}}$ may be assumed to be negligible [73]. In an EPR experiment, therefore, $\hat{\vec{S}} \equiv [0 \ 0 \ \hat{S}_z]$. The possible values of $\hat{S}_z$ are directly related to the spin projection quantum number m_s, such that $\hat{S}_z = m_s\hbar$.

When all substitutions are applied, Equation 3.1 is simplified:

$$\mathcal{H}_{\mathrm{EZ}} = -\vec{B} \cdot \left(\gamma \cdot \hat{\vec{S}}\right) = -\begin{bmatrix} 0 & 0 & B_0 \end{bmatrix} \cdot \left((-\mu_B g/\hbar) \cdot \begin{bmatrix} 0 \\ 0 \\ m_s\hbar \end{bmatrix} \right) = m_s g \mu_B B_0 \tag{3.3}$$

Finally, the energy gap created by B_0 is the difference between the energies of the $+½$ and

$-½$ electron spin states:

$$\Delta E = \left|E_{\text{up}} - E_{\text{down}}\right| = \left|(+½)\, g\mu_B B_0 - (-½)\, g\mu_B B_0\right| = g\mu_B B_0 \tag{3.4}$$

In EPR spectroscopy, absorption occurs when the energy delivered by the microwave source matches the value of ΔE as B_0 is swept (Figure 3.1) [71]. Representing the microwave energy as $h\nu$, where h is the Planck constant and ν is the fixed frequency used during spectral acquisition, the resonance position B_{res} on a field-swept spectrum is determined by the following substitution:

$$\Delta E = h\nu = g\mu_B B_0 \implies B_{\text{res}} = \frac{h\nu}{g\mu_B} \tag{3.5}$$

The Zeeman Effect is thus responsible for producing a single absorption resonance for a given spin system at a well-defined field strength. If the paramagnetic species were a free electron, one would therefore expect to observe a single resonance peak for a completely homogeneous system.

However, an unpaired electron associated with a molecule incurs additional effects from its surroundings. The greatest influence on a radical's resonance condition comes from its associated nucleus, which possesses its own magnetic moment and can therefore modulate the effective field experienced by the electron. Strictly speaking, there are two effects rendered by the nucleus on the electron spin state energy: Zeeman splitting of the nuclear spin states due to the external field ($\mathcal{H}_{\text{NZ}}$), and the so-called *nuclear hyperfine*

interaction which involves coupling of the electron and nuclear magnetic moments ($\mathcal{H}_{\mathrm{HF}}$) [71]. In the context of an EPR experiment, the relative magnitude of $\mathcal{H}_{\mathrm{NZ}}$ is so small as to be negligible, and it is not generally considered. The magnitude of $\mathcal{H}_{\mathrm{HF}}$, on the other hand, depends on the quantum state of the nuclear spin, and ultimately results in an offset in the resonance position. This offset can be written as $m_I A$, where m_I is the nuclear magnetic moment quantum number, and A is the hyperfine coupling constant with units of magnetic field strength (Appendix A contains a derivation of this contribution). Adding this term to the above equation, we obtain a more complete expression for the resonance position:

$$B_{\mathrm{res}} = \frac{h\nu}{g\mu_B} - m_I A \tag{3.6}$$

Additional effects from other nearby nuclei (termed "superhyperfine" interactions) can also contribute, but their effect on nitroxide EPR spectra at conventional X-band microwave frequencies is typically unresolved, and thus will be discussed later only in the context of their contribution to linewidth. Two features of Equation 3.6 are immediately noteworthy. First, the effect of A on the spectrum is degenerate, being dependent on value of m_I; as a result, resonance from a single spin population will split into multiple primary absorption peaks, one for each m_I state available to the atomic nucleus associated with the unpaired electron. Second, only two terms in Equation 3.6 are dependent on the properties of the sample: the electron g-factor (g), and the nuclear hyperfine coupling (A). The value of g will influence the center of the peak distribution, while the value of A will determine the splitting between peaks.

For the purposes of further discussion, consider all this in the context of a nitroxide spin label. The unpaired electron density in a nitroxide is predominantly centered on the nitroxide nitrogen when immersed in polar aqueous environments, so a nitrogen atom will typically be the source of the nuclear hyperfine interaction. A ^{14}N atom has nuclear spin quantum number $I = 1$, and corresponding magnetic moment quantum numbers $m_I = (-1, 0, 1)$. Thus, a typical nitroxide EPR spectrum for a completely homogeneous, crystalline sample will contain 3 well-resolved, distinct absorption lines centered according to the value of g and with a peak-to-peak distance dictated by the value of A (Figure 3.2).

Having established the factors that give rise to resonance, the source of EPR's orientation sensitivity can now be revealed: both the g-factor g and the nuclear hyperfine coupling A are, in fact, highly anisotropic properties. The magnetic moment of an unpaired electron acquires anisotropic characteristics due to the shape of its associated molecular orbital system, conferring anisotropy on the g-factor; likewise, orbital shape also affects the interactions between the nuclear and electron magnetic moments, conferring anisotropy on the nuclear hyperfine interaction.

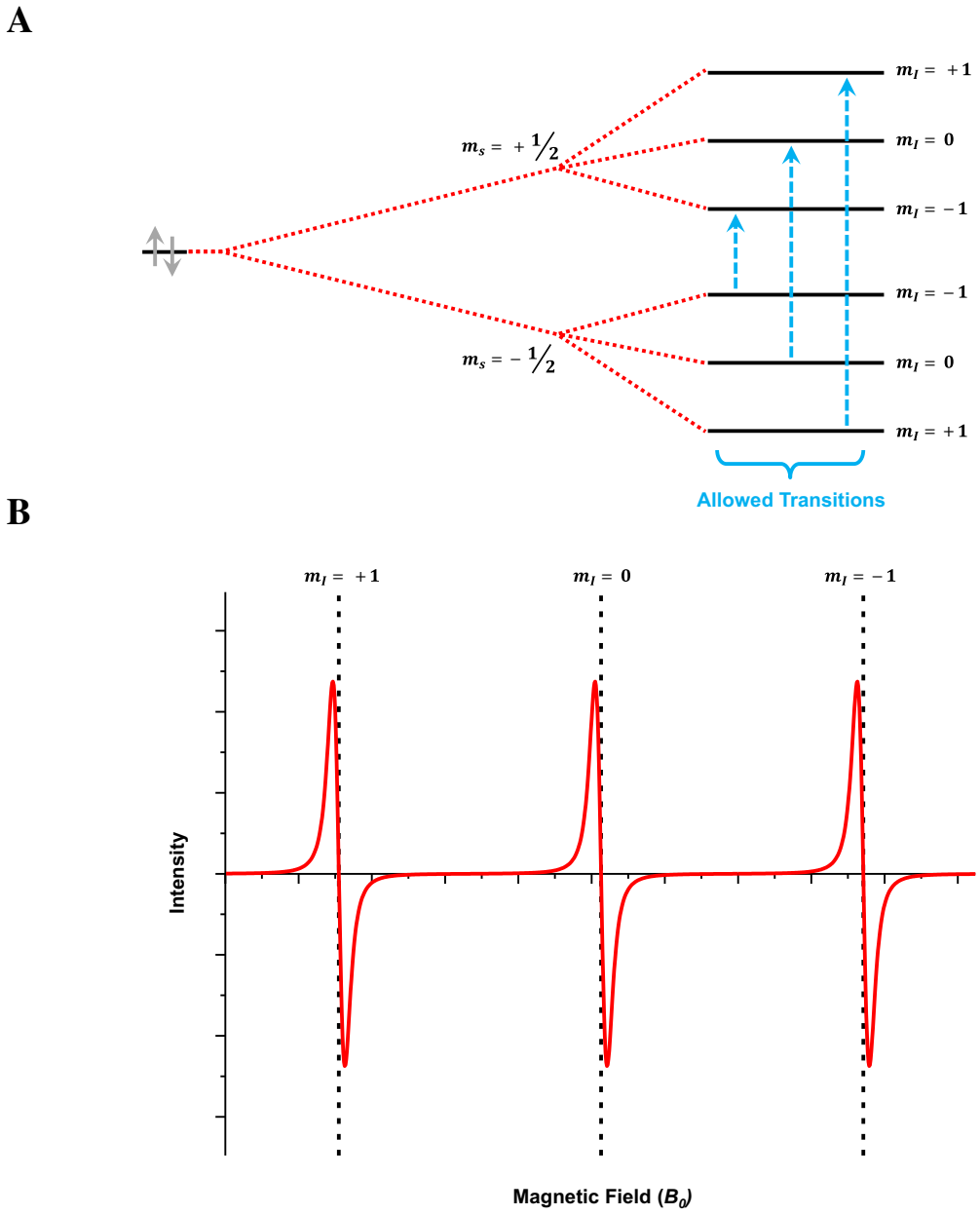

Figure 3.2. The effects of hyperfine splitting on a nitroxide EPR spectrum. A: Hyperfine splitting from a nearby ^{14}N nucleus further subdivides the energy levels separated by the Zeeman effect into three sublevels each, corresponding to the nuclear spin quantum state (described by m_I). Selection rules mandate that $\Delta m_I = 0$ and $\Delta m_s = 1$, so three distinct excitation events are allowed. B: Typical nitroxide EPR spectrum, highlighting the three absorption lines resulting from the nuclear hyperfine interaction. The low-field line, for instance, corresponds to a transition between $m_I = +1$ states, because the energy gap between those states is the largest of the three, and thus requires the lowest magnetic field strength for excitation with microwaves of fixed frequency.

To describe this anisotropy, both g and A are fully represented as second-rank tensors, each consisting of 9 values arranged in a 3x3 matrix. Theoretical and empirical studies on crystalline samples of nitroxide spin labels have determined that the principle axes of both the g and A tensors are coincident with the molecular geometry of the nitroxide group [74, 75]. By convention, the axes are designated such that $g'_{xx} > g'_{yy} > g'_{zz}$. As a result, the x-axis of this coordinate frame (x_N) is defined along the N-O bond, the z-axis (z_N) is defined by the p_z-orbital of the nitrogen, and the y-axis (y_N) lies in a direction orthogonal to both x_N and z_N (Figure 3.3) [74, 76]. This reference coordinate frame, defined by the nitroxide molecule and directly tied to the magnetic properties of the free radical, is referred to hereafter as the "nitroxide frame".

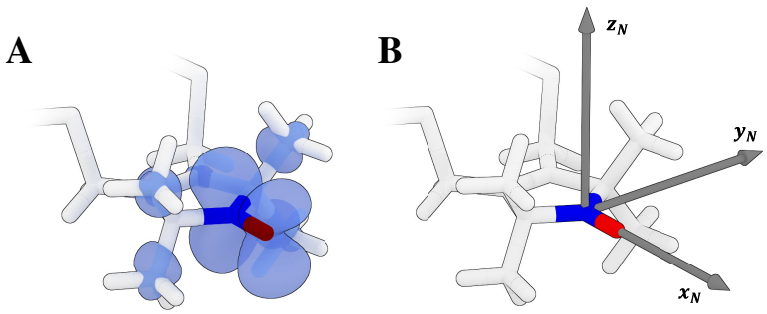

Figure 3.3. Spin anisotropy and the nitroxide coordinate frame. A: Positive electron spin density visualized on a nitroxide spin label, with the nitroxide bond highlighted in red and blue. The density shown was calculated in the presence of a dielectric continuum, approximating an aqueous solvent environment. Spin density is distributed mainly between ^{16}O ($I = 0$) and ^{14}N ($I = 1$), but the polar environment increases the fraction of density associated with ^{14}N via partial charge stabilization. B: The nitroxide coordinate frame, with principle axes x_N, y_N and z_N defined by the molecular geometry.

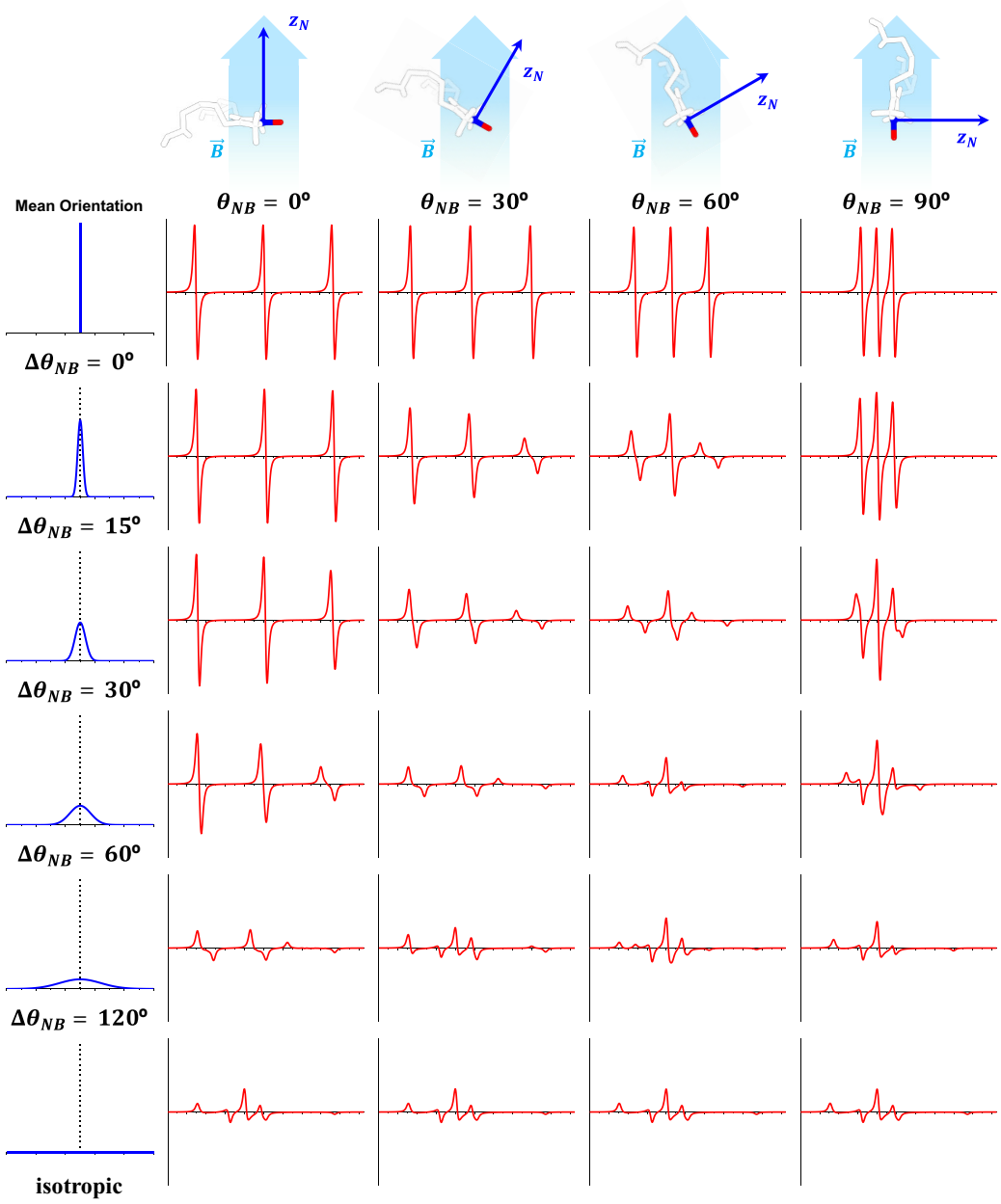

Figure 3.4. Orientation dependence of the nitroxide EPR spectrum. Columns illustrate how the lineshape of the acquired V_1 spectrum is highly sensitive to the axial polar angle θ_{NB}, which describes the orientation of the nitroxide frame z-axis (z_N, top, blue) relative to the external magnetic field ($\vec{B}$, top, cyan). Rows illustrate how static disorder also affects the ensemble lineshape. Disorder is quantified here by $\Delta\theta_{NB}$, which describes the full width at half maximum for a Gaussian distribution of angles centered at a given θ_{NB}. EPR spectra are also sensitive to the azimuthal angle ϕ_{NB}, but the effect on spectral lineshape is more subtle (effects not shown).

The anisotropy of the g and A tensors means that their effective values in Equation 3.6 depend on the orientation of the paramagnetic species in the external magnetic field: the presence of $\vec{B}$ imposes different effects on both the electron and nuclear magnetic moments depending on how the molecule is oriented relative to $\vec{B}$. It turns out that both g and A may in fact be written purely as the functions $g(\theta_{NB}, \phi_{NB})$ and $A(\theta_{NB}, \phi_{NB})$, where θ_{NB} and ϕ_{NB} are polar angles which describe the orientation of $\vec{B}$ in the nitroxide frame (see Appendix A for a full derivation of these functions):

$$g(\theta_{NB}, \phi_{NB}) = g'_{xx} \sin^2 \theta_{NB} \cos^2 \phi_{NB} + g'_{yy} \sin^2 \theta_{NB} \sin^2 \phi_{NB} + g'_{zz} \cos^2 \theta_{NB} \tag{3.7a}$$

$$A(\theta_{NB}, \phi_{NB}) = \sqrt{{A'_{xx}}^2 \sin^2 \theta_{NB} \cos^2 \phi_{NB} + {A'_{yy}}^2 \sin^2 \theta_{NB} \sin^2 \phi_{NB} + {A'_{zz}}^2 \cos^2 \theta_{NB}} \tag{3.7b}$$

Adjustment of θ_{NB} and/or ϕ_{NB} thus renders significant effects on the values of B_{res}, and subsequently on the lineshape of the resulting EPR spectrum (Figure 3.4, columns). This is the source of EPR's exceptional sensitivity to probe orientation: the relative positions of absorption lines are directly dependent on the spatial orientation of the absorbing paramagnetic species relative to the laboratory reference frame. Spectral lineshape is also highly sensitive to the amount of static disorder present in a system, as all spectra are linear combinations of their components, and therefore a given distribution of angles will give rise to a unique sum of resonances (Figure 3.4, rows).

With the orientation dependence of the resonance positions defined, few additional parameters are required to fully characterize the spectrum (these include parameters for homogeneous and inhomogeneous line broadening, typically simulated via Gaussian and

Lorentzian convolutions, respectively). Provided that the sample in question is devoid of confounding effects (such as nanosecond motion, discussed in the next section), it is therefore possible to determine θ_{NB} and ϕ_{NB} directly from least-squares fitting of a simulated spectrum to the data using very few parameters.

Tight dependence on orientation and ease of simulated fitting means that in systems where the paramagnetic ensemble can be oriented around $\vec{B}$, the potential for measuring precise structural constraints by EPR is theoretically vast. In addition to the obvious application in crystals, EPR could also reveal the alignment of paramagnetic species incorporated into oriented biological assemblies such as muscle fibers or membrane bilayers. With specific regard to SDSL methods, the high sensitivity of EPR to both mean orientation and static disorder means that a single spin-labeled location within an oriented ensemble of proteins can reveal much about the structure of that protein.

Finally, cases where orientational order is absent are also informative for the purposes of simulated fitting. An isotropic distribution of static spins produces a characteristic lineshape often observed in dry powders, and is known as a powder spectrum. Powder spectra are helpful for empirically deriving the principle values of g and A in an unknown system, as the distribution of θ_{NB} and ϕ_{NB} can be fixed at the isotropic limit and therefore the intrinsic tensor values alone dictate the shape of the spectrum.

3.3 Motional Dependence of EPR

In principle, the orientation dependence of EPR affords extremely high resolution to θ_{NB} and ϕ_{NB} in the spectrum, but there are other properties of a spin system that can influence the spectral lineshape. Chief among these is the contribution from motion of the paramagnetic center relative to the applied magnetic field. Motion essentially introduces a modulation of the anisotropy discussed in the previous section, with spin orientation changing in three dimensions at a given rate as the molecule tumbles in solution. The simplest cases to consider involve isotropic rotational tumbling, and can be grouped into 3 motional regimes according to their associated rotational correlation time (τ_R). When the rate of motion is sufficiently slow ($\tau_R \geq 10^{-6}$ s; the so-called "rigid limit" of CW-EPR), spins absorb energy and relax before significant changes in their spatial orientation can occur, and their apparent resonances are thus unaffected. Such a spectrum may be simulated using the same methods described in the previous section (resulting in a powder spectrum for a randomly oriented ensemble). Conversely, when the rate of isotropic motion becomes sufficiently rapid ($\tau_R \geq 10^{-12}$ s; the so-called "fast limit" of CW-EPR), all contributions from the intrinsic tensor anisotropies are averaged out, such that the spectrum shows no orientation dependence whatsoever:

$$g_{\text{eff}} = \frac{1}{3}\left(g'_{xx} + g'_{yy} + g'_{zz}\right) \tag{3.8a}$$

$$A_{\text{eff}} = \frac{1}{3}\left(A'_{xx} + A'_{yy} + A'_{zz}\right) \tag{3.8b}$$

The intermediate regime lying between the fast and rigid limits (10^{-7} s $\leq \tau_R \leq 10^{-12}$ s) constitutes the domain where spectra from spin-labeled proteins typically reside. The covalent attachment of a spin label to the protein backbone necessarily introduces a flexible linker, which tethers the paramagnetic center to the site of interest; for conventional nitroxide spin labels, this includes 4-5 saturated bonds, allowing the nitroxide to undergo a wide range of motion relative to the labeled site. Such motion typically falls on the nanosecond timescale.

Effects of motion in this intermediate regime on the EPR spectrum are more complex than the extreme fast and slow cases described above. Spins transfer on and off-resonance as they tumble, resulting in broadening of the absorption lines. Anisotropies in the tensors also become partially averaged by rapid interconversion between orientations; crucially, this partial averaging greatly obscures the intrinsic orientation dependence of the EPR spectrum, so that even spectra from samples with significant orientational order are heavily dominated by motional effects.

Overall, the transfer of resonance and partial averaging of tensors produces a general trend where line splitting and apparent linewidth both decrease as τ_R shortens from the rigid limit. Simulation of such spectra is typically accomplished via the stochastic Liouville equation (SLE), a semi-classical diffusion model which accounts for the effects of motion on spin relaxation. The SLE introduces several new parameters, including a rotational diffusion tensor (R) with its associated diffusion coordinate frame, and orienting potentials in the diffusion frame built up from spherical harmonics. In theory, these parameters allow

SLE-based simulations to represent the effects of many different types of motion on the EPR spectrum with a high level of precision.

When considering these motionally-influenced spectra in practice, however, derivation of meaningful constraints proves challenging beyond the most rudimentary applications. Any simulation involving nanosecond motion will always be subject to increased ambiguity over the static simulations described in the previous section, given that a greater number of parameters can have degenerate effects on the spectrum (apparent linewidth, for instance, is affected both by homogeneous and inhomogeneous broadening, as well as rotational diffusion). Furthermore, SDSL methods suffer additional ambiguity because it is not possible to know for certain what portion of the reported diffusion arises from motion of the protein backbone, and what portion arises from motion of the spin label relative to the protein (the latter contribution typically dominates for conventional labels). Finally, as stated above, orientation dependence in the spectrum is also largely ablated by nanosecond motion, drastically reducing the resolution of θ_{NB} and ϕ_{NB} in oriented systems.

Thus, SDSL methods for CW-EPR in large proteins have been limited by dependence on spin labels that exhibit nanosecond motion. Except in rare circumstances where a label becomes immobilized by side chain interactions, applications generally fall either to basic characterization of the local environment, or to the detection of significant changes in spin label mobility that may result from binding interactions or conformational change. To investigate the structure and dynamics of the protein backbone itself, alternative techniques are typically required.

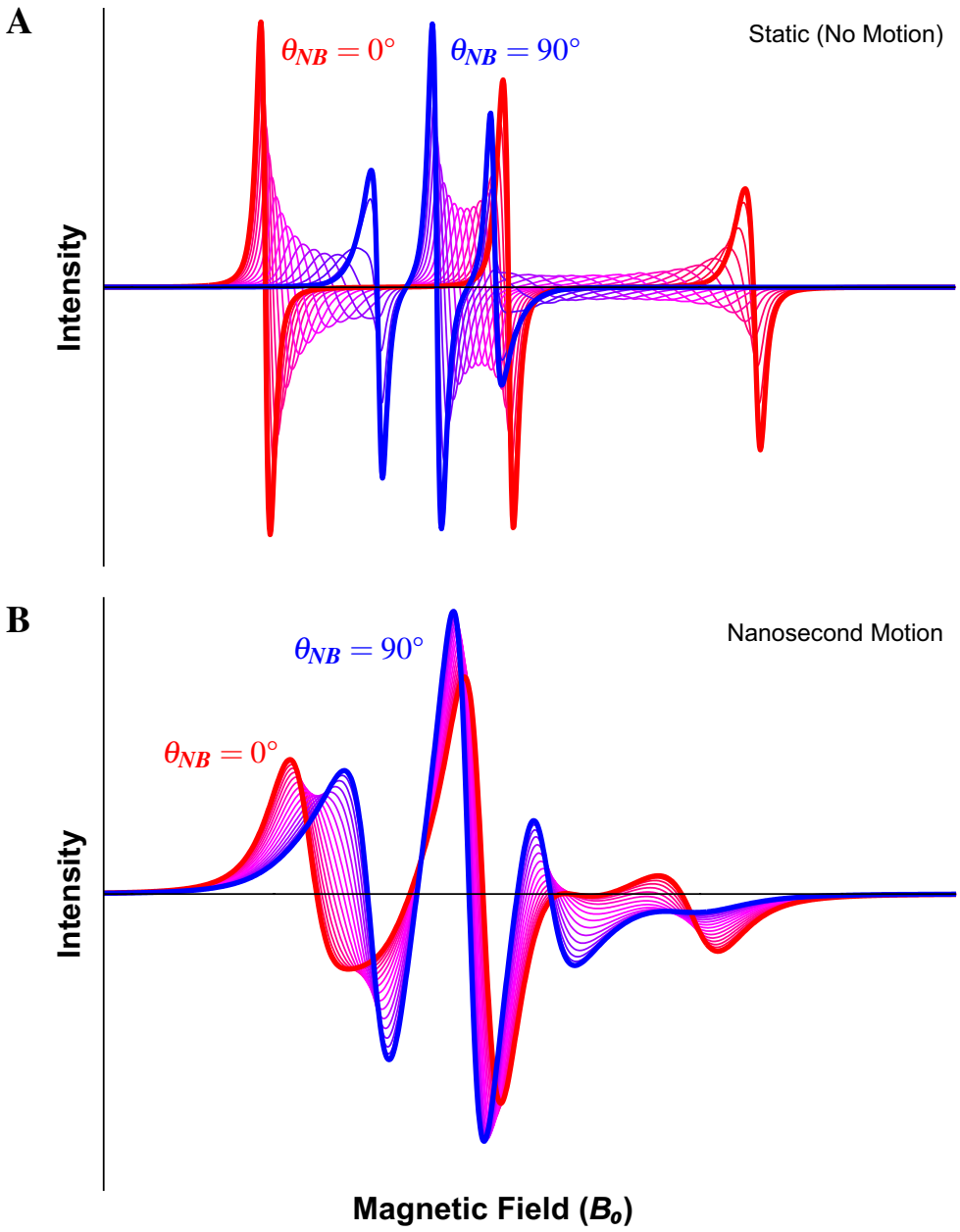

Figure 3.5. The effect of nanosecond motion on the EPR spectrum of oriented nitroxides. A-B: Simulated EPR spectra of nitroxides oriented with $\theta_{NB} \in [0°, 90°]$ and $\phi_{NB} = 0°$. Static disorder in θ_{NB}, modeled as a Gaussian orientational distribution with FWHM= 15°, has been added to each simulation to represent the macroscopic disorder common in spin-labeled protein samples. Bold traces represent distributions centered at $\theta_{NB} = 0°$ (red) and $\theta_{NB} = 90°$ (blue), with intermediate traces drawn in increments of 5°. A: Nitroxide EPR spectra simulated without nanosecond motion, as discussed in Section 3.2. B: Same system as A, with the addition of nanosecond motion characterized by restricted motion in a cone with angle 70° and rotational correlation time $\tau = 32$ns. Motional narrowing drastically reduces the spectrum's sensitivity to θ_{NB}, compared with the immobilized system in A.

3.4 Distance Measurements by Pulsed EPR

The EPR phenomenon can also be exploited in more complex experiments to yield different information about a spin system. Dipolar electron-electron resonance (DEER) is a pulsed EPR technique of particular relevance to structural biology, as it enables the derivation of distances between two or more nearby spins [77]. By employing two spin labels by SDSL on a protein or protein complex of interest, DEER can be used to measure the distance between the two sites. DEER has become a standard tool in biophysical EPR alongside CW-EPR experiments, and has found many applications from the detection of structural changes in enzymes to the *de novo* determination of complex structural models [45, 56, 78, 79]. The technique is analogous to Förster resonance energy transfer (FRET) in fluorescence spectroscopy, and has occasionally been employed in complement with FRET to study the same system [56, 80]. Nitroxide DEER has a narrower range of sensitivity to distance than FRET (on the order of 1.5-5nm for samples with non-negligible disorder) and must be performed at cryogenic temperatures, but possesses markedly superior resolution due to its feature-rich waveform, and enjoys the practical advantages of smaller labels and the ability to employ the same label at both sites of interest.

The basis of a DEER experiment is the classic spin echo pulse sequence common in NMR spectroscopy [81]. Just as in the standard CW setup, the paramagnetically-labeled sample must be placed in a magnetic field to establish Zeeman splitting and create the requisite energy gap. The difference is that the microwave radiation used for excitation is delivered as discrete pulses, rather than by continuous exposure. At the beginning of

the experiment, a $\pi/2$ pulse delivered orthogonal to the static magnetic field saturates the spin system, and generates coherence in the lab frame's transverse plane. This orients the bulk magnetization vector in the transverse plane, orthogonal to both the external field and the microwave source. As time advances following the initial pulse, transverse coherence is lost as chemically unique spins begin to precess at slightly different frequencies (i.e., T_2 relaxation occurs). After a specified time τ, a π refocusing pulse inverts the system, reflecting all magnetic moments across the source axis and allowing them to momentarily reestablish coherence on the other side as they continue precessing (this occurs at time 2τ). The resulting buildup and subsequent decay of transverse magnetization is known as a "spin echo", and ultimately serves as the source of the signal in DEER (Figure 3.6A, blue).

When performed alone, the spin echo experiment is not sensitive to the distance between spins; while each spin affects the local magnetic field experienced by its neighbors, the amplitude of the refocused echo will not depend on individual precession frequencies. In DEER, however, the spin echo is only half the experiment: the $\pi/2$ and π pulses are delivered with narrow bandwidth at a fixed frequency (the "observe" frequency, ν_{obs}), exciting only a small subset of the total spin population (the "A-spins"). Between the $\pi/2$ and π pulses at ν_{obs}, an additional π pulse at a different microwave frequency (the "pump" frequency, ν_{pump}) excites a second population of spins (the "B-spins") (Figure 3.6A, orange). The Boltzmann distribution of the B-spins is inverted by the pump pulse, causing the sign of their bulk magnetization to flip. Assuming that ν_{obs} and ν_{pump} both excited an appreciable number of spins, there will be many cases in which one A-spin and one B-spin exist

in close proximity, ideally paired up within the construct of interest; this is where DEER can occur. The local magnetic field experienced by a spin is affected by other nearby magnetic moments in a manner proportional to the third root of the distance; thus, when an A-spin is close enough to a B-spin flipped by the pump pulse, its local field is altered in a distance-dependent manner and its precession frequency changes accordingly. The A-spin echo expected at time 2τ will consequently have altered amplitude, because those spins precessing out of phase will detract from the bulk magnetization at that time. A DEER waveform is constructed by plotting the integrated intensity of the echo against the position of the pump pulse in time (τ). When $t = 0$, the $\pi/2$ observe pulse and the π pump pulse are simultaneous, and no modulation of echo amplitude is expected. As t increases, the effect of B-spin inversion on the phase of A-spins becomes more pronounced, resulting in an initial decay in the DEER waveform. Due to the angular nature of spin precession, the waveform eventually reaches a maximum modulation depth, and begins to oscillate about a mean echo amplitude. Both the initial decay and period of oscillation are shorter for closely interacting spins, as the distance-dependent effects on A-spin precession frequencies are more severe. Thus, the distance between two spins can be directly derived by analyzing the shape of the DEER waveform (Figure 3.7, columns). As the waveform represents an ensemble measurement, the amount of static disorder present in a sample can also be extracted, as a distribution of interspin distances leads to dampening of the observed oscillations by destructive interference (Figure 3.7, rows).

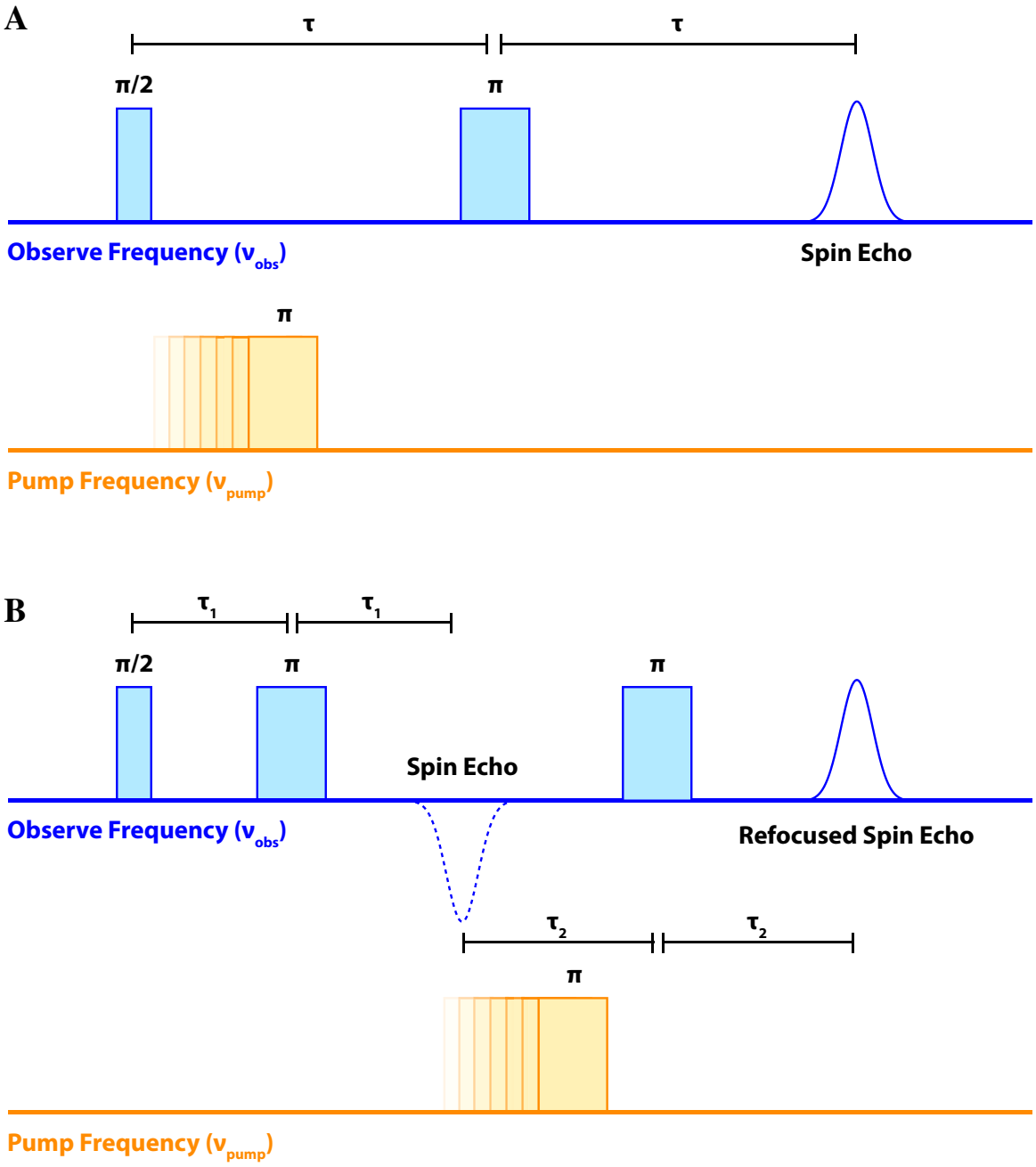

Figure 3.6. Pulse sequences for three and four-pulse DEER experiments. A: The three-pulse experiment. $\pi/2$ and π pulses are applied using the observe frequency ν_{obs} (blue), and a spin echo is subsequently observed at time 2τ. Meanwhile, a π pulse is applied between the observe pulses using the pump frequency ν_{pump} (orange). B: The four-pulse experiment. The same spin echo perturbation phenomenon is measured, but a second π pulse in the observe pulse sequence refocuses the spin echo generated after $2\tau_1$ at time$= 2\tau_1 + 2\tau_2$. This allows for the elimination of dead time in recording the DEER waveform, because the pump π pulse can now be applied on either side of the initial spin echo.

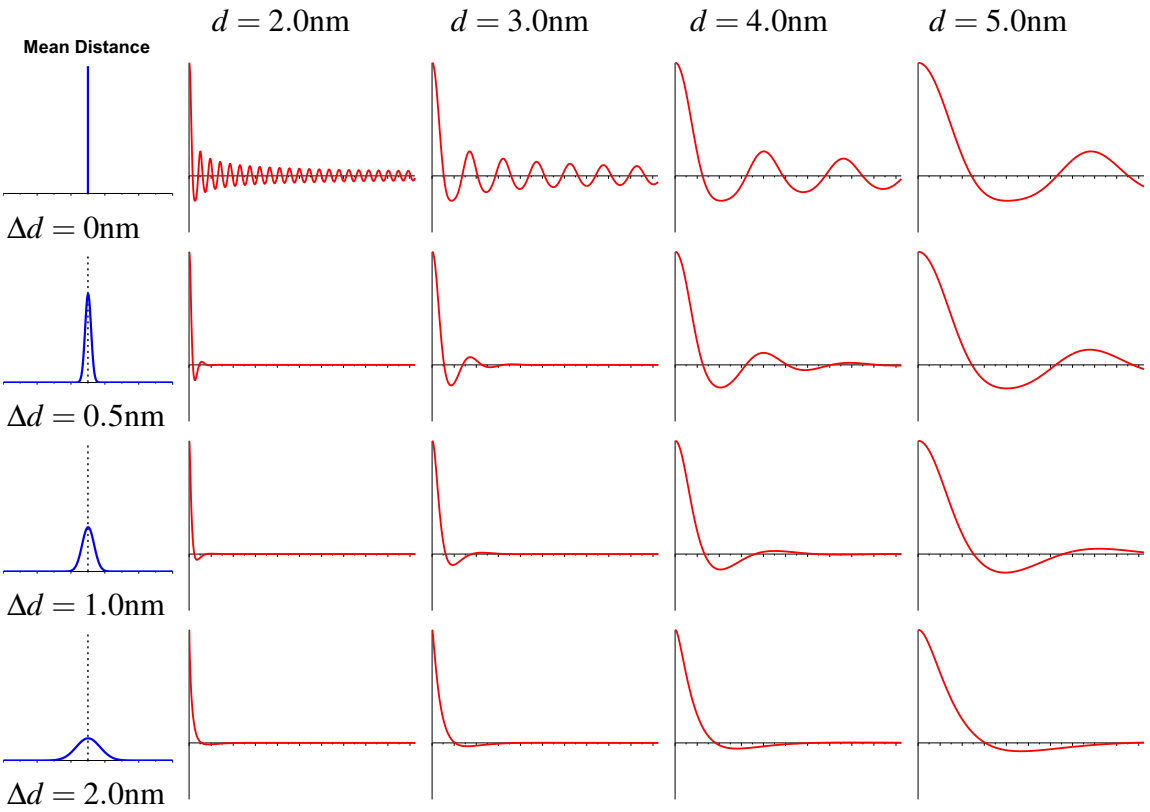

Figure 3.7. Dependence of the DEER waveform on interspin distance and disorder. Columns illustrate how the periodicity of the waveform is highly sensitive to the distance (d) between two nearby spins. Rows illustrate how disorder in the spin pair ensemble affects the amplitude of the oscillations in the waveform. Disorder is quantified here by Δd, which describes the full width at half maximum for a Gaussian distribution of distances centered at a given d. All waveforms are normalized to the modulation depth. The examples shown above effectively span the sensitive range of the DEER measurement; the row where $\Delta d = 0$ is not physical, but nonetheless useful for illustrating the theoretical decay toward a steady oscillation about the modulation depth.

The three-pulse DEER experiment described above illustrates the relevant theory, but most DEER experiments are currently conducted using a slightly modified sequence that includes four pulses (Figure 3.6B) [82]. By delivering an additional π pulse in the observe sequence, say at time τ_2 after the first spin echo, the initial spin echo will be refocused again at time $2\tau_1 + 2\tau_2$. The pump pulse positions are then stepped out between the two observe π pulses. This scheme renders the same effects on the refocused echo amplitude and produces the same waveform as a three-pulse experiment, but eliminates issues with instrument dead-time that would otherwise prevent capture of the maximum echo amplitude in the data.

In general, DEER experiments on labeled proteins suffer many of the same complications as their CW-EPR counterparts with regard to the mobility of traditional spin labels, and the accuracy and effective resolving power of the technique is hampered as a result. While nanosecond motions of significant amplitude do not occur after the sample is frozen, long linkers and broad or unpredictable ranges of motion manifest as increased disorder in the distance distribution, obscuring the true disorder present in the labeled backbone. Flexible labels also introduce ambiguity in the mean distance measurement, because the exact position of each nitroxide relative to its labeled site is not easily predicted. Thus, the intrinsic utility of both CW-EPR and DEER are limited by current conventions in SDSL methods.

3.5 The Bifunctional Spin Label

Modern efforts to improve EPR methodology for protein structure determination have varied in approach. Until recently, the prevailing strategy has been to address the common limitation of SDSL outlined above, wherein spectral contributions from the flexible label and its attached protein are unresolved. Extensive simulation studies have attempted to quantify the occupancy of rotamer states for various spin labels, so that the label and protein contributions can be effectively separated during analysis [83, 84]. Understanding the conformational dynamics of the probe is indeed a crucial avenue of study for all forms of site-directed spectroscopy, especially where precise structural measurements on the target protein (e.g. orientation, distance) are desired. However, as in other forms of spectroscopy, these rotamer libraries often prove difficult to apply generally, due to the tendency of spin labels to interact unpredictably with surrounding side chains and protein secondary structure. A spin label that becomes immobilized on a protein through favorable interactions with surface residues will exhibit entirely different behavior from a label that explores the solvent, and judicious selection of labeling sites can only moderately increase the odds of predicting this behavior. Molecular dynamics (MD) simulations may be performed on a case-by-case basis with the labeled protein fully modeled in, but such methods are very time-consuming, and are typically suitable only for observing conformational occupancy. Few current MD methods purport to give an accurate description of molecular motion on a realistic timescale, a shortcoming that is acceptable in some forms of spectroscopy but which is severely limiting for CW-EPR.

In the face of these challenges, an alternate strategy is to act on the level of experimental design: if nanosecond motion of the label could simply be eliminated, virtually all the ambiguity that plagues the SDSL method could be alleviated. Any motional effects observed in CW-EPR spectra could be reliably attributed to the target protein, and less motion in the spectra of oriented systems would help to restore their high dependence on label orientation. If the target protein was large enough and stable enough to preclude motional effects altogether, even the simulated fitting of data could be greatly simplified. The accuracy and resolution of DEER-derived distance distributions would also be improved, as positional ambiguity and ensemble disorder would be significantly reduced.

The typical nitroxide spin label contains a five- or six-membered organic ring containing the nitroxide nitrogen, flanking methyl groups to shield the nitroxyl radical from reduction, and a reactive group tethered to the ring by a flexible linker of two or more saturated bonds. There are powerful exceptions, such as the non-natural amino acid TOAC, which incorporates directly into the peptide backbone; unfortunately, however, these alternatives currently require peptide synthesis to achieve specific labeling, and are thus unsuitable for proteins greater than 50 amino acids in length [85]. The most popular label of the traditional variety is the methanethiosulfonate spin label (MTSSL), named for its reactive group, which readily forms a disulfide linkage with free cysteine residues [86]. Other examples include the iodoacetimide spin label (IASL) and the maleimide spin label (MSL), both of which also react with free cysteines but form irreversible carbon-sulfur bonds, rather than disulfides. Factors that directly impact motional ambiguity include the

number of saturated bonds in the linker, the size of the nitroxide ring structure, and the presence or absence of additional moieties.

Several variations on the basic structural formula described above have been synthesized in an effort to limit the mobility of nitroxides after labeling. Addition of bulky phenyl or pyridyl substituents on the nitroxide ring has been shown to substantially reduce nanosecond motion, though correlation times fall short of the rigid limit in aqueous solution [87]. An attractive alternate strategy involves generating a second tether to the protein backbone with a second reactive group; such an approach has been employed successfully in spectroscopy of fluorescent labels (e.g. bifunctional rhodamine). Efforts to engineer an immobilized spin label by double attachment have included the pairing of conventional methanethiosulfonate groups on the nitroxide ring with a large variety of additional reactive moieties, such as photoactivatable azido, azidonitrophenyl, or phthalimide groups (which react with nearby lysines upon irradiation), or additional methanethiosulfonate groups [88–90].

The smallest and simplest of these derivatives shares its basic structure with MTSSL, including a second (identical) methanethiosulfonate group symmetric with the first to enable bifunctional targeting of two cysteine residues [91]. This compound, referred to hereafter as the bifunctional spin label (BSL), has been shown to exhibit consistently strong immobilization relative to its attached protein. Initial applications of BSL centered on its utility as a reporter of slow (ms) protein dynamics in solution, typically measured by a variation on the standard CW technique known as saturation transfer EPR [54, 92, 93]. Beyond

these studies of molecular tumbling, however, there are features of BSL's labeling behavior that show strong potential for high-resolution structure determination. BSL is small enough to achieve bifunctional labeling through bridging of adjacent motifs within the same secondary structure, such as the successive turns of an α-helix (at residue positions i and i+4), the successive pleats of a β-strand (at positions i and i+2), or across adjacent β-strands in a β-sheet. All of these labeling strategies have been successfully implemented in model systems, and each results in CW-EPR spectra at the rigid limit [94]. Restriction of the labeling sites to a single structural element is attractive for two reasons. First, localization of the crosslinking reaction reduces the risk of significant structural perturbation by the label, while maintaining close physical proximity to the site of interest. Physical proximity has an additional advantage when coupled with the small size of the label, however: a consistent geometric relationship between the label and the target site is maintained. Crystallography has shown that the α-helix labeling scheme (i and i+4) gives rise to a well-defined portion of electron density corresponding to BSL, indicating a single predominant conformation; this observation has since been supported by MD studies of BSL modeled with the same attachment scheme [94, 95]. If BSL is indeed consistently stereospecific, this feature alone represents tremendous opportunity for protein structure determination, because spatial information about the nitroxide (reported by the EPR spectrum) could be related directly and unambiguously to the peptide backbone.

While BSL thus lends itself to a wealth of potential applications, most have not been explored beyond the initial proof of principle. Several groups have commented on the

strong immobilization of BSL determined by CW-EPR [92, 94, 96], and narrower distance distributions from DEER when compared with traditional spin labels have also been reported [94, 97]. However, these methods have yet to be applied in a context that directly provides new high resolution information about a protein's structure. DEER has not been reported with BSL on dynamic proteins where significant distance changes are expected, and no study has employed BSL in oriented systems, where the recovery of high orientational resolution in CW-EPR is perhaps the most significant potential advantage of all.

3.6 Motivation for Research (Part II)

In the previous chapter, the importance of generating accurate structural models for actin and myosin together in complex was discussed. Elucidation of the important transitions within the myosin CD that couple nucleotide hydrolysis to actin binding and force generation require high resolution models, because those movements are necessarily small and subtle. Site-directed spectroscopy can succeed in providing structural information where traditional comprehensive techniques like X-ray crystallography and cryo-EM fail, and EPR in particular possesses a robust methods toolkit for the derivation of modeling constraints. With its exquisite intrinsic sensitivity to probe orientation, and the development of pulsed experiments with high distance resolution, EPR is theoretically well-poised to determine how myosin's internal structure responds during its interactions with actin and nucleotides.

However, current SDSL methods place significant limitations on the effective resolving power of both CW-EPR and DEER. Although traditional nitroxide spin labels are typically much smaller than their fluorescent counterparts, labeling still generates a flexible linker of several saturated bonds between the nitroxide and the site of interest, introducing significant and unpredictable layers of ambiguity. Local disorder of the spin label has a severe impact on the ability of EPR to reliably report the behavior of the labeled protein, and the effects of nanosecond motion often completely ablate spectral sensitivity to orientation.

Thus, an improvement of the standard SDSL method is required to recover the true intrinsic capabilities of EPR for structure determination. The use of BSL has been shown to consistently eliminate nanosecond motion of the nitroxide relative to the protein, and in constructs that target labeling to successive turns of an α-helix, there is empirical evidence for conformational specificity. Initial studies have therefore indicated that BSL may be able to solve the major issues plaguing SDSL, but applications for novel structural insight at high resolution have not been explored.

The purpose of the present work, therefore, is twofold. First and foremost, the proceeding studies explore the hypothesis that mechanochemical coupling in the myosin CD is accomplished via small internal movements of individual structural elements, with particular focus on effects in the presence of actin. Second, in order to quantify and ultimately model these internal changes, the proceeding studies incorporate rigorous methods development for the derivation of structural constraints from EPR, using BSL to achieve the required spectral resolution.

CHAPTER 4: HIGH-RESOLUTION HELIX ORIENTATION IN ACTIN-BOUND MYOSIN DETERMINED WITH A BIFUNCTIONAL SPIN LABEL

[1]Benjamin P. Binder, [1]Sinziana Cornea, [1]Andrew R. Thompson, [2]Rebecca J. Moen, and [1]David D. Thomas*

[1]Department of Biochemistry, Molecular Biology and Biophysics, University of Minnesota, Minneapolis, MN 55455
[2]Department of Chemistry and Geology, Minnesota State University, Mankato, MN 56001

* To whom correspondence should be addressed: ddt@umn.edu

Published in *Proc. Natl. Acad. Sci. USA*, Volume 112, Issue 26, pp. 7972-7

4.1 Chapter Summary

Using electron paramagnetic resonance (EPR) of a bifunctional spin label (BSL) bound stereospecifically to Dictyostelium myosin II, we have determined with high resolution the orientation of individual structural elements in the catalytic domain while myosin is in complex with actin. BSL was attached to a pair of engineered cysteine side chains four residues apart on known α-helical segments, within a construct of the myosin catalytic domain that lacks other reactive cysteines. EPR spectra of BSL-myosin bound to actin in oriented muscle fibers showed sharp 3-line spectra, indicating a well-defined orientation relative to the actin filament axis. Spectral analysis indicated that orientation of the spin label can be determined within < 2.1 degrees accuracy, and comparison with existing structural data in the absence of nucleotide indicates that helix orientation can also be determined with < 4.2 degrees accuracy. We used this approach to examine the crucial ADP-release step in myosin's catalytic cycle, and have detected reversible rotations of two helices in actin-bound myosin in response to ADP binding and dissociation. One of these rotations has not been observed in myosin-only crystal structures.

4.2 Introduction

The myosin family of molecular motors is responsible for numerous vital functions in eukaryotes, including the contraction of striated muscle. Bundled within an intricate and highly-regulated myofibril lattice, muscle myosin II converts the chemical energy released by ATP binding and hydrolysis into mechanical work, executing a series of structural transitions that generate force on actin and shorten each muscle cell [24, 98]. Coupling of actin binding, nucleotide hydrolysis, and lever arm movement within myosin's catalytic domain (CD) is essential for proper function of the contractile apparatus [99, 100].

Myosin function requires actin, and thus an understanding of its mechanism requires analysis of both proteins in complex. However, no crystals of actin-myosin complexes have been reported, so the resolution of actin-bound myosin structures is currently limited to that of electron microscopy. Furthermore, x-ray crystallography and electron microscopy produce only static structures in frozen or crystalline environments, which cannot accurately render dynamics, disorder, or transitions between states, which are essential to understanding function and pathology [70, 100].

In contrast, site-directed spectroscopy can be used to examine the actin-myosin complex under more physiological conditions. Both fluorescence and electron paramagnetic resonance (EPR) have been used in complement to examine the structural dynamics of myosin bound to actin [101, 102]. EPR offers superior orientational resolution, due to the high sensitivity of the EPR spectrum to alignment of a spin label in the applied magnetic

field. A well-placed spin label can provide direct information about orientation and dynamics in the vicinity of the labeling site, a strategy that has proven powerful in the study of myosin in oriented muscle fibers [102–104]. However, conventional methods for site-directed spin labeling impose significant limits on the effective resolving power of EPR. Spin labels are typically incorporated into proteins through covalent attachment to Cys, resulting in a flexible linker that permits the label to undergo nanosecond rotational motion independent of the peptide backbone. Such motion obscures the orientation dependence of the spectrum [105, 106].

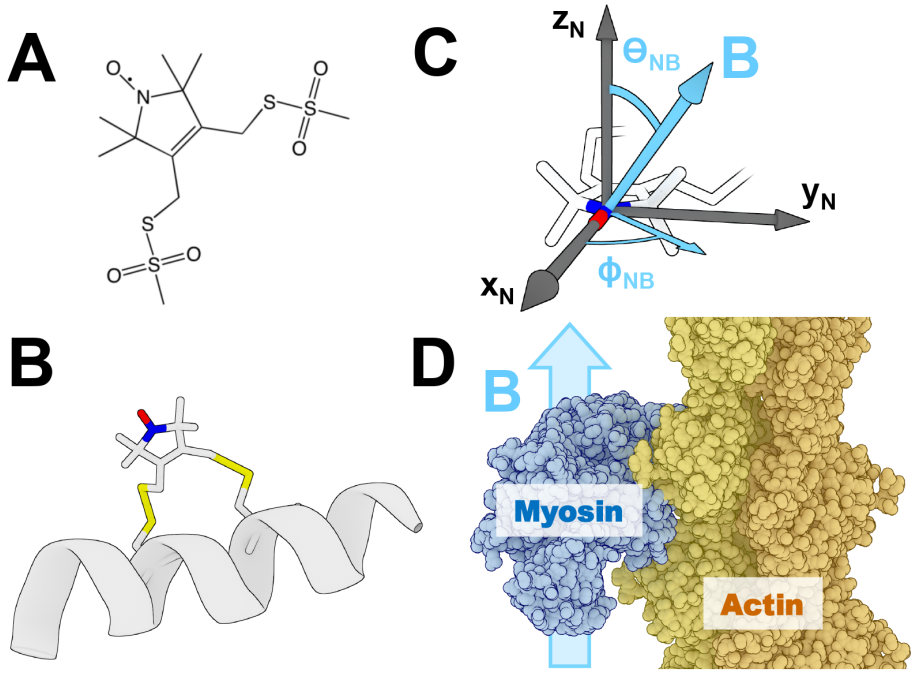

Figure 4.1. Overview of bifunctional spin labeling and EPR on oriented fibers. A: Chemical structure of BSL. B: BSL bound stereospecifically to an α-helix at positions i and i+4, as in [94]. C: Angles θ_{NB} and ϕ_{NB} that define the orientation of the nitroxide spin label (defined by axes x_N, y_N, z_N) relative to the applied magnetic field $\vec{B}$, which directly determine the orientation dependence of the EPR spectrum. D: Orienting the helically ordered muscle fiber (and thus the actin filament axis) with $\vec{B}$ permits direct measurement of the nitroxide orientation relative to actin.

Our solution is to eliminate local probe motions by employing a spin label that becomes strongly and stereospecifically immobilized with respect to the target protein upon attachment. In site-directed fluorescence, this has been achieved by using probes that react with di-Cys [107–109] or tetra-Cys [110] labeling sites, but these fluorescent probes are typically at least twice the size of spin labels, and fluorescence lacks the high orientational resolution of EPR [101, 102]. The spin-labeled amino acid TOAC provides stereospecific attachment to the peptide backbone, but this probe is currently only practical for peptides on the order of 50 amino acids or less [85]. For larger proteins, spin labels have been synthesized with bulky substituents to reduce mobility [87], or substitution with additional reactive moieties to confer bifunctionality [88, 89, 91]. The smallest and simplest of these derivatives shares its basic structure with the widely-used methanethiosulfonate spin label (MTSSL), with a second MTS group that allows bifunctional targeting of two Cys residues [91] (Fig. 4.1A). This bifunctional spin label (BSL) is rigidly immobilized when reacted with a pair of Cys residues, so that it undergoes negligible nanosecond rotational motion relative to the protein and can thus be used reliably to measure microsecond protein rotational motions by saturation transfer EPR [54, 92, 93].

Crystallography has shown that BSL exhibits a rigid and stereospecific linkage when reacted with Cys four residues apart on successive turns of an α-helix, with great potential for accurate spin-spin distance measurements (Fig. 4.1B) [94]. However, the potential advantages of BSL for enhanced orientational resolution have not been explored. We hypothesize that if BSL is employed in the context of an intrinsically-oriented system (e.g.,

myosin in the myofilament lattice), the resolution of EPR will be sufficient to detect the orientation of individual protein structural elements with unprecedented accuracy (Fig. 4.1C, D).

4.3 Results

4.3.1 Comparison of spectra from myosin labeled with BSL and MTSSL.

A solvent-exposed location on the C-terminal end of myosin's relay helix was chosen for initial study, because crystal structures and spectroscopic studies of isolated myosin have shown that the orientation of this helical segment is sensitive to nucleotide binding [19, 56, 111]. MTSSL was reacted monofunctionally at position 492 (Fig. 4.2A, upper), and BSL was reacted bifunctionally at positions 492 and 496 (Fig. 4.2A, lower; Fig. 4.2B).

Skinned muscle fiber bundles, decorated with spin-labeled S1dC in the absence of nucleotide ("rigor"), were oriented either parallel or perpendicular to the spectrometer's applied magnetic field. Spectra from monofunctionally labeled (MTSSL) protein show virtually no dependence on fiber orientation (Fig. 4.2C, left), indicating that the spin label ensemble is not well ordered in the myofilament lattice. In contrast, BSL spectra are highly sensitive to fiber orientation (Fig. 4.2D, left), implying orientational order of the spin label relative to the myosin CD, and of the myosin CD relative to actin.

Spectra of minced (randomly oriented) fibers show no dependence on sample orientation, as expected (red and blue spectra identical in Fig. 4.2C-D, right), but the spectra of monofunctionally (C) and bifunctionally (D) attached probes are quite different. Since

these samples lack orientation, such differences can only arise from nanosecond rotational motion. The BSL spectrum has a "powder" lineshape, with a wide splitting of 71.2 ± 0.2 G between the outer extrema, indicating no significant nanosecond rotational motion (Fig. 4.2D right). Thus BSL is strongly immobilized and highly ordered at this site, enabling it to directly report structural states in an oriented system. In contrast, the spectrum of mono-functional MTSSL bound to the same site shows substantial narrowing (Fig. 4.2C right), indicating large-amplitude dynamic disorder on the nanosecond timescale.

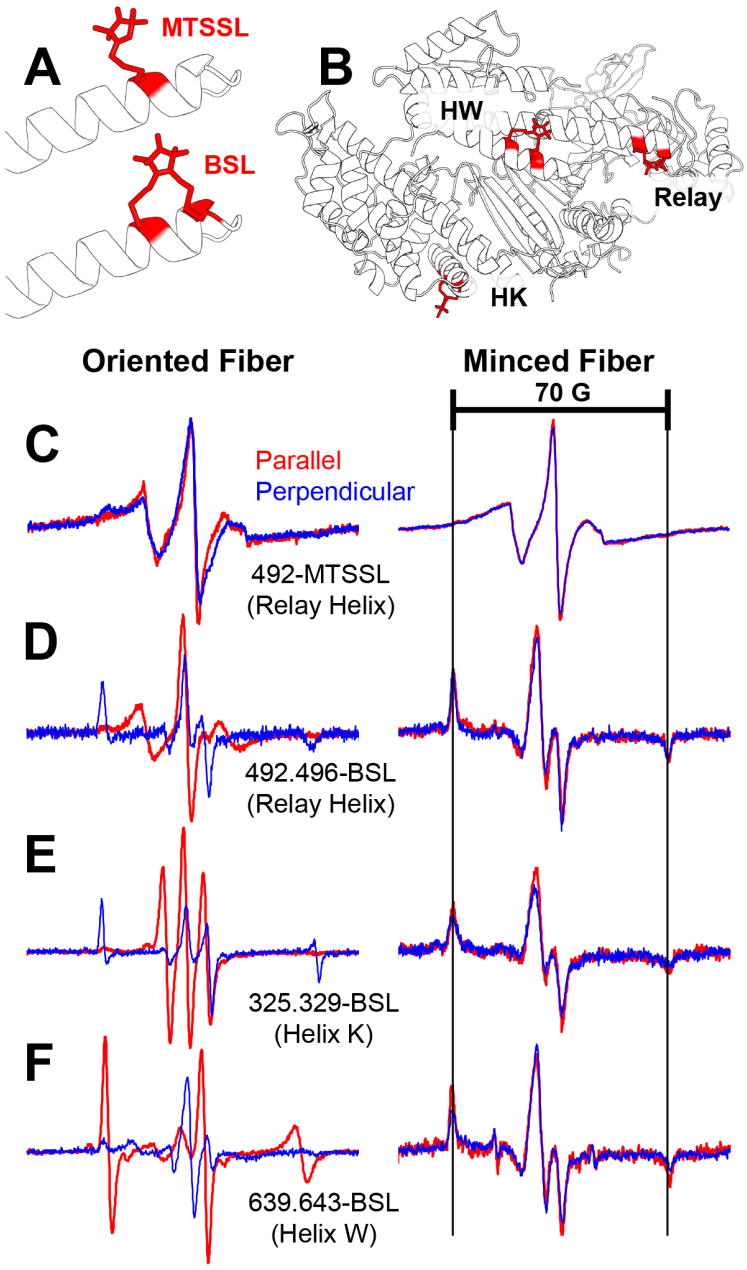

Figure 4.2. Comparison of oriented fiber EPR spectra in parallel and perpendicular orientations. A: MTSSL and BSL on the relay helix. B: BSL labeling sites chosen on three stable helices throughout the myosin CD. C-F: Left: EPR spectra of the spin-labeled constructs on oriented fiber bundles, in the absence of nucleotide (rigor), with the fiber axis aligned parallel (red) and perpendicular (blue) to the magnetic field. Right: EPR spectra of randomly-oriented (minced fiber) preparations of all spin-labeled constructs. C: S1dC labeled at residue 492 with MTSSL (relay helix). D: S1dC labeled at residues 492 and 496 with BSL (relay helix, bifunctional analog to C). E: S1dC labeled at residues 325 and 329 with BSL (Helix K). F: S1dC labeled at residues 639 and 643 with BSL (Helix W).

4.3.2 BSL is strongly immobilized and ordered on myosin at sites across the CD.

We generated two additional myosin constructs with bifunctional labeling sites on Helix K (325C and 329C) and Helix W (639C and 643C), located respectively in the upper and lower 50kDa domains that form myosin's actin-binding cleft (Fig. 4.2B). In all three cases, spectra of oriented fibers show very sharp lines that are quite sensitive to fiber orientation (Fig. 4.2D-F, left), consistent with highly ordered probes. Spectra of minced fibers all exhibit identical lineshapes between sample cell orientations (Fig. 4.2D-F, right) and show a very wide outer splitting, indicating strong immobilization on the nanosecond timescale. Spectra of fibers oriented parallel to the field (Fig. 4.2D-F left, red) are clearly different across all sites, indicating that probes at these sites have distinct orientations relative to the fiber (actin) axis.

4.3.3 Spin-labeling with BSL does not significantly alter myosin function.

Actin-activated ATPase assays were performed on all BSL-labeled and unlabeled di-Cys myosin samples in order to assess the effect of labeling on protein function (Fig. 4.6, Table 4.3). Extent of labeling on BSL-labeled samples was determined by spin-counting; spin-to-protein ratios approaching 1 were obtained for all 3 constructs (Table 4.3), demonstrating virtually complete bifunctional labeling. In addition, spectra of single- and di-Cys constructs share no significant features in oriented fibers, indicating the negligible presence of monofunctionally-attached BSL (Fig. 4.2C-D, Fig. 4.7). For all 3 constructs, substantial actin activation of myosin ATPase was observed for both labeled and unlabeled samples

(Fig. 4.6, Table 4.3). There was significant variation among the three constructs, but the observed kinetics fall within the range previously observed for Dicty myosin S1dC [26, 40], and labeling affected neither $V_{\max}$ nor K_{ATPase} by more than a factor of two. Thus, labeling does not alter the fundamental mechanism of myosin's enzymatic activity.

4.3.4 BSL orientation relative to actin is determined by direct spectral simulation and fitting.

The results in Fig. 4.2 show that BSL undergoes negligible nanosecond rotational motion, so the shape of the spectrum is dictated entirely by the orientation of the nitroxide spin label (N) relative to the instrument's static magnetic field ($vecB$), defined by θ_{NB} and ϕ_{NB} (Fig. 4.1C). Thus, when spectra are acquired with the muscle fiber (actin filament) axis parallel to the magnetic field (Fig. 4.1D), spectra directly report the orientational distribution of the nitroxide spin label relative to actin [103, 104, 112], defined by θ_{NA} and ϕ_{NA}, which are identical to θ_{NB} and ϕ_{NB} (Fig. 4.1C). Therefore, we focus on spectra acquired using the parallel fiber alignment.

We determined the orientational distribution in each sample through least-squares fitting of EPR data to spectral simulations (Fig. 4.8), as described previously [103, 104, 112] (see also section 3.2). First, magnetic and hyperfine tensors were obtained by fitting spectra acquired from minced fibers (Fig. 4.2D-F, right), assuming immobile and randomly oriented spin labels. After fixing these values, analysis of oriented samples depends exclusively on θ_{NA} and ϕ_{NA} (Fig. 4.1). Each spectrum was assumed to arise from a distribution of static probe orientations relative to the applied magnetic field $\vec{B}$ (here equivalent to the

	Actin-BSL axial angle, θ_{NA} (°)	
	Apo (rigor)	5mM MgADP
492.496-BSL (Relay Helix)	70.5 ± 0.1	60.9 ± 0.2
325.329-BSL (Helix K, U50)	88.2 ± 0.5	89.2 ± 0.6
639.643-BSL (Helix W, L50)	28.0 ± 0.1	25.0 ± 0.3
	Actin-BSL azimuthal angle, ϕ_{NA} (°)	
	Apo (rigor)	5mM MgADP
492.496-BSL (Relay Helix)	27.0 ± 1.8	13.6 ± 2.4
325.329-BSL (Helix K, U50)	33.3 ± 1.8	35.3 ± 1.0
639.643-BSL (Helix W, L50)	32.6 ± 2.1	22.6 ± 1.8
	Angular width FWHM, $\Delta\theta, \phi$ (°)	
	Apo (rigor)	5mM MgADP
492.496-BSL (Relay Helix)	11.9 ± 1.5	18.1 ± 0.7
325.329-BSL (Helix K, U50)	10.0 ± 1.7	9.2 ± 0.2
639.643-BSL (Helix W, L50)	10.4 ± 0.2	9.9 ± 0.7

Table 4.1. Orientation of the myosin-bound nitroxide spin label (N) relative to the actin (fiber) axis (A), derived from spectra of muscle fibers oriented parallel to the magnetic field (Fig. 4.3). Values are mean ± SEM $(n = 3)$.

actin filament axis A). Spectra were fitted allowing for the presence of up to two independent populations, each characterized by central angles θ_{NA} and ϕ_{NA}, and a Gaussian full width at half maximum $(\Delta\theta, \phi)$ describing static disorder of the ensemble. For each of the three BSL samples, one principal oriented Gaussian component was observed (Fig. 4.8), and that component is displayed in Fig. 4.3B, with parameters given in Table 4.1.

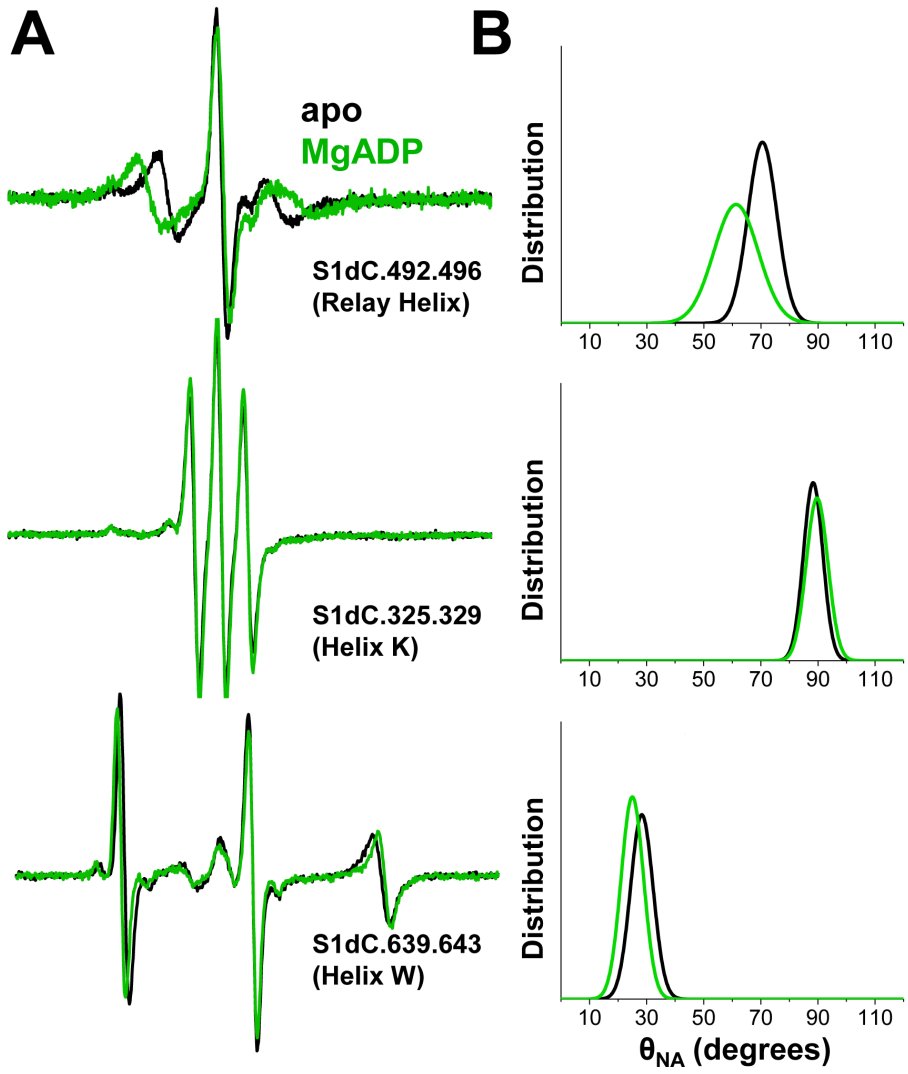

Figure 4.3. Orientational distributions for myosin helices in absence of nucleotide and presence of MgADP. A: BSL-labeled myosin bound to actin in skinned muscle fibers in the absence of nucleotide (black) and the presence of 5mM MgADP (green). B: θ_{NA} distributions for nucleotide-free (black) and ADP-bound (green) biochemical states, obtained by spectral simulation and least-squares fitting of the data in A.

4.3.5 BSL resolves significant structural changes in the force-generating domain of myosin during ADP binding and release.

Next, we asked whether this approach is capable of resolving transitions between distinct nucleotide-dependent structural states. We focused on identifying differences between nucleotide-free and MgADP-bound complexes, because of the physiological relevance of the ADP-release transition (see Discussion).

We acquired spectra from oriented fibers in the absence (black) and presence (green) of 5mM MgADP (Fig. 4.3A) by switching the source of peristaltic flow through the fiber capillary. After acquisition in the presence of MgADP, flow was switched back to a nucleotide-free solution containing 10mM EDTA, to dissociate the residual bound ADP. In all cases this spectrum was identical to that of the original nucleotide-free sample.

In the relay helix construct, a marked increase in the outer splitting was observed with MgADP (Fig. 4.3A, top). Subsequent fitting revealed that this corresponds to a change in θ_{NA} of $-9.6^\circ \pm 0.3^\circ$, a change in ϕ_{NA} of $-13.4^\circ \pm 4.2^\circ$, and a change in disorder $(\Delta\theta, \phi)$ of $+6.2^\circ \pm 2.2^\circ$ (FWHM) (Fig. 4.3B, Table 4.1). In the Helix K construct (upper 50kDa domain), no significant changes were detected (Fig. 4.3, middle; Table 4.1). In the Helix W construct (lower 50kDa domain), a significant increase in outer splitting was observed, corresponding to a change in θ_{NA} of $-3.0^\circ \pm 0.4^\circ$, and a change in ϕ_{NA} of $-10.0^\circ \pm 3.9^\circ$; there was no significant change in disorder (Fig. 4.3, bottom; Table 4.1). The different effects observed in these three helices indicate ADP-induced structural changes internal to

the CD, rather than a concerted rotation of the entire domain relative to actin.

4.3.6 Helix orientation with respect to actin.

Angles in Fig. 4.3 and Table 4.1 correspond to θ_{NA} and ϕ_{NA}, defined by the relative orientation of BSL and the actin filament (Fig. 4.4A,B). In order to develop structural constraints that are independent of the spin label, we considered the spatial relationship between the label and its associated α-helix. BSL is highly ordered at all sites tested, indicating that the label is stereospecific in its attachment, so our data support the use of a single model to define the label-helix relationship. We started with a crystal structure of BSL attached to T4 lysozyme at positions i and i+4 on an α-helix (PDB: 3L2X) [94]. We determined the axis of the labeled helix using a technique previously described [113], and defined a nitroxide reference frame using the geometry of BSL (Fig. 4.4C). Vector algebra yields two new angles, θ_{NH} and ϕ_{NH}, which describe the orientation of the helix vector in the nitroxide frame (Fig. 4.4D). With both helix and actin vectors defined in the nitroxide reference frame, the angle between them (θ_{AH}) describes the tilt of the myosin helix with respect to the actin filament (Fig. 4.4E,F).

To verify our derivation, we compared the helix orientations calculated from our nucleotide-free EPR results to a recent model of the actomyosin complex, assembled from cryo-EM and crystallographic data on nucleotide-free myosin II in complex with rabbit skeletal actin [114]. In this model, θ_{AH} values were measured for the three labeled helices relative to the actin axis, and these values were compared with the centers of our experimental θ_{AH} distributions. Table 4.2 shows that each EPR experiment produces a θ_{AH} value

	Initial ($\theta_{NH} = 74.2°, \phi_{NH} = -73.8°$)		
	Model-Based θ_{AH} (°)	Model-Based θ_{AH} (°)	Difference (°)
Relay Helix (apo)	84.4	74.8 ± 1.8	-9.5 ± 1.8
Helix K (U50)	29.6	42.3 ± 1.9	12.7 ± 1.9
Helix W (L50)	77.5	83.5 ± 2.1	6.0 ± 2.1
	Optimized ($\theta_{NH} = 74.9°, \phi_{NH} = -61.2°$)		
	Model-Based θ_{AH} (°)	Model-Based θ_{AH} (°)	Difference (°)
Relay Helix (apo)	84.4	83.4 ± 1.8	-1.0 ± 1.8
Helix K (U50)	29.6	30.6 ± 1.9	0.9 ± 1.9
Helix W (L50)	77.5	78.4 ± 2.1	1.0 ± 2.1

Table 4.2. Axial tilt angles of labeled helices with respect to actin in the absence of nucleotide. Values are derived using probe orientations obtained either from EPR ("Experimental" columns) or directly from a cryo-EM model of actomyosin ("Model-Based" column) [114].

that gives good agreement with the model calculation, with a difference of $12.7° \pm 1.9°$ in the most extreme case.

While all labeling sites on our myosin constructs were chosen within straight helices, the T4 lysozyme helix used in our derivation is kinked at the labeling site. It is likely that BSL's conformation on straight helices is different from that observed in this crystal, and we hypothesized that this discrepancy could account for some of the observed disagreement in θ_{AH} values. We varied the angles θ_{NH} and ϕ_{NH}, assuming the same values at all three sites, to minimize the difference between experimental and model-based results, yielding the optimized values given in Table 4.2. It is striking to observe that a small change in θ_{NH} and ϕ_{NH} is sufficient to bring all three of the experimental θ_{AH} angles to within 1 degree of their model-based predictions. This result demonstrates that we can obtain structural

constraints for the actomyosin complex using our EPR-based method that are in precise agreement with previous literature, while avoiding the inherent difficulties and caveats associated with frozen and crystalline samples. The agreement across all three labeling sites, when a single conformation of BSL is assumed, provides further evidence that BSL is indeed highly stereospecific in its attachment to α-helices.

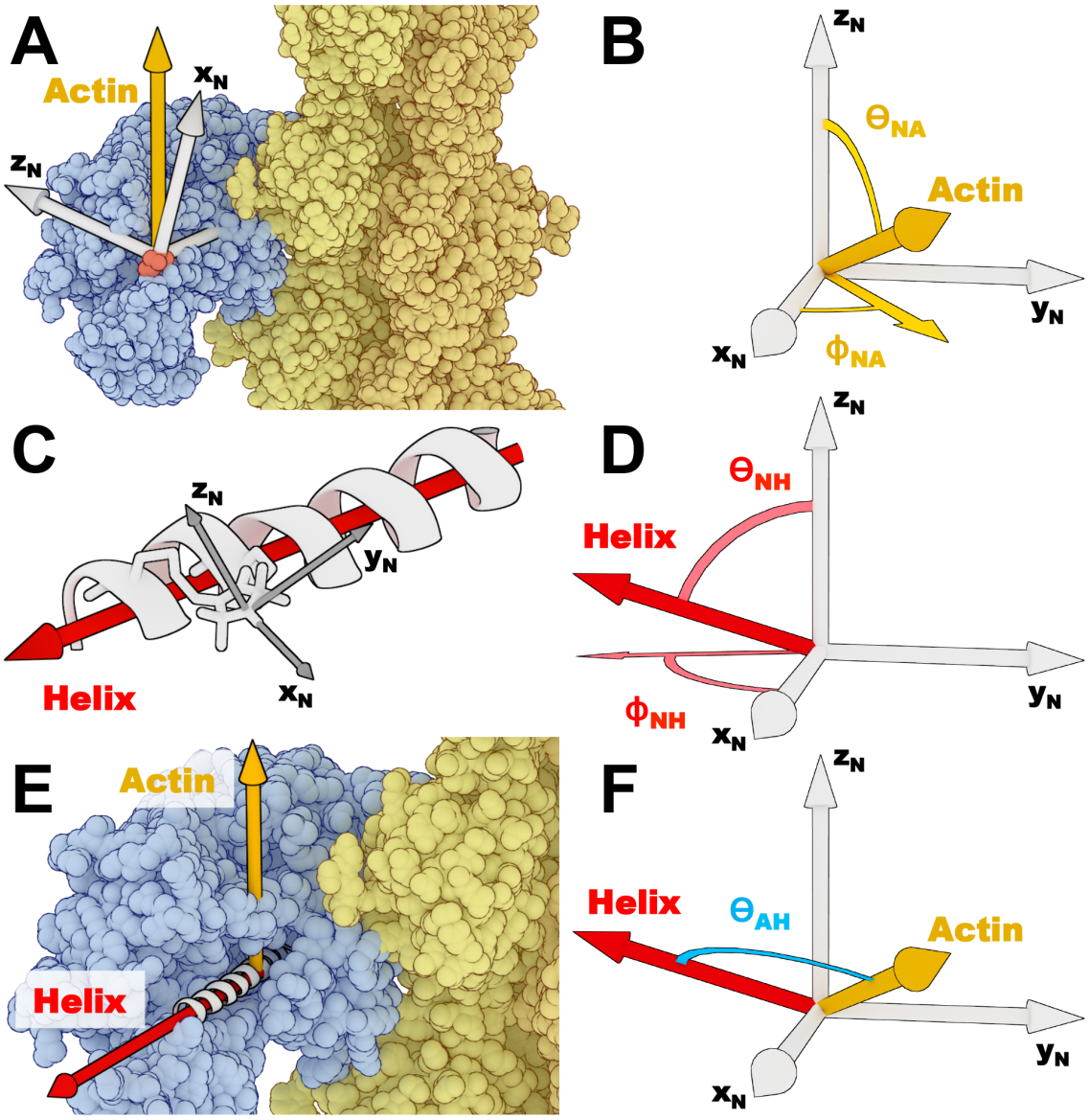

Figure 4.4. Visualization of coordinate transformations. A: Actin (yellow) in complex with myosin S1 (blue) labeled with BSL (red). The actin long axis (gold, same as the magnetic field axis B in Fig. 4.1C, since fibers are aligned parallel to $\vec{B}$) has a well-defined orientation within BSL's nitroxide coordinate frame (white), defined by angles θ_{NA} and ϕ_{NA} (B). C: BSL bound to a helix, with the nitroxide frame (gray) and helix axis (red) highlighted, defining angles θ_{NH} and ϕ_{NH} that describe the helix orientation relative to BSL (D). E: Actin (yellow) and myosin (blue) in complex, as in A, showing the two vectors of interest, actin (gold) and a representative helix axis (red), defining angle θ_{AH} between them (F).

4.3.7 Effects of ADP on helix orientation.

For the relay helix site, our results are consistent with crystal structures and previous spectroscopic studies on actin-free myosin, which show evidence of a nucleotide-dependent deformation in the C-terminal end of the relay helix [56, 115–117] (Fig. 4.5A). In each of these structures, a kink in the helix is introduced at residue M486. To model the changes in myosin reflected by EPR data, we assume that the observed reorientation of BSL corresponds to movement at the end of the relay helix, comprising residues 486 through 496. Analysis of MgADP spectra using our optimized θ_{NH} and ϕ_{NH} values (Table 4.2) yields a set of 4 potential relay helix orientations (θ_{AH}) in the presence of MgADP. Comparison to an alignment of myosin-only crystal structures highlights the most likely solution: a θ_{AH} value of $71.0° \pm 2.4°$ (Fig. 4.5B, green) places the helix in good alignment with crystal structures of myosin with nucleotide, and reflects a conformation highly similar to the MgADP-bound structures observed *in crystallo*. The other solutions bend the relay helix in a direction directly opposite from the crystal structures, or else deform the helix so severely as to disrupt its secondary structure. Thus, we conclude that the change observed by EPR correlates with a reorientation of the relay helix from $83.4° \pm 1.8°$ to $71.0° \pm 2.4°$ relative to the actin filament ($\Delta\theta_{AH} = -12.4° \pm 3.9°$) (Fig. 5B,C). The helix also becomes more disordered with the addition of MgADP ($\Delta\Delta\theta_{AH} = +6.2° \pm 2.2°$) (Fig. 4.5C).

In contrast to the relay helix, the orientation of Helix W is virtually invariant in myosin-only crystal structures. Thus it is not clear whether our observed change corresponds to an internal bending of the helix, or to a reorientation of the entire helix. However,

repeating the analysis discussed above and assuming that the helix behaves as a rigid rod, the best solution gives a change in θ_{AH} of $-4.7° \pm 1.1°$, pulling Helix W away from the bent relay helix.

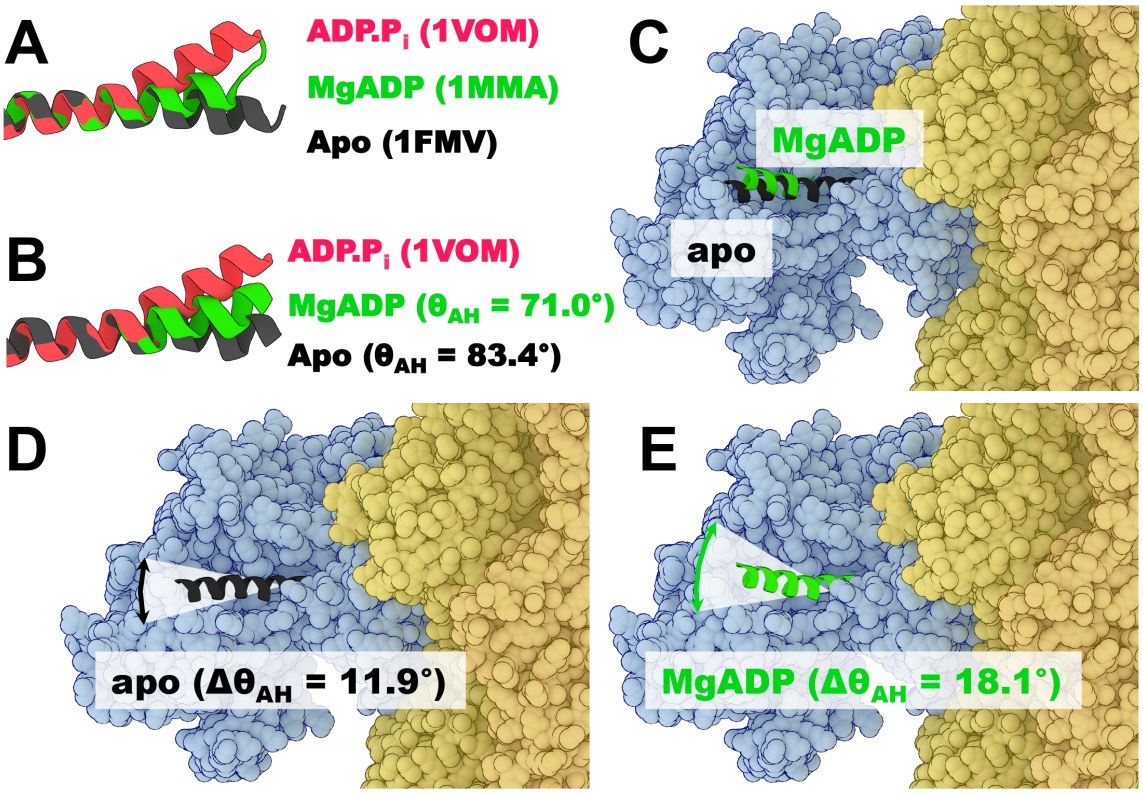

Figure 4.5. Effects of MgADP on relay helix orientation. A: Structural alignment of three Dicty myosin relay helix crystal structures, showing the nucleotide-induced C-terminal bend. B: Relay helix from our actomyosin model [114], showing the EPR-derived change induced by ADP (black to green), with the ADP.Pi structure from A shown for reference. C: Actin (yellow) in complex with myosin (blue), with EPR-derived mean relay helix orientations highlighted. D-E: EPR-derived amplitudes of angular disorder.

4.4 Discussion

4.4.1 BSL greatly enhances the resolution of EPR within oriented systems.

Bifunctional derivatives of nitroxide spin labels simplify EPR spectra by reducing nanosecond probe motion and disorder. Here we have shown the power of this technology in intrinsically oriented systems, granting EPR the capacity to measure absolute orientations of individual protein structural elements.

Previously, it was possible to detect changes in protein structure by observing shifts in orientation and mobility of spin labels at well-chosen sites. While informative, these results were typically unsuitable for accurate structural interpretation because of the weak coupling between probe and backbone [118]. Measuring orientations precisely required the use of synthetically-incorporated groups such as the amino acid TOAC, which are difficult to employ in proteins too large to synthesize [102]. The alternative presented here allows for the introduction of rigidly-attached probes post-expression, enabling high orientational resolution for structural elements within much larger targets. We have demonstrated here that BSL consistently becomes strongly immobilized and well oriented on α-helices in myosin across multiple sites throughout the CD (Fig. 4.2). The result is a single, dominant, narrow angular distribution in oriented samples, implying a high degree of stereospecificity at each site (Fig. 4.3, Table 4.1). Our derivations of helix-to-actin angles reinforce this observation, and provide strong evidence that BSL binds all three target helices with a well-defined preferred conformation (Fig. 4.4, Table 4.2).

4.4.2 ADP induces internal structural changes within the CD in actin-bound myosin.

The physiological significance of the myosin ADP-release step has become increasingly apparent. Actin decreases myosin's ADP affinity by a factor of roughly 100 [119, 120], implying crucial allosteric coupling between the nucleotide-binding pocket (ATPase) and the actin-binding interface (crossbridge dynamics). Strain on the lever arm affects the rate of ADP release in several myosins [31, 121–123], and single-molecule studies have correlated this rate with lever arm movement [31, 32]. Thus ADP release is directly related to a mechanical event that either represents the completion of the powerstroke, or functions as a load-dependent tuning mechanism [123]. Electron microscopy of smooth muscle myosin bound to actin shows a significant effect of ADP on the orientation of the lever arm relative to the catalytic domain [124]. Thus a large body of evidence suggests an important structural change within the CD of myosin that affects both actin binding and lever arm position upon ADP release, but a direct measurement of this internal structural change has not previously been provided for actin-bound myosin.

We have employed BSL to probe specific sites on myosin while the protein is in complex with actin. We observe a reversible change in label orientation at the relay helix site upon addition and removal of MgADP (Fig. 4.3, Table 4.1). Deriving the orientation of the labeled helix from EPR data (Fig. 4.4), we calculate a change of $-12.4° \pm 3.9°$ in the orientation of the relay helix relative to actin (Fig. 4.5). These results align well with existing crystal structures of myosin alone, but have not previously been observed within the actomyosin complex. We also detect a change of $-4.7° \pm 1.1°$ in the orientation of Helix

W relative to actin. This change is not observed in myosin-only crystal structures, and thus serves as a rare example of actin directly modulating myosin's structural dynamics. Further characterization of this behavior with additional labeling sites may help to refine our understanding of the mechanism behind actin activation of myosin ATPase.

4.4.3 Additional labeling sites would provide more detailed structural information.

These results demonstrate BSL's potential for dramatically improving the accuracy of structure determination in an oriented assembly. While BSL's high EPR resolution permits the precise determination of helix axial tilt angles in myosin with respect to actin (θ_{AH}), the measurements taken here are not sensitive to the orientation of the helix in the plane normal to the actin filament. This missing information means that a single labeling site on a helix cannot completely define how that helix is oriented within each myosin head, in a way that would allow direct modeling *de novo*. Such ambiguity should be alleviated by combining this approach with distance measurements between pairs of sites, detected by dipolar spin-spin interaction [94, 97]. This would be essentially equivalent to the approach employed in structure determination by NMR, where both orientation and distance constraints are combined [125]. The superior sensitivity of EPR makes it applicable to rapid measurements in dynamic samples, such as contracting muscle fibers; such measurements are needed to resolve crucial questions about the structural transitions that generate contractile force. The present work introduces a powerful application of EPR to intrinsically-oriented biological systems in general, allowing for the derivation of accurate structural constraints not only for

sarcomeric proteins, but also for proteins associated with nucleic acid chains, microtubules, and lipid bilayers.

4.5 Methods

4.5.1 Protein and muscle fiber preparations.

Mutant myosin constructs were prepared in a "Cys-lite S1dC" Dictyostelium myosin II background truncated at residue 758 and containing only one native (non-reactive) cysteine at position 655 [126]. Constructs were expressed and purified from Dictyostelium orf+ cells. Skinned rabbit psoas muscle fiber bundles were dissected and permeabilized as described previously [127].

4.5.2 EPR Spectroscopy.

EPR spectra were recorded at X-band (9.6 GHz) using an E500 EleXsys spectrometer (Bruker Instruments). Acquisition of spectra for oriented samples was performed as described previously [54, 92]. BSL spectra were analyzed to determine the orientational distribution of the nitroxide coordinate frame with respect to the applied magnetic field for parallel-oriented samples, using computational simulation and least-squares minimization as described previously [103, 112].

A detailed description of methods and reagents can be found in Section 4.6, Supplementary Information.

4.6 Supplementary Information

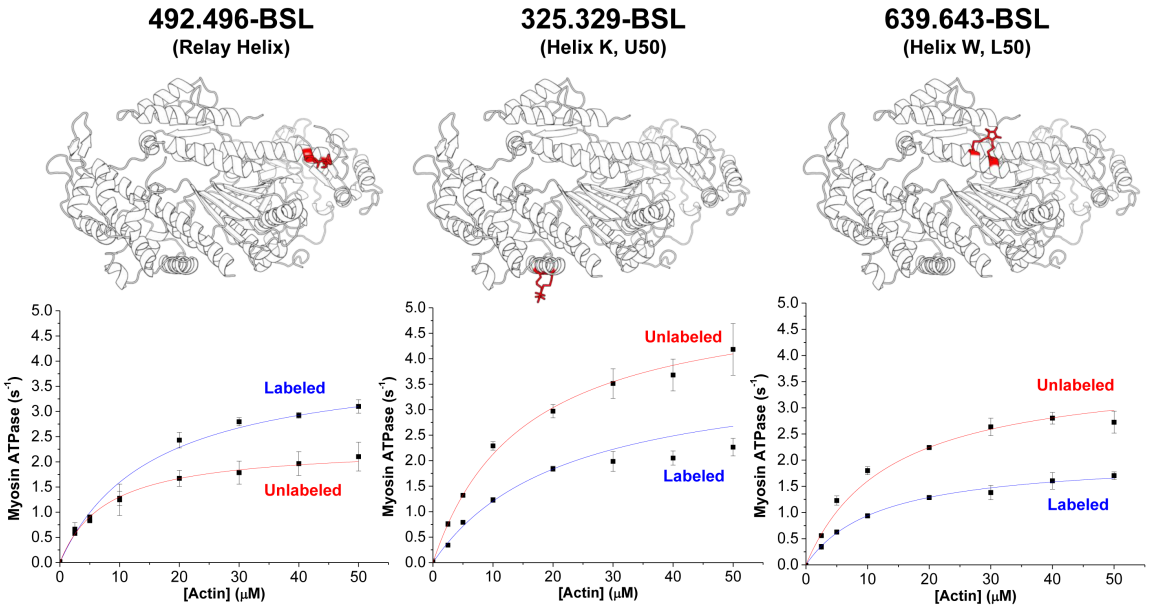

Figure 4.6. Actin-activated ATPase data for bifunctional constructs. Top: Di-Cys myosin S1dC constructs with labeling sites highlighted and spin labels modeled in red. Bottom: actin-activated ATPase data for each mutant construct, before labeling (red) and after labeling with BSL (blue). Errors are SEM ($n = 3$).

	Unlabeled		
	V_{max} (s^{-1})	K_{ATPase} (μM)	Spins/Protein
492.496-BSL (Relay Helix)	2.32 $\pm$ 0.10	7.77 $\pm$ 0.75	-
325.329-BSL (Helix K, U50)	5.33 $\pm$ 0.30	15.06 $\pm$ 1.19	-
639.643-BSL (Helix W, L50)	3.75 $\pm$ 0.18	13.43 $\pm$ 1.51	-
	BSL-labeled		
	V_{max} (s^{-1})	K_{ATPase} (μM)	Spins/Protein
492.496-BSL (Relay Helix)	4.05 $\pm$ 0.30	15.40 $\pm$ 1.60	0.97
325.329-BSL (Helix K, U50)	3.85 $\pm$ 0.99	22.00 $\pm$ 7.06	0.87
639.643-BSL (Helix W, L50)	2.05 $\pm$ 0.06	11.80 $\pm$ 0.78	0.96

Table 4.3. Actin-activated ATPase activity of Dicty S1dC constructs. V_{max} is the activity at saturating actin, and K_{ATPase} is the actin concentration needed for half-maximal activation ($V = V_{max}/2$). Errors are $\pm$ SEM ($n = 3$). Label-to-protein ratios were determined by spin counting.

4.6.1 Protein and muscle fiber preparations.

Mutant myosin constructs were prepared in a "Cys-lite S1dC" *Dictyostelium* myosin II background truncated at residue 758 and containing only one native (non-reactive) cysteine at position 655 [126], using a QuickChange II XL Site-directed mutagenesis kit (Invitrogen). One construct was engineered for labeling with MTSSL, containing a single Cys substitution at position 492 on the C-terminal end of the relay helix. One additional construct presented in SI was engineered with a single Cys substitution at position 639. Additionally, three constructs were engineered for labeling with BSL, each containing a di-Cys motif wherein residues on successive turns of an α-helix (positions *i* and *i*+4) were mutated to Cys. Helices targeted for mutagenesis in the three constructs were helix K in

the Upper 50kDa domain (positions 325 and 329), helix W in the Lower 50kDa domain (positions 639 and 643), and the C-terminal end of the relay helix (positions 492 and 496). Following mutagenesis, constructs were expressed and purified from *Dictyostelium* orf+ cells. F-actin was prepared from rabbit skeletal muscle as described previously [128, 129]. Actin-activated ATPase activity of myosin constructs, labeled and unlabeled, was measured using an NADH-coupled assay [130].

Skinned rabbit psoas muscle fiber bundles, dissected and permeabilized as described previously [127], were further dissected down to a diameter of 0.5mm and a length of approximately 3cm, drawn inside a 25mL glass capillary (Drummond), and secured at both ends with silk thread.

4.6.2 Site-directed spin labeling of myosin.

Single-Cys or di-Cys myosin mutants in labeling buffer (30mM Tris, 50mM KCl, 3mM $MgCl_2$, pH 7.5) were incubated at 4°C with 5mM DTT for 1hr to ensure reduction of engineered cysteine residues prior to labeling. DTT was removed using Zeba Spin desalting columns (Thermo Scientific), and myosin was incubated at 4°C for 1hr in 2-fold molar excess of either the bifunctional 3,4-Bis-(methanethiosulfonylmethyl)-2,2,5,5-tetramethyl-2,5-dihydro-1H-pyrrol-1-yloxy spin label (BSL), or the monofunctional 1-Oxyl-2,2,5,5-tetramethyl-3-pyrroline-3-methyl methanethiosulfonate spin label (MTSSL). Following incubation, excess spin label was removed and the protein was exchanged into EPR (rigor) buffer (40mM HEPES, 1mM EGTA, 2mM $MgCl_2$, 15mM KPr, pH 7.0) using Zeba Spin

desalting columns.

4.6.3 EPR Spectroscopy.

Spectra were recorded at X-band (9.6 GHz) using an E500 EleXsys spectrometer (Bruker Instruments). Acquisition of spectra for oriented samples was performed essentially as described previously [54, 92]. Briefly, skinned rabbit psoas muscle fiber bundles were incubated at 4°C with 80mM spin-labeled myosin for 1hr inside glass capillaries (described above), to decorate free actin filaments in the fiber bundle with spin-labeled S1dC. Spectra were acquired with the long axis of the fiber bundle capillary aligned parallel (using a modified TM110 cavity) or perpendicular (using a TE102 cavity) to the instrument's magnetic field. Samples were kept at 4°C throughout acquisition by flowing temperature-controlled nitrogen gas through a quartz dewar fixed to the bottom of the cavity (TM110) or through the cavity's anterior optical port (TE102). The fiber bundle was perfused with buffer under a constant flow of 340 μL/min, to eliminate unbound myosin and unbound spin label, and to allow for changing the biochemical environment of the bundle during the experiment. Three spectra were acquired in both cavities for each sample, in the presence of EPR (rigor) buffer, ADP buffer (40mM HEPES, 1mM EGTA, 2mM $MgCl_2$, 5mM MgADP, pH 7.0), and EDTA buffer (40mM HEPES, 1mM EGTA, 2mM $MgCl_2$, 10mM EDTA, pH 7.0). Following acquisition of spectra from an oriented fiber sample, the spectrum from randomly oriented fibers was recorded after removing the fiber bundle from its capillary, mincing it, and placing it in a TE102-compatible flat cell.

BSL spectra from oriented fibers were analyzed to determine the orientational distribution of the applied magnetic field in BSL's nitroxide coordinate frame, using computational simulation and least-squares minimization as described previously [103, 112]. Briefly, minced fiber spectra were analyzed to determine the orientation-independent parameters (g and A tensors). These parameters were then fixed and applied to a simulation model that assumes a sum of Gaussian distributions of static (no nanosecond rotational diffusion) spin label orientations, each defined by a center (θ_0, ϕ_0) and a width ($\Delta\theta, \phi$, full width at half maximum). This static model is justified by previous observations of BSL attached to myosin [54, 92, 93] and other proteins [94], and by the spectra of randomly oriented samples of actin-bound myosin (Fig. 2).

EPR on S1dC in solution (for spin counts) was carried out using 80mM spin-labeled protein in EPR buffer. Quartz capillaries containing S1dC (0.6mm i.d., 20mL sample volume) were sealed with critoseal and placed in an SHQ cavity (ER4122 ST). Samples were kept at 4°C throughout acquisition using a quartz dewar as described above. Quantification of the extent of spin labeling (spin labels bound per S1) was carried out as previously described [92].

Detailed plots of spectra from oriented fibers, their simulated best fits, and corresponding residuals are shown in Fig. 4.8. EPR is subject to some intrinsic ambiguity in the determination of angular centers, since the orientation dependence in EPR depends on squared cosines of angles. For simplicity, a single distribution on the interval [0,90] is reported here for each parameter. In all cases in this study, only one plausible helix orientation was found.

For each construct, we observed two well-resolved spectral components, corresponding to a major, highly ordered spin label population, and a minor, more weakly ordered population. We hypothesize that the second component arises predominantly either from unbound S1dC trapped in the myofilament lattice during fiber decoration, or (in the case of the site on Helix W, where the minor component is relatively well-ordered) from a small population of alternate BSL conformers stabilized by the structural environment of the specific labeling site. Thus, in the main manuscript, only the primary component is considered.

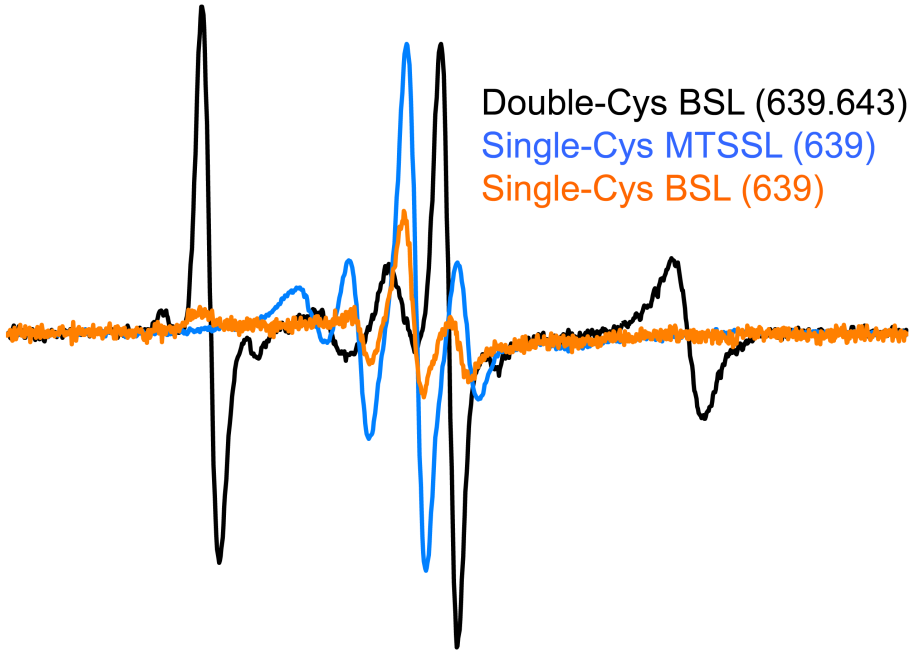

Figure 4.7. Comparison of BSL spectra from single-Cys and di-Cys constructs. Spectra were acquired on parallel-oriented fiber bundles in the absence of nucleotide. Black: Spectrum of BSL attached to a di-Cys S1dC construct at positions 639 and 643 (Helix W). Blue: Spectrum of MTSSL attached to a single-Cys S1dC construct at position 639 (Helix W). Orange: Spectrum of BSL attached to same construct as in blue. Absence of blue or orange spectral components from the black spectrum indicates complete bifunctional labeling on the di-Cys construct.

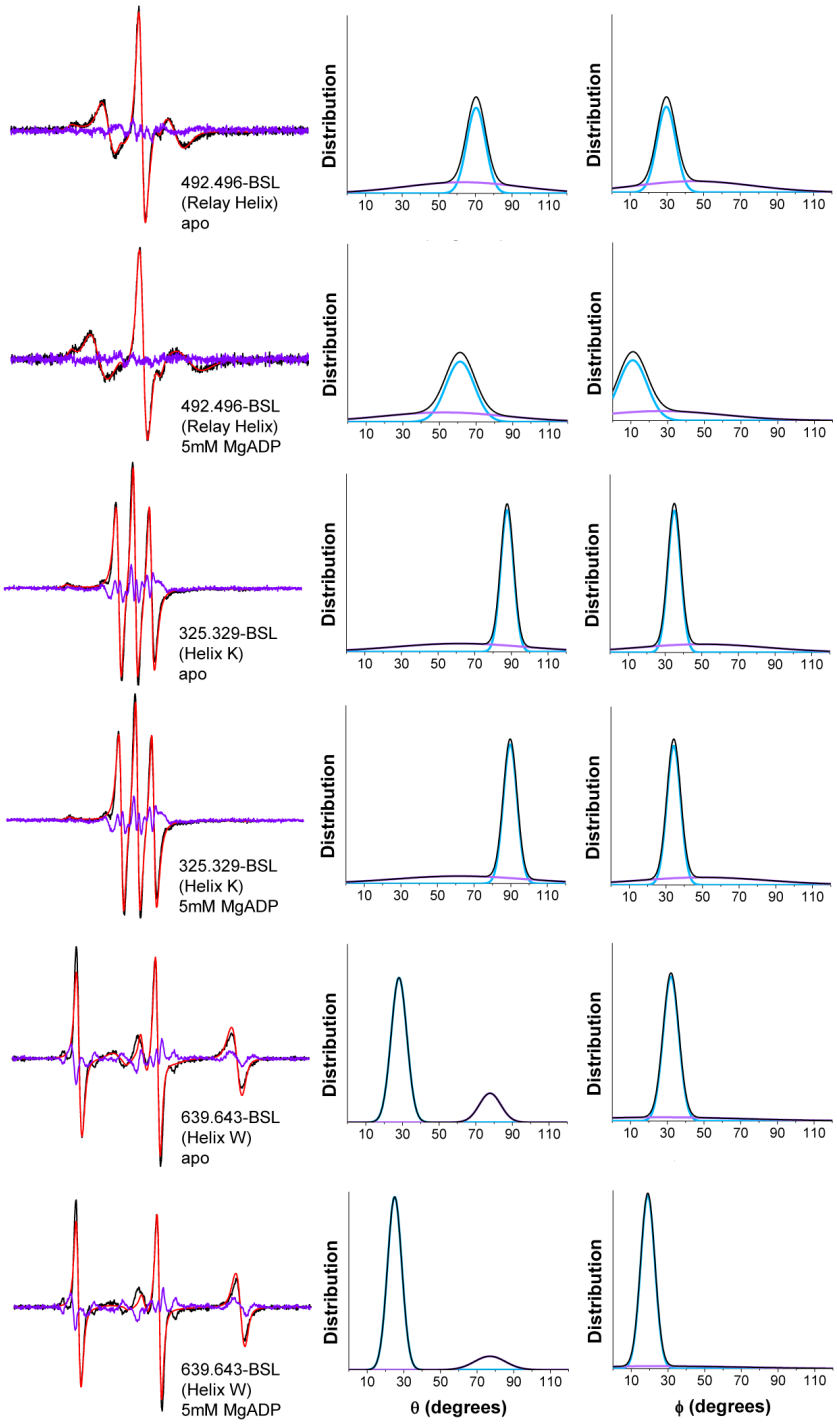

Figure 4.8. EPR spectra of fibers oriented parallel to the applied magnetic field. Left: Data (black), best fit simulated spectrum (red) and residual (purple). Center, Right: Angular distributions associated with each simulated spectrum, showing angular component 1 (cyan), angular component 2 (violet), and envelope (black).

4.6.4 Molecular modeling.

Atomic coordinates of Dicty myosin bound to rabbit skeletal actin was derived from previously published cryo-EM data by Dr. Kenneth Holmes [114]. The atomic coordinates for BSL bound to an α-helix were obtained from PDB 3L2X [94]. Angle calculations from atomic structures were calculated using custom extensions written for Visual Molecular Dynamics 1.9 (VMD) [131]. Structure images were rendered using the PyMOL Molecular Graphics System, Version 1.3 (Schrdinger, LLC) and Blender, Version 2.72b (Blender Foundation).

CHAPTER 5: HIGH-RESOLUTION MODELS OF ACTIN-BOUND MYOSIN FROM ORIENTATION AND DISTANCE MEASUREMENTS USING EPR OF A BIFUNCTIONAL SPIN LABEL

Benjamin P. Binder, Andrew Thompson, and David D. Thomas

Department of Biochemistry, Molecular Biology and Biophysics, University of Minnesota, Minneapolis, MN 55455

To be submitted to *Biophysical Journal*, 2016

5.1 Chapter Summary

We have employed two complementary electron paramagnetic resonance (EPR) techniques along with a bifunctional spin label (BSL) to directly model the effects of nucleotide binding on the structure of myosin's catalytic domain (CD), while myosin is in complex with actin. Constraints for the orientation of individual helices in the CD were obtained by acquiring continuous-wave EPR (CW-EPR) on recombinant myosin labeled at specific sites with BSL and bound to actin in skinned muscle fibers. Inter-helix distance constraints were also obtained, via analysis of Double Electron-Electron Resonance (DEER) on myosin constructs labeled specifically at two sites. We have shown previously that BSL-enabled orientation measurements alone can quantify small but significant movements of individual myosin helices, and here the addition of high-resolution distance constraints alleviates the remaining spatial ambiguity, allowing for direct refinement of existing atomic models. DEER measurements were also used to probe conformational changes in the CD upon actin binding, and to compare the effects of nucleotide binding with and without actin.

5.2 Introduction

Actin and myosin share a fundamental partnership within motile organisms, taking on a particularly specialized role in the function of striated muscle tissue. Myosin couples actin-activated hydrolysis of ATP, actin binding and release, and structural changes within its own catalytic domain to produce mechanical force on actin filaments. Upon activation of muscle contraction, this biochemical and structural coupling induces relative sliding of thin and thick filaments in the myofibril lattice, shortening the entire fiber [132, 133].

The greatest barrier to precise structural understanding of actomyosin function and pathology currently lies in difficulties associated with the determination of both proteins in complex. No crystal structures of actin-bound myosin have yet been reported, and thus the resolution of atomic models is currently limited to that of electron microscopy. Moreover, both techniques are intrinsically limited to the study of virtually homogenous samples in restricted spatial environments, imposing conditions which may not accurately reflect the dynamic structural equilibrium at play during myosin's catalytic cycle. Further refinement of existing mechanistic models thus depends on the derivation of high-resolution structural constraints using alternative methods.

Site-directed spectroscopy provides the versatility and resolution necessary for quantifying small allosteric changes within dynamic proteins. Fluorescence and electron paramagnetic resonance (EPR) in particular have been used extensively to characterize biochemical, kinetic, and structural changes in myosin [54, 56, 102, 134]. The comparatively

superior intrinsic resolution of EPR has proven especially powerful in the study of intra-myosin distances by double electron-electron resonance (DEER) [45, 56], and of the localized topology of myosin domains within oriented muscle fibers [103, 104]. Until recently, however, the effective resolving power of site-directed EPR has been limited by nanosecond mobility of the spectroscopic probe relative to its associated labeling site, contributing significant static and dynamic disorder to the resulting spectrum [84, 135].

The recent adoption of bifunctional spin labels (BSL) for site-directed labeling has shown great promise for eliminating the effect of local probe dynamics on EPR spectra [91, 136] (Fig. 1). By engineering two cysteine labeling sites at positions *i* and *i*+4 on a stable α-helix, the resulting bifunctional reaction of BSL's twin methanethiosulfonate groups strongly anchors its paramagnetic center to the protein backbone, ensuring that the spectrum will reflect only the behavior of the backbone [94]. We have recently employed this approach in oriented muscle fibers to derive the orientations of individual myosin α-helices relative to the actin filament axis [137]. The BSL approach has also been used to great advantage over traditional spin labels in the accurate determination of DEER distance distributions for multiple protein systems, both experimentally [94, 97] and *in silico* [95].

Taken together, these high-resolution orientation and distance measurements represent a set of orthogonal structural constraints similar to those often employed in nuclear magnetic resonance for structure determination [125]. Both measurements are applicable to myosin in the presence of actin, and can be performed under a wide variety of biochemical conditions. Considered alone, neither measurement is capable of directly producing

a unique atomic model for elements of the complex, but simultaneous analysis of both orientation and distance constraints has not yet been attempted. In the present work, we hypothesize that the combined use of BSL in oriented fiber EPR and in DEER will significantly alleviate spatial degeneracy, and render sufficient structural information for the development of precise atomic models of actomyosin structural elements.

5.3 Methods

5.3.1 Protein and muscle fiber preparations.

Mutant myosin constructs were prepared in a "Cys-lite S1dC" *Dictyostelium* myosin II background truncated at residue 758 and containing only one native (non-reactive) cysteine at position 655 [126]. Constructs were expressed and purified from Dictyostelium orf+ cells [138]. Skinned rabbit psoas muscle fiber bundles were dissected and permeabilized as described previously [127]. F-actin was prepared from rabbit skeletal muscle, and prepared as described previously [139]. Further details concerning methodology for expression and subsequent spin-labeling of mutant myosins are given in Section 4.6.

5.3.2 EPR spectroscopy.

CW-EPR spectra referenced in this study were recorded at X-band (9.6 GHz) using an E500 EleXsys spectrometer (Bruker Instruments). All details regarding CW spectral acquisition and subsequent analysis are given in Section 4.6; please refer to this section for details on methodology. DEER spectra were recorded at Q-Band (35 GHz) on an E580 EleXsys

spectrometer (Bruker Instruments). 30μL samples of 50-80μM spin-labeled myosin containing 10% glycerol (vol/vol) were flash-frozen in a dry ice/isopropanol bath in quartz Q-Band DEER tubes; myosin samples containing actin were mixed with the appropriate amount of actin (usually 2:1 mol/mol actin:myosin) prior to freezing. All pulsed EPR experiments were performed at 65 K, using the four-pulse DEER sequence described in Section 3.4; all $\pi/2$ pulse lengths were 12ns, and all π pulse lengths (including the ELDOR pulse) were 24ns. ν_{pump} was set to match the position of maximum absorbance in the nitroxide resonance spectrum, and ν_{obs} was centered at a second local maximum roughly 50 MHz from ν_{obs}. Resulting waveforms were analyzed using DeerAnalysis 2016 [140], and custom functions written for MATLAB [141].

5.3.3 Molecular Modeling.

Molecular modeling was carried out using the PyMOL Molecular Graphics System, Version 1.7 [142], UCSF Chimera, Version 1.9 [143], and Visual Molecular Dynamics, Version 1.9.1 [131]. Model optimization and analytical measurements were achieved using custom extensions written for Visual Molecular Dynamics in TCL and Python, using SciPy library in particular for tasks involving least-squares minimization [144, 145]. Structure images were rendered using Blender, Version 2.72b (Blender Foundation).

5.4 Results

5.4.1 Comparison of monofunctional and bifunctional spin labels for DEER distance measurements.

Three locations on myosin's catalytic domain (CD) were chosen for bifunctional labeling in this study, at positions previously determined to give unique orientational distributions and exhibit minimal perturbation of actin-activated myosin ATPase [137]. Initially, we compared the DEER spectra of equivalent constructs labeled with monofunctional and bifunctional labels; for this comparison, we focused on measuring the distance between sites on Helix K and Helix W, because these helices appear to be relatively static in myosin-only crystal structures, and give rise to narrow orientational distributions when studied individually in oriented muscle fibers (Figure 5.1A-B) [115, 116, 137, 146].

DEER spectra of myosin containing two single-Cys motifs and labeled with MTSSL display oscillations that are significantly attenuated relative to spectra from BSL-labeled di-Cys constructs, suggesting a more disordered population in the MTSSL-labeled samples (Figure 5.1C). Waveforms from both experiments were subjected to Tikhonov fitting analysis, followed by fitting of the optimal Tikhonov distribution with a single Gaussian function to parameterize the dominant distance distribution. The MTSSL-labeled single-Cys construct gives rise to a dominant distribution centered at $d_0 = 4.66$nm, with full width at half maximum $\Delta d = 0.80$nm (Figure 5.1D, blue). Conversely, the BSL-labeled di-Cys construct gives rise to a dominant distribution centered at $d_0 = 4.52$nm, with full width at half maximum $\Delta d = 0.53$nm (Figure 5.1D, red). These results indicate nearly

identical relative placement of the two nitroxide groups in the constructs, consistent with the equivalent design of the single-Cys and di-Cys labeling sites. On the other hand, the BSL-labeled di-Cys construct has a dominant distance distribution that is narrower than its MTSSL-labeled equivalent ($\Delta\Delta d = 0.27$nm). This result is expected due to the strong immobilization of bifunctionally-attached BSL on proteins, observed previously [97, 137]. The Tikhonov distribution for the MTSSL-labeled construct is also characterized by a much larger secondary distribution in the long-distance regime; the many possible rotamer states available to MTSSL are a possible explanation for this difference.

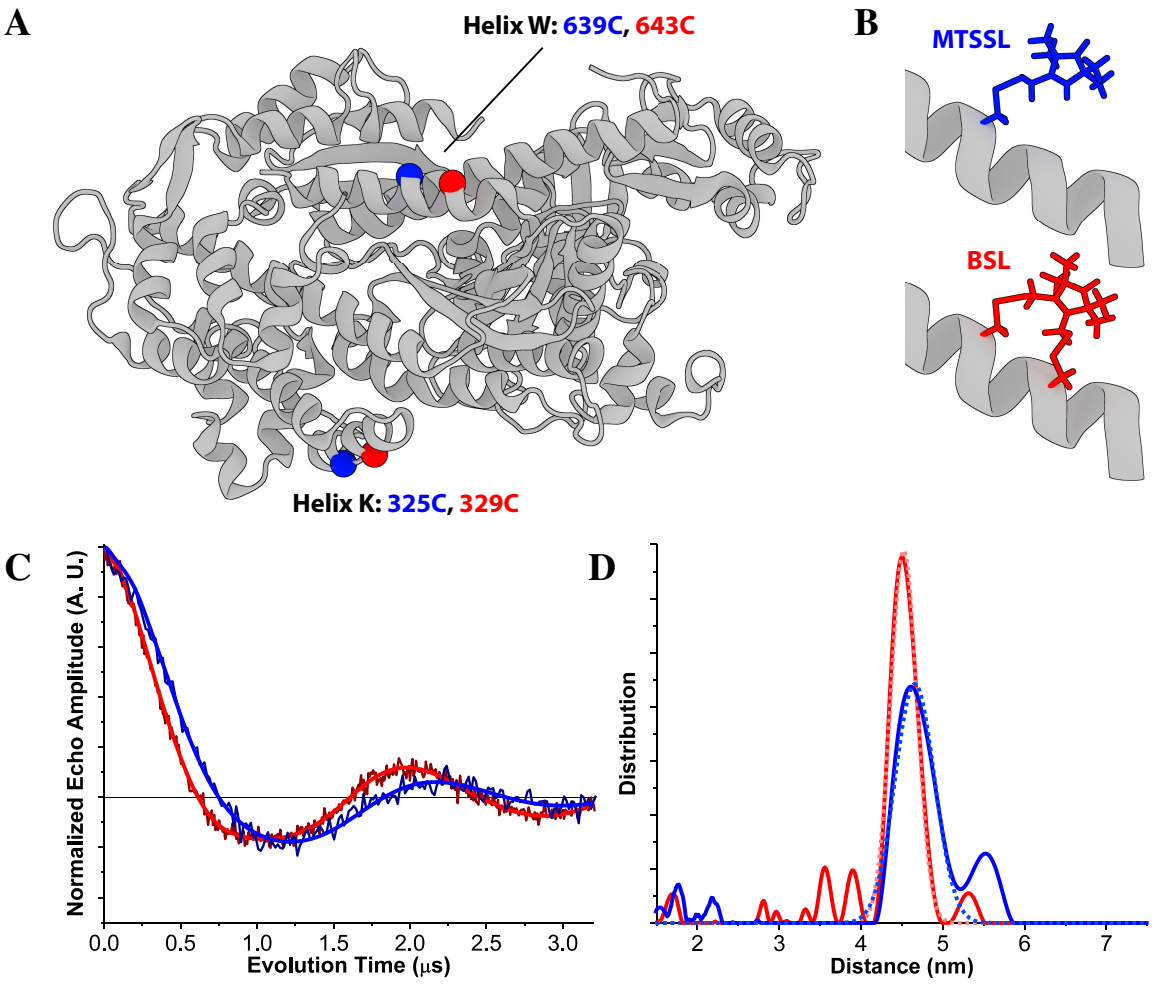

Figure 5.1. Comparison of MTSSL and BSL for distance measurements across the myosin CD. A: Structure of myosin with labeling sites highlighted. MTSSL-labeled constructs were designed by introducing cysteine residues at positions 325 (Helix K) and 639 (Helix W) (blue). BSL-labeled constructs were designed by introducing an additional cysteine residue (red) on each helix to form i and $i+4$ bifunctional labeling sites at positions 325.329 and 639.643. B: Illustration of binding modes for MTSSL and BSL. C: Background-corrected DEER waveforms for 325.639-MTSSL (dark blue) and 325.329.639.643-BSL (dark red), with spectral simulations based on best-fit Tikhonov analysis overlaid (blue and red). Spectra are shown normalized to modulation depth (horizontal line). D: Best-fit Tikhonov distance distributions for 325.639-MTSSL (blue) and 325.329.639.643-BSL (red) corresponding to spectra in C, with Gaussian fits of the dominant population overlaid (dashed light blue and pink).

5.4.2 Distances measured across the myosin CD in the presence of actin.

We generated three myosin constructs using each possible pairing of the three BSL labeling sites selected for study, and recorded DEER on doubly-labeled samples of each construct (Figure 5.8). Of the three possible constructs, two gave results that fall within the sensitive range of distance detection by DEER: 325.329.639.643-BSL (HK-to-HW; Figure 5.2A, left), and 492.496.639.643-BSL (Relay-to-HW; Figure 5.2A, right).

Next, we recorded DEER on both the HK-to-HW and relay-to-HW constructs in the presence of F-actin, using a ratio of 2:1 actin:myosin (mol/mol), to determine intra-protein distance distributions for the actomyosin complex (Figure 5.2B, gray). Tikhonov-based fitting analysis produced distance distributions that were significantly more complex than the actin-free samples, particularly for the HK-to-HW construct (Figure 5.2C, solid black). While the relay-to-HW distribution still appears centered around a single mean distance (2.58nm), the HK-to-HW distribution is characterized by three major peaks, centered at 3.95nm, 4.69nm, and 5.52nm.

When parsing these results into relevant constraints for model building, it was necessary to determine which HK-to-HW distances actually arise from DEER between the desired intra-protein label pairs. We hypothesized that one of the peaks in the HK-to-HW distribution, centered at the far distance of 5.52nm, was an artifact arising from two labeled myosin heads binding in close proximity along actin's polymer repeat. To test this hypothesis, additional DEER experiments were performed, varying the concentration ratio

of F-actin to myosin in a titration series (Figure 5.9). The relative fraction of the total distance distribution contained in the 5.52nm peak was shown to be inversely related to the amount of F-actin present, supporting the notion that this distance arises from DEER between two nearby myosin heads. By contrast, the fractional contribution of the 3.95nm and 4.69nm peaks increases with increasing F-actin concentration, suggesting that both of these peaks correspond to intra-protein distances (Figure 5.10). Previous biophysical studies of the myosin CD have only identified a single structural population for the nucleotide-free rigor state, and our previous work with BSL at the Helix W site suggests that the local environment there may accommodate two distinct preferred conformations of BSL [56, 137]. Thus, we hypothesized that the 3.95nm and 4.69nm peaks correspond to two alternate label conformers, rather than two distinct structural states of myosin. This hypothesis required validation through modeling analysis, and is treated thoroughly in a following section. In the analysis presented here, we focus on the 4.69nm peak.

The primary peaks of each distance distribution were easily fit by Gaussian distributions (Figure 5.2C, dashed gray), and their corresponding parameters are given in Table 5.1. Table 5.1 shows that the HK-to-HW distribution is characterized by a narrow width similar to that observed in the actin-free samples (Figure 5.1). By contrast, the distribution of distances in the relay-to-HW construct is much wider, reflecting the greater conformational flexibility of the Relay Helix that has been observed previously [137].

5.4.3 Small changes in inter-helix distance distributions are detected with MgADP.

In order to assess the potential impact on actomyosin structure with nucleotide binding/release, we recorded DEER on our relay-to-HW and HK-to-HW constructs in the presence of both actin (2:1 actin:myosin, mol/mol) and 5mM MgADP (Figure 5.2B, light green). Tikhonov-based fitting analysis produced distributions that were each distinct from their nucleotide-free analogs, with a greater difference observed in the HK-to-HW construct (Figure 5.2C, solid dark green). As before, primary distribution peaks were parameterized by Gaussian fitting, and the corresponding values are given in Table 5.1.

The differences in inter-helix distances between apo and MgADP-bound states of myosin are very slight, with the relay-to-HW construct reporting no change in distribution center, and a change in width of less than 0.1nm, which, although small, is evident in the altered shape of the DEER waveform (Figure 5.2B). The HW-to-HK construct reports a widening of the primary distance distribution, with FWHM= 1.02nm, but it is difficult to determine how much of this perceived width increase truly corresponds to the desired intra-protein measurement, and how much is contributed by merging of that distribution with the long distance detected as a distinct distribution in the apo state. The center of this distribution does shift significantly, however, with a change in center $\Delta d = +0.13$nm.

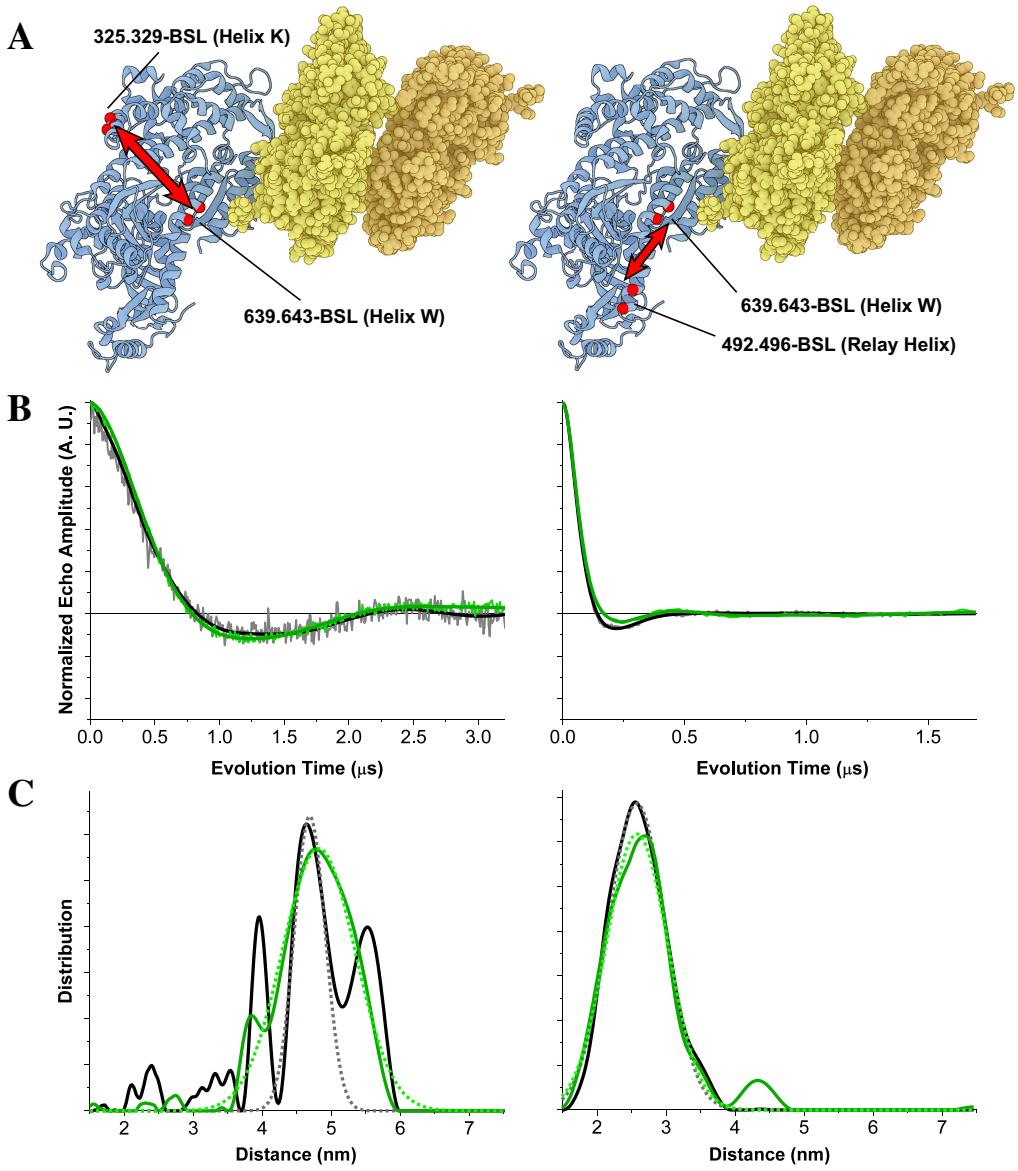

Figure 5.2. Comparison of the apo and MgADP states of the actomyosin complex, measured using two double-BSL constructs. A: Illustration of the HK-to-HW distance (left) and relay-to-HW distance (right), showing two actin monomers from different chains (yellow and orange), the myosin CD (blue) and relevant BSL labeling sites (red spheres). Actin filament axis is normal to the plane of the page. B: Background-corrected DEER waveform data from the constructs illustrated in A, in the absence of nucleotide (gray) and the presence of 5mM MgADP (light green). Best-fit Tikhonov simulations are overlaid in black and dark green, respectively. C: Derived distance distributions from the data in B. Tikhonov distributions are shown in solid black (apo) and solid dark green (MgADP), and Gaussian fits of primary peaks are shown with dashed lines.

	Apo (rigor)		5mM MgADP	
	Mean Distance (nm)	FWHM (nm)	Mean Distance (nm)	FWHM (nm)
492.496.639.643-BSL	2.58	1.39	2.58	1.48
325.329.639.643-BSL	4.69	0.75	4.82	1.77

Table 5.1. Gaussian parameters for primary distance distributions in actin-bound myosin. Values are from Gaussian fitting of best-fit Tikhonov distributions derived from DEER, isolating the primary distribution peak (Figure 5.2C, dashed lines).

5.4.4 An atomic model of the apo complex satisfies experimental constraints from orientation and distance, and characterizes BSL's binding conformation.

Molecular modeling was employed to compare our EPR-based measurements of inter-helix distance, as well as previous data reporting on individual helix orientations [137], with established atomistic models. Our goal was to produce a model for the spin-labeled actomyosin complex, validated both by the literature and our experiments, which could subsequently be used as a template for exploring the structural topology of states for which no atomic structure is currently available: namely, the MgADP-bound rigor state.

In order to directly correlate spectroscopically-derived results with protein structure, our first consideration was the choice of initial reference model for actomyosin. A recent cryo-EM model of human cytoplasmic myosin-IIc bound to actin was chosen for use as a template (PDB ID: 5JLH), due to the extremely high resolution of the map compared to previous models using myosin-II, and the excellent structural alignment of the derived co-ordinates with those previous models (Figure 5.11A) [61, 69, 114]. In order to examine this topology in the context of our *Dictyostelium* myosin constructs, we generated a homology

model of the *Dictyostelium* sequence using the 5JLH myosin structure as a template (Figure 5.11B) [147–150]. This homology model was subsequently combined with the F-actin structure from 5JLH by successive structural alignments, yielding a final model consisting of two myosin CD's bound to adjacent monomers in the same actin polymer chain. In this way, we obtained an actomyosin model capable of representing both distances within an actin-bound myosin CD, and distances between neighboring CD's on an actin filament. As discussed above, both types of distances are expected to contribute in our DEER-derived distributions.

The second major consideration was the choice of initial starting model for BSL. Only one crystal structure of BSL attached to positions i and $i+4$ on an α-helix has currently been reported, using T4 lysozyme as the labeling target (PDB ID: 3L2X) [94]. Thus, while the underlying tertiary structure we used for the nucleotide-free actomyosin complex has been supported by near-identical alignments across several isoforms in independent studies [45, 61, 114, 151], the conformation of BSL reported by crystallography is less substantiated. Our previous work has strongly suggested that BSL tends to adopt a single, primary, stereospecific conformation on straight α-helices, but that this conformation is not truly represented in the lysozyme crystal structure, due to the placement of labeling sites near a kink in the secondary structure [137]. Therefore, the first question we sought to answer with our model concerns optimization of spin label conformation. Specifically, we asked whether there exists a single, consistent conformation of BSL which, when modeled onto each helix in our actomyosin structure, is sufficient to generate agreement with the primary

distance and orientational distributions gathered thus far from EPR.

We began by modeling BSL onto each of the three experimentally-labeled helices at appropriate positions in both myosin molecules, by least-squares alignment of backbone atoms from the published coordinates in 3L2X [94]. In order to perform a robust conformational search, it was necessary to ensure that the initial conformations at each labeling position were truly equivalent; therefore, each label was parameterized relative to its associated myosin helix. Five parameters were considered: θ_{NH} and ϕ_{NH}, the polar angles of the myosin helix axis in the label nitroxide frame; $\vec{v}_{\text{core}}$, the perpendicular vector from the nitroxide nitrogen to the center of the helix; $\vec{v}_{\text{axis}}$, describing the parallel displacement along the helix axis from a zero position defined by the α-carbons of the labeled cysteines; and ψ, the angle of rotation of the nitroxide nitrogen about the helix axis (Figure 5.3). Simultaneous consideration of all five parameters provides a unique description of the spatial relationship between a label and its associated helix. To enforce consistency in the model, we chose one label position to act as a template (arbitrarily, on Helix K), and examined the difference between that label's conformational parameter set, and the parameter sets of each of the other five labels. These differences were minimized by least-squares optimization of a geometric transformation acting on the position and orientation of the spin label coordinates, according to the function

$$T(\{c\}) = \Omega_{\text{N}}(\alpha_N, \beta_N, \gamma_N) + (u\hat{x} + v\hat{y} + w\hat{z}) \tag{5.1}$$

where $\{c\}$ is a set of atomic coordinates, $\{u, v, w\}$ are scalar coefficients; $\{\hat{x}, \hat{y}, \hat{z}\}$ are unit

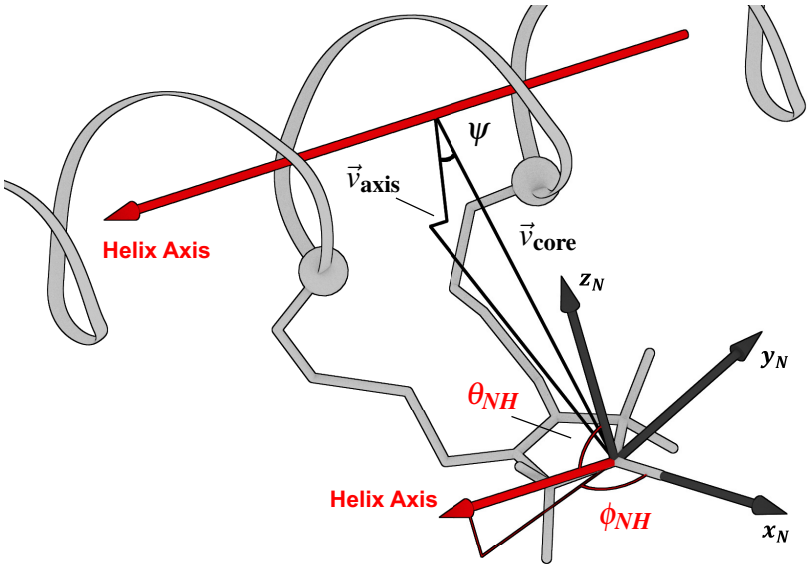

Figure 5.3. Illustration of conformational parameters. Angles θ_{NH} and ϕ_{NH} are the polar angles of the helix axis (red) in the nitroxide frame (dark gray). Vectors $\vec{v}_{\text{core}}$ and $\vec{v}_{\text{axis}}$ are measured relative to the geometric center of the helix. The angle ψ is a function of label rotation relative to α-carbon position.

vectors corresponding to principle axes of the global coordinate system; and Ω_{N} is a geometric transformation defined in the label nitroxide frame, defining a rotation described by Euler angles α_N, β_N, and γ_N. Optimized functions were applied to the coordinates of each label in turn, thereby generating a consistent starting model for our conformational search.

Eight constraints from the nucleotide-free EPR experiments were imposed on the model: three sets of θ_{NA} and ϕ_{NA}, the polar angles of the actin filament axis in the nitroxide frame for each labeling site; $d_{\text{K-W}}$, the 4.69nm distance derived from DEER on the HK-to-HW construct; and $d_{\text{relay-W}}$, the 2.58nm distance derived from DEER on the relay-to-HW construct (Table 5.2). The corresponding distance and orientation measurements were calculated in our model, and optimized by applying the following transformation function to

each label's coordinates simultaneously:

$$T(\{c\}) = \Omega_{\mathrm{N}}(\alpha_N, \beta_N, \gamma_N)\Omega_{\mathrm{R}}(\psi) + a\vec{v}_{\mathrm{axis}} + b\vec{v}_{\mathrm{core}} \tag{5.2}$$

where $\{c\}$ is a set of atomic coordinates; Ω_{N}, $\vec{v}_{\mathrm{core}}$, and $\vec{v}_{\mathrm{helix}}$ are defined exactly as described above; $\{a,b\}$ are scalar coefficients; and Ω_{R} is a geometric transformation applying a rotation of ψ degrees about the helix axis. Least-squares optimization of the model against all eight experimental constraints corresponds to minimizing the function

$$\begin{aligned} f(\alpha_N, \beta_N, \gamma_N, \psi, a, b) = &\sum_{\{c_n\}} \left(\Theta\left(T(\{c_n\})\right) - \theta_n\right)^2 \\ &+ \sum_{\{c_n\}} \left(\Phi\left(T(\{c_n\})\right) - \phi_n\right)^2 \\ &+ \left(D\left(T(\{c_{\mathrm{K}}\}), T(\{c_{\mathrm{W}}\})\right) - d_{\text{K-W}}\right)^2 \\ &+ \left(D\left(T(\{c_{\text{relay}}\}), T(\{c_{\mathrm{W}}\})\right) - d_{\text{relay-W}}\right)^2 \end{aligned} \tag{5.3}$$

where $\{c_n\}$ is a set of atomic coordinates corresponding to a spin label at location n; θ_i and ϕ_i are experimental θ_{NA} and ϕ_{NA} values for index i; and Θ, Φ, and D are functions for calculating θ_{NA}, ϕ_{NA}, and interspin distances, respectively. A minimum was found with the following parameters: $\alpha_N = -116.6°$, $\beta_N = -12.6°$, $\gamma_N = 129.9°$, $\psi = -7.7°$, $a = -0.4$Å, and $b = -1.6$Å; the optimal transformation T was subsequently applied to the coordinates of each BSL molecule.

A comparison between experimental constraints and equivalent measurements in our

		Experiment	Model	Difference
Actin-BSL Axial Angle, θ_{NA} (°)	Helix K	88.2	87.1	1.1
	Relay Helix	109.5	110.2	0.7
	Helix W	152.0	152.1	0.1
Actin-BSL Azimuthal Angle, ϕ_{NA} (°)	Helix K	33.3	32.6	0.7
	Relay Helix	-27.0	-28.5	1.5
	Helix W	147.4	148.6	1.2
Intra-Helix Distances (nm)	HK-to-HW	4.69	4.50	0.19
	Relay-to-HW	2.58	2.57	0.01

Table 5.2. Comparison of EPR experimental constraints for the apo actomyosin complex with measurements derived from the optimized model. Experimental orientation values reported here are exactly equivalent to the mean orientational distribution values given in Table 4.1 for the apo experiments, with symmetric reflections applied to some values to account for the intrinsic degeneracy in EPR's sensitivity to θ_{NA} (twofold) and ϕ_{NA} (fourfold).

optimized model is given in Table 5.2, and the pre- and post-optimization label conformations are overlaid in Figure 5.4A. It is striking to observe that a relatively small adjustment to the crystal conformation is sufficient to bring all measured parameters to within 1.5°, and 0.2nm, of experimentally-determined values. In addition to the values reported in Table 5.2, we also surveyed interspin distances between neighboring myosin molecules, and determined that all possible interactions are in the very long distance regime, beyond 5.5nm (Figure 5.12). This further supports the hypothesis that the long-distance peak observed in our HK-to-HW construct is a nearest-neighbor artifact, and shows that this solution does not give rise to any conflicting distances that are absent in our experimental analysis. Thus, a single, consistent label conformation employed within our cryo-EM-based actomyosin model is indeed sufficient to reproduce all primary, experimentally-determined parameters

with high precision.

Next, we turned to the minor sub-populations left unaccounted for in our single-conformation hypothesis, comprising the minor 3.95nm distance observed with the HK-to-HW construct, and a pair of θ_{NA} and ϕ_{NA} values from a secondary sub-population in the oriented fiber analysis for Helix W [137]. Because Helix W was the only labeling location with two distinct, well-ordered spectral components in oriented fibers, we initially expanded our analysis to allow for two label conformations on Helix W only. To determine the most likely starting point for optimization of the alternate conformer, we re-examined the crystal structure of BSL on T4 lysozyme used in the previous hypothesis [94]. The published coordinates for this structure report a single conformation of the spin label, but examination of the associated electron density map reveals significant patches of unfitted density that likely correspond to a minor secondary conformation (Figure 5.13). A coarse atomic model of this minor conformation was generated by rigid-body fitting of BSL coordinates into the unfitted density from 3L2X (Figure 5.13) [152], and subsequently modeled onto Helix W in our optimized model by the same least-squares alignment described above. A variation on the algorithm in Equation 5.3 was performed, this time allowing only the alternate conformation to move while the labels from the optimized model at all other locations remained fixed. For experimentally-derived constants θ_i, ϕ_i, and d_i, values corresponding to secondary sub-populations were supplied in place of their primary counterparts. Once again, agreement with all constraints was found with minimal adjustment of the starting conformation (Figure 5.12, Table 5.5). Combined with the analysis detailed

above, this result serves to account for all populations observed in EPR.

Before employing our spin-labeled apo model in the determination of novel structural states, it was necessary to ascertain whether the optimized label conformations obtained above were sterically viable. Thus, energy minimization was performed to optimize model geometries surrounding each spin label. The five-membered ring and primary ring substituents of each BSL molecule were fixed in place during the minimization, in order to preserve experimentally-constrained positions and orientations; actin monomers were also fixed in place, while all disulfide linkages, backbone atoms, and side chains in myosin were allowed to relax until convergence. Pre- and post-minimization models are overlaid in Figure 5.4B, demonstrating that the label conformations imposed by our optimization have a minimal effect on protein structure.

Thus, the cryo-EM-based model we used to represent the nucleotide-free rigor complex is validated by our experimental and modeling results. Furthermore, our hypothesis regarding the highly stereoselective nature of BSL labeling is strongly supported by agreement between our labeled model and experimental results obtained using two different EPR techniques across multiple labeling sites.

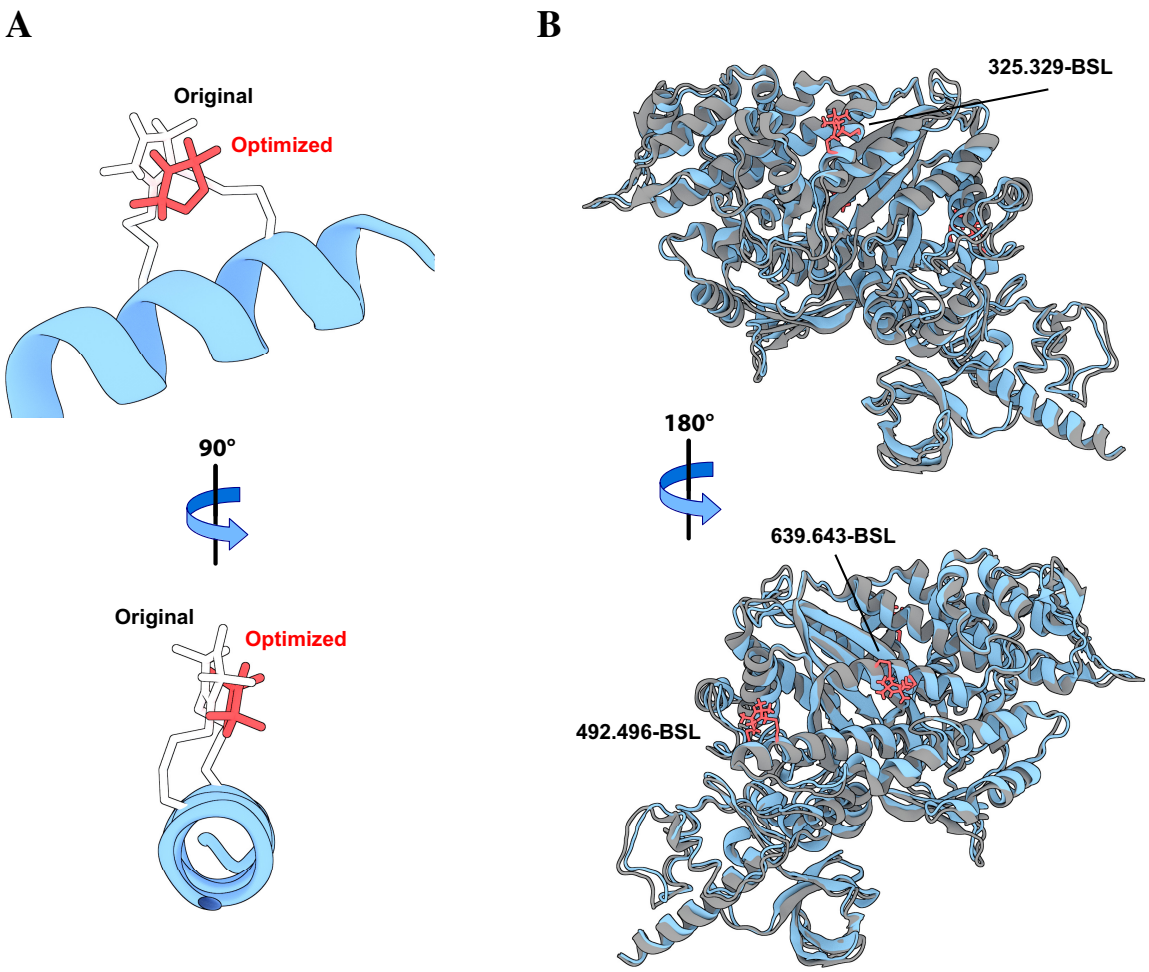

Figure 5.4. Optimization of spin labels and protein structure in the apo state. A: Conformation of BSL applied in our actomyosin model, before (white) and after (red) minimization against experimentally-derived constraints. B: Spin-labeled myosin structure used in our actomyosin model, before (blue) and after (dark gray) energy minimization. Spin labels at all sites (red) were fixed in place, forcing local protein structure to relax around them.

5.4.5 The structure of the MgADP-bound rigor complex is determined by application of experimental constraints.

Having validated our structure of spin-labeled actomyosin in the apo state, we applied additional orientation and distance constraints to determine how this structure changes in the presence of saturating MgADP. Our approach was similar to the BSL conformer optimization method described above; this time, however, adjustments to labeled helices were allowed while spin label conformation was held fixed.

Several studies have provided strong evidence for a structural transition coupled to ADP release in the actomyosin rigor complex, and myosin-only crystal structures also report subtle differences in protein conformation. However, the sensitivity of these techniques has been largely limited to changes in the force-generating region of S1: the only significant differences observed in crystals occur at the interface between the L50 and Converter domains, and while force-sensing and motility studies reveal lever arm movement in several myosin isoforms, changes internal to the CD cannot be directly observed by these methods. Thus, our constrained modeling approach was designed to allow all three labeled helices full freedom of movement, comprising 3 translational modes and 3 rotational modes. Helices K and W are straight α-helices in all reported crystal structures, with negligible movement relative to surrounding tertiary structure across various biochemical conditions; therefore, these helices were assumed to behave like rigid rods, with rotational pivot points placed at their centers of geometry. The relay helix, on the other hand, has been observed in crystals to exhibit a kink at residue 486, which is strongly coupled to bound nucleotide; thus, only the C-terminal region of the helix (comprising residues 486-496) was allowed to

move, with a rotational pivot point centered at residue 486.

Once again, eight constraints were applied in our structural refinement: namely, the same set of six angles and two distances employed in the previous section. This time, however, the values of these constraints were derived from experiments performed in the presence of 5mM MgADP (Table 5.1, Table 5.3), and the starting model for refinement was the final, optimized model of the apo state derived in the previous section. Choice of this model for the initial condition necessarily biases our refinement toward the solution which most closely resembles the apo complex, but this inherent assumption is justified by the subtlety of the internal changes expected. During optimization, all atoms in each helical segment (including attached spin labels) were subjected to the transformation

$$T(c) = \Omega_{\mathrm{H}}(\alpha_H, \beta_H, \gamma_H) + (u\hat{x} + v\hat{y} + w\hat{z}) \tag{5.4}$$

where c is a set of atomic coordinates, $\{u, v, w\}$ are scalar coefficients; $\{\hat{x}, \hat{y}, \hat{z}\}$ are unit vectors corresponding to principle axes of the global coordinate system; and Ω_{H} defines a rotation described by α_H, β_H, and γ_H, which are the yaw, pitch, and roll angles associated with each helix in the global coordinate frame, respectively. The optimal transformation was found by least-squares minimization of Equation 5.3, using Equation 5.4's definition of T and experimentally-derived constraints corresponding to MgADP experiments, rather than those in the absence of nucleotide. Unlike the spin label optimization in the previous section, which enforced equivalent transformations across all labeling sites, here each

		Experiment	Model	Difference
Actin-BSL Axial Angle, θ_{NA} (°)	Helix K	89.2	89.8	0.6
	Relay Helix	119.1	119.1	0.0
	Helix W	155.0	155.0	0.0
Actin-BSL Azimuthal Angle, ϕ_{NA} (°)	Helix K	35.3	37.0	1.7
	Relay Helix	-13.6	-13.3	0.3
	Helix W	157.4	157.7	0.3
Intra-Helix Distances (nm)	HK-to-HW	4.82	4.83	0.01
	Relay-to-HW	2.58	2.58	0.08

Table 5.3. Comparison of EPR experimental constraints for the MgADP-bound actomyosin complex with measurements derived from the optimized model. Experimental orientation values reported here are exactly equivalent to the mean orientational distribution values given in Table 4.1 for the 5mM MgADP experiments, with symmetric reflections applied to some values to account for the intrinsic degeneracy in EPR's sensitivity to θ_{NA} (twofold) and ϕ_{NA} (fourfold).

helical segment was allowed to move independently, resulting in a unique set of 6 transformation parameters for each of the three helices considered.

Optimal parameters from the minimization are given in Table 5.6. Pre- and post-MgADP-minimization models are overlaid in Figure 5.5A-C, and a comparison of experimental measurements to those calculated from the post-minimization model is given in Table 5.3. Strikingly, these results show that without influence from any existing structures of the MgADP state, the relay helix in our model converges to a conformation which agrees remarkably well with myosin-only crystal structures (Figure 5.5D). Results from our previous study also support this notion of structural similarity between actin-free and actin-bound states of the relay helix [137], but here the additional distance constraints from

DEER make it possible to arrive at this conclusion completely independently. Furthermore, it is now possible to precisely probe additional changes that were previously observed with orientation measurements alone: Helix W (and, to a much lesser extent, Helix K) are altered by the presence of MgADP (Figure 5.5D). While Helix K remains almost entirely static and retains excellent alignment with myosin-only crystal structures, Helix W experiences a significant shift relative to the center of the actin-binding cleft, with residues closer to the actomyosin interface angling away (Figure 5.5A-B). When both helices and the cleft axis are all observed in the same plane (Figure 5.5B), Helices K and W experience subtle movement away from one another across the cleft axis. If the movement of Helices K and W is assumed to represent bulk movement of the Upper 50kDa and Lower 50kDa domains respectively, then this change represents a subtle opening of the actin-binding cleft upon MgADP binding. To our knowledge, this is the first quantified report of a MgADP-induced effect on the structural state of the cleft.

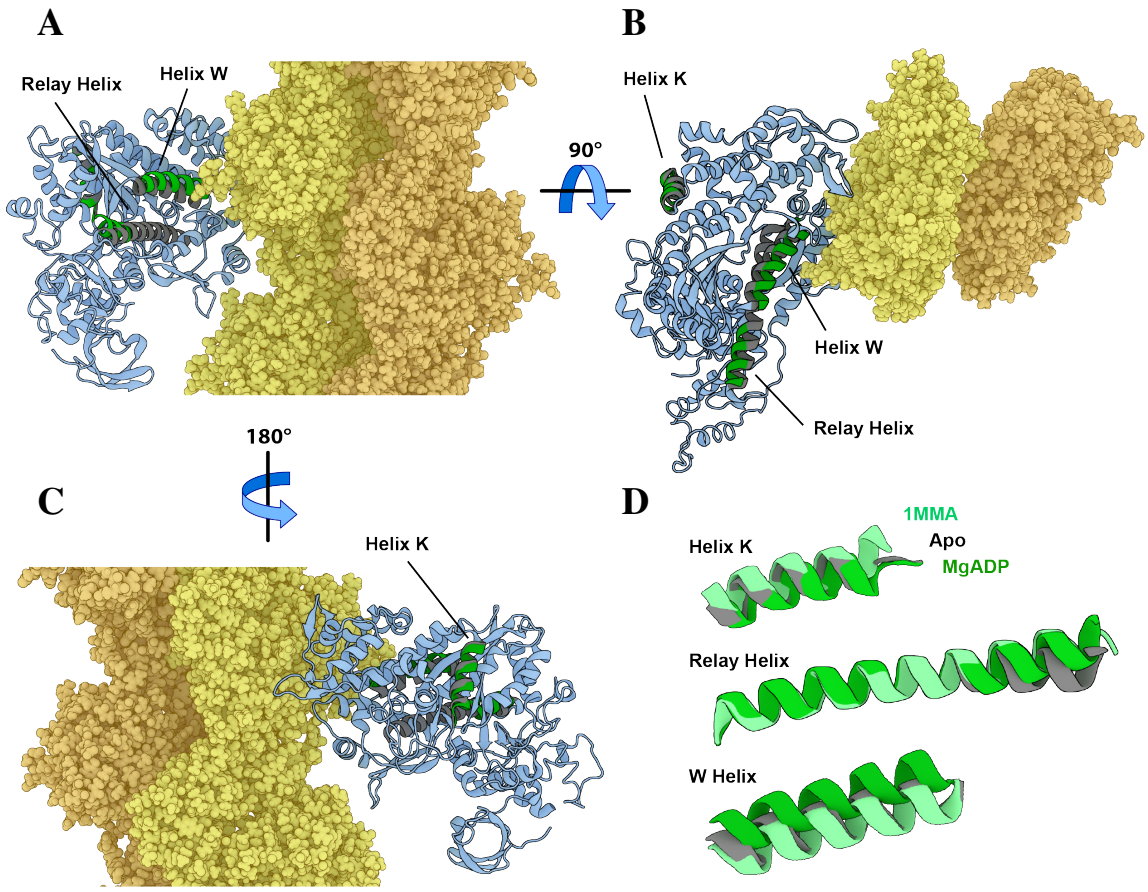

Figure 5.5. Refinement of the MgADP-bound state of actomyosin. A-C: Myosin (blue) and actin (yellow/orange) from our model of the rigor complex, before and after MgADP refinement. Targeted helices (K, relay, and W) are highlighted in the pre-refinement (apo state, dark gray) and post-refinement (MgADP state, green) states. D: Comparison of the apo state (dark gray) and MgADP state (green) models to a crystal structure of *Dictyostelium* myosin without actin, bound to MgADP (PDB ID: 1MMA, light green) [19]. Because of significant differences in the overall arrangement of domains around the actin-binding cleft between crystal (cleft open) and model (cleft closed) structures, alignment of the crystal structure to the model was accomplished via pair-wise matching of either the Upper 50kDa domain (for Helix K) or the Lower 50kDa domain (for the Relay Helix and Helix W).

5.4.6 Comparison of actin-free and actin-bound DEER distances reveal structural changes across the myosin cleft.

In addition to the changes induced by MgADP binding and/or release, the information obtained in our DEER experiments enables an analysis of the effects of actin binding on the myosin CD. While the lack of known helix orientation constraints for an actin-free myosin prevents the same detailed structural modeling approach taken above, a comparison of distances with and without actin remains informative. DEER spectra from spin-labeled samples of the HK-to-HW and relay-to-HW constructs, prepared in the presence and absence of 2:1 actin:myosin (mol/mol), are shown overlaid in Figure 5.6. The primary Tikhonov peaks in each dataset were fit to single Gaussian distributions, and their associated parameters are given in Table 5.4. Gaussian analysis reveals a very subtle change in mean distance for the HK-to-HW construct, corresponding to a positive shift of $+0.17$nm upon addition of actin. In contrast, the relay-to-HW construct shows negligible change in mean distance, with $\Delta d < 0.05$nm. Both constructs exhibit a significant increase in disorder for their primary sub-population, with $\Delta\Delta d = +0.64$nm for the HK-to-HW construct, and $\Delta\Delta d = +0.22$nm for the relay-to-HW construct.

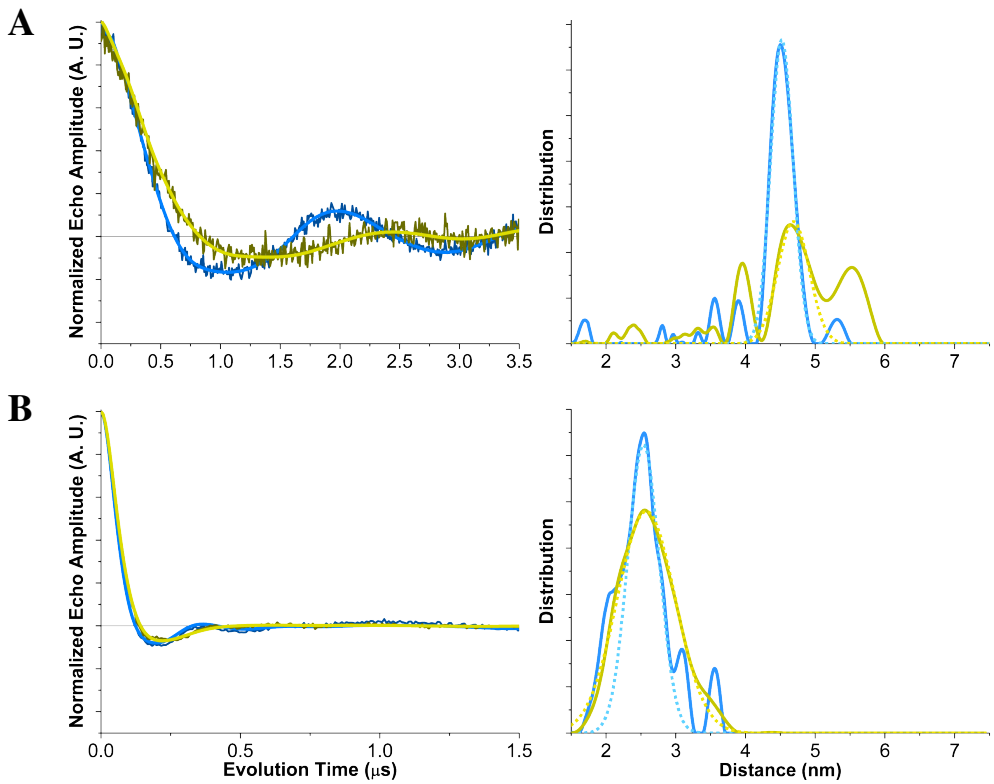

Figure 5.6. Comparison of intra-myosin distances measured by DEER in the presence and absence of actin. Left: Background-corrected DEER waveforms for the HK-to-HW construct (A) and the relay-to-HW construct (B), comparing data from a sample of spin-labeled myosin alone (dark blue) with data from a sample containing 2:1 actin:myosin (mol/mol) (dark yellow). Best-fit Tikhonov simulations are overlaid in blue and yellow, respectively. Right: Derived distance distributions from the data at left. Tikhonov distributions are shown in solid blue (myosin alone) and solid yellow (with actin), and Gaussian fits of primary peaks are shown with dashed lines.

	Myosin Alone		2:1 Actin:Myosin (mol/mol)	
	Mean Distance (nm)	FWHM (nm)	Mean Distance (nm)	FWHM (nm)
492.496.639.643-BSL	2.54	0.75	2.58	1.39
325.329.639.643-BSL	4.52	0.53	4.69	0.75

Table 5.4. Gaussian parameters for primary distance distributions in the presence and absence of actin. Values are from Gaussian fitting of best-fit Tikhonov distributions derived from DEER, isolating the primary distribution peak (Figure 5.6, dashed lines).

5.5 Discussion

5.5.1 BSL adopts a highly stereoselective conformation on protein α-helices.

BSL has been employed as an attractive alternative to monofunctional spin labels in a variety of systems, but while several attempts have been made to characterize the label's binding behavior, definitive conclusions are difficult to draw [94, 95, 97, 153]. Pure *in silico* analysis tends to produce conformational distributions which are significantly wider than those observed in experiments [95, 137, 153], and the only crystal structure currently available is unlikely to reflect a preferred conformation on straight α-helices due to disadvantageous positioning of reactive cysteines in the target protein [94]. Thus, it has been very challenging to relate BSL-derived measurements of orientation and distance directly to the behavior of an associated protein backbone, despite much evidence that the label readily becomes strongly immobilized and highly ordered upon bifunctional attachment.

In the present study, we have demonstrated that the advantages of BSL for increased distance resolution in DEER still apply when employed in the large and dynamic myosin CD (Figure 5.1). By examining multiple spin label pairs across the CD, we have determined that BSL produces distance distributions of a width comparable to the width observed in orientational distributions from oriented fibers (Figure 5.2, Figure 5.8, Table 5.1) [137]. As with the analogous experiments in oriented fibers, these measurements are also sensitive to subtle structural changes induced by nucleotide binding.

Crucially, we have used this experimental data to determine a single label conformer

that is consistently preferred across three separate labeling sites on different helices. Extensive *in silico* modeling and optimization reveals that a single conformation is sufficient to satisfy all orientation and distance constraints from EPR, without significantly deforming a high-resolution cryo-EM model of actomyosin (Figure 5.4) [69, 137]. This label conformation is significantly different from the published crystal coordinates, though in comparison, the label still retains its position on the same side of the helix, and its orientation relative to the helix axis is similar [94]. We have also characterized a secondary conformation, which is sufficient to account for all significant minor sub-populations in experimental distributions (Figure 5.12). Results from our optimization indicate that this alternate conformation is likely present on just one of the three helices, and that it is similar to the conformation suggested by unfitted density in the published crystallographic data (Figure 5.13) [94].

Tight coupling of spin labels to the protein backbone was a goal that inspired the original synthesis of BSL [91], and this property has since been well-established in the literature [54, 93, 94, 97, 153]. In the present work, we expand upon a hypothesis from our previous study, demonstrating that BSL is not only strongly immobilized and well-ordered on α-helices, but also *highly stereoselective*. Our results indicate that the label takes at most two conformations on the three helices surveyed, and that one of these conformations is strongly preferred over the other. The notion of stereospecificity in site-directed spin labeling represents tremendous potential for high-resolution structure determination, because the relationship between backbone and nitroxide is unambiguous, and therefore subject to direct modeling. We have determined structures for each of the observed conformations,

and thus our findings are readily applicable to other protein systems via direct modeling.

5.5.2 The C-terminal end of myosin's relay helix rotates upon binding of MgADP.

The ADP-release step in myosin's catalytic cycle has garnered increasing attention as a source of important coupled structural changes in Subfragment-1, particularly as they pertain to force generation. Movement of the myosin lever arm at a rate comparable to the release of ADP has been observed in several isoforms [31, 32, 57, 58], as have strain-dependent effects on ADP release rate [57, 58, 121–123, 154, 155]. Crystal structures of myosin alone have long predicted a movement of the C-terminal end of the relay helix upon binding of various nucleotides, including MgADP, which are thought to correlate with large-scale transitions of the lever arm [19, 115–117, 146]. These interactions have been difficult to observe in actin-bound myosin, but examples for processive non-muscle and smooth muscle myosins are available [49, 124].

We have demonstrated previously that a structural transition also occurs in actin-bound myosin-II upon MgADP binding/release: results from EPR on oriented fibers indicated movement of the C-terminal end of the relay helix that was likely to mirror the shift observed in myosin-only crystal structures [137]. However, our conclusions were limited by the relatively small number of experimental constraints, such that we were only able to quantitatively report the change in helix tilt angle relative to the actin filament axis.

In the present study, our experimental constraints for this system have been significantly expanded with the addition of DEER-derived distance distributions. The additional

parameters have allowed us to render a complete geometric transformation for the observed changes in the relay helix, resulting in a new set of coordinates that may be compared to myosin-only crystal structures (Figure 5.5). Our final model falls in excellent agreement with these structures, indicating that the presence of actin does not significantly alter the structural mechanism of force propagation in the myosin CD.

5.5.3 The actin-binding cleft opens slightly upon binding of MgADP.

Many studies have shown that the changes to myosin structure induced by MgADP are not limited solely to the force-generating domain. The binding of MgADP in myosin's nucleotide binding pocket has been shown to drastically reduce the affinity of myosin for actin, especially for classes characterized by a low duty cycle, like myosin-II [52, 119, 120, 156, 157]. This change in affinity implies that structural transitions also occur near the actomyosin interface as a result of ADP binding/release, but no study has yet determined the extent or nature of these changes in myosin-II.

The actin-binding cleft is a large solvent-filled cavity between the Upper and Lower 50kDa domains in myosin's CD that has been widely observed to narrow (or "close") when myosin transitions from a weak-binding interaction into a strongly-bound rigor complex with actin [45, 49, 61, 69, 114, 151, 158, 159]; this correlation has led to the adoption of cleft conformation as a reporter for actomyosin binding affinity in structural studies [160]. We have previously demonstrated that Helix W, located near the cleft in the Lower 50kDa domain, experiences a significant shift in orientation relative to actin upon binding of MgADP by myosin [137]. However, just as with the relay helix, analysis of this change

was limited by a lack of sufficient modeling constraints.

In the present study, additional constraints from DEER have allowed for true modeling of changes to both Helix K and Helix W with MgADP binding/release. We have quantified shifts in both helices away from the actomyosin interface, indicating a subtle opening of the actin-binding cleft when MgADP is present (Figure 5.5). In the cleft-affinity relationship proposed above, this correlates with a decrease in actin-binding affinity, thus providing a direct structural basis for the reciprocal affinities of myosin for actin and MgADP. The behavior of both helices also aligns well with recent structural and spectroscopic studies in myosin V, where nucleotide-dependent changes near the actomyosin interface were mainly detected as flexibility in the Lower 50kDa domain, while the Upper 50kDa domain remained relatively static [49, 161]; indeed, our modeled result for myosin II follows a similar pattern.

While these results provide a compelling explanation for myosin's classic behavior, it is worth noting that the reciprocal affinity effect is blunted by at least an order of magnitude in the *Dictyostelium* construct that serves as our background for site-directed labeling. In wild-type *Dictyostelium* myosin, MgADP affinity is reduced roughly 100-fold upon actin binding, but substitution of native cysteines and truncation of the construct at residue 758 are both correlated with drastic attenuation of this effect [52, 162–164]. Thus, it is possible that the effect we observe here is less pronounced than it would be in a wild-type motor. In the future, additional studies using longer myosin constructs would be invaluable for investigating the apparent allosteric coupling mediated by the C-terminus; optimization of

labeling methods may also permit the study of constructs with some native cysteines restored.

5.5.4 Restrained simulations and additional labeling sites would further refine reported models.

In this study, we have successfully employed two complementary EPR methods to resolve and model two significant structural transitions in actin-bound myosin: one in the force-generating domain of the CD, and one at the actomyosin interface. We have also determined the nature of BSL binding to α-helices in intimate detail, verifying its stereoselectivity and generating model conformations with applicability to other sites and other systems. While each of these modeled results carries near-atomic resolution due to the multiple experimental constraints employed, it is not possible to generate a full atomistic rendering of myosin's structural state from the movements of three individual helices alone.

One of our major future goals is to investigate how the movement of a helix affects the overall structure of the domain surrounding it. Restrained molecular dynamics (RMD) simulations have been used for this purpose in other systems, particularly in conjunction with DEER-derived distances [95, 165, 166]. Briefly, the method applies harmonic restraints to keep various parameters (like inter-spin distances) centered around an experimentally-determined mean during a simulation, while allowing the rest of the system to equilibrate around the restrained regions. Preliminary data suggests that it is possible to constrain both distance and orientation simultaneously, with orientational restraints implemented as torsional springs acting on a calculated nitroxide frame (Figure 5.7). Such a simulation would

preserve all of the structural information derived from the current study, while enabling a detailed analysis of local effects due to the observed rearrangements. Furthermore, proper tuning of force constants could effectively recapitulate the level of disorder observed in EPR, which is currently not considered in our atomistic models.

The DEER experiments implemented here have also enabled a comparison between actin-free and actin-bound myosin which was not possible in our earlier study of oriented fibers (Figure 5.6). Observed distance changes across the cleft (HK-to-HW construct) are on the order of those previously determined at similar sites by DEER with monofunctional labels [45]. The obvious advantage of BSL is its tightly-defined relationship with the protein backbone, but without more information it is difficult to draw definitive conclusions about the behavior of the cleft. A small number of additional labeling sites would quickly alleviate this ambiguity, enabling cross-comparison of one label's position against multiple others.

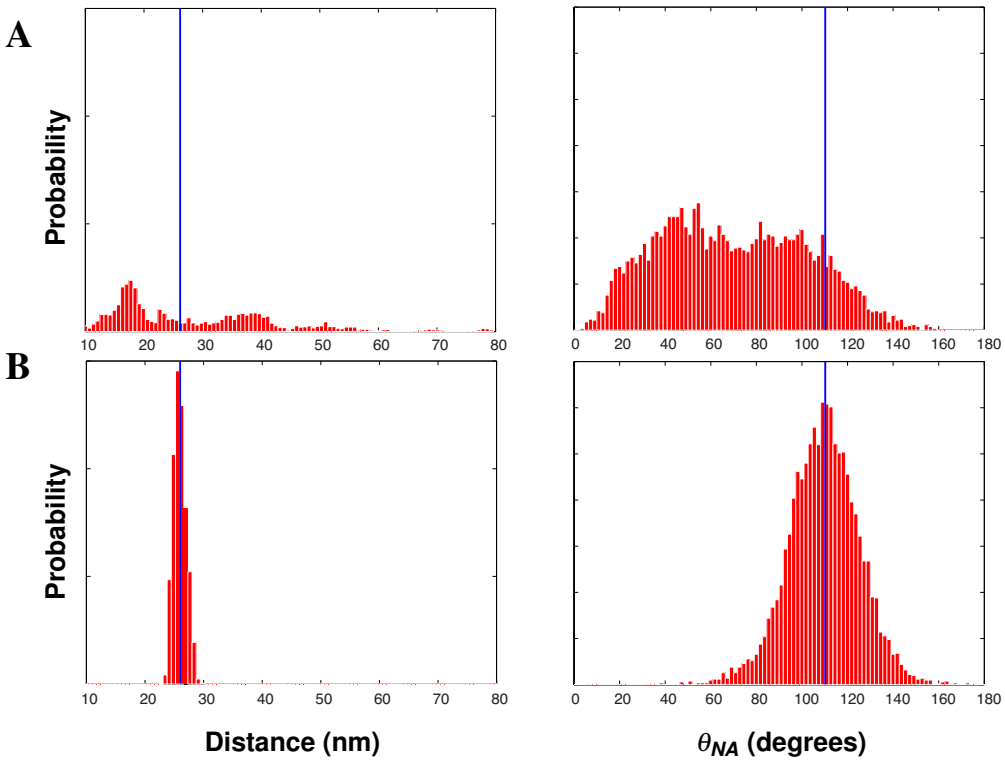

Figure 5.7. Probability distributions from preliminary restrained MD simulations on spin-labeled myosin. A-B: Histograms generated from two molecular dynamics trajectories, both built using spin-labeled helices from the final apo model in Figure 5.4. Plots depict inter-spin distances between labels on the relay helix and Helix W (left), and θ_{NA} from the relay helix site (right). The initial state of the model is indicated with blue lines. A: 100ps simulation of isolated helices in implicit solvent, with no added restraints. B: Same simulation as in A, with harmonic restraints placed on the inter-spin vector and the orientation of the nitroxide coordinate frame. Equilibrium positions for both restraints were set to measurements from the initial state (blue lines). Data shows that both orientation and distance information from the current study can be effectively preserved in simulations; further tuning of the restraints will allow for greater control over the width of the distributions.

5.6 Supplementary Information

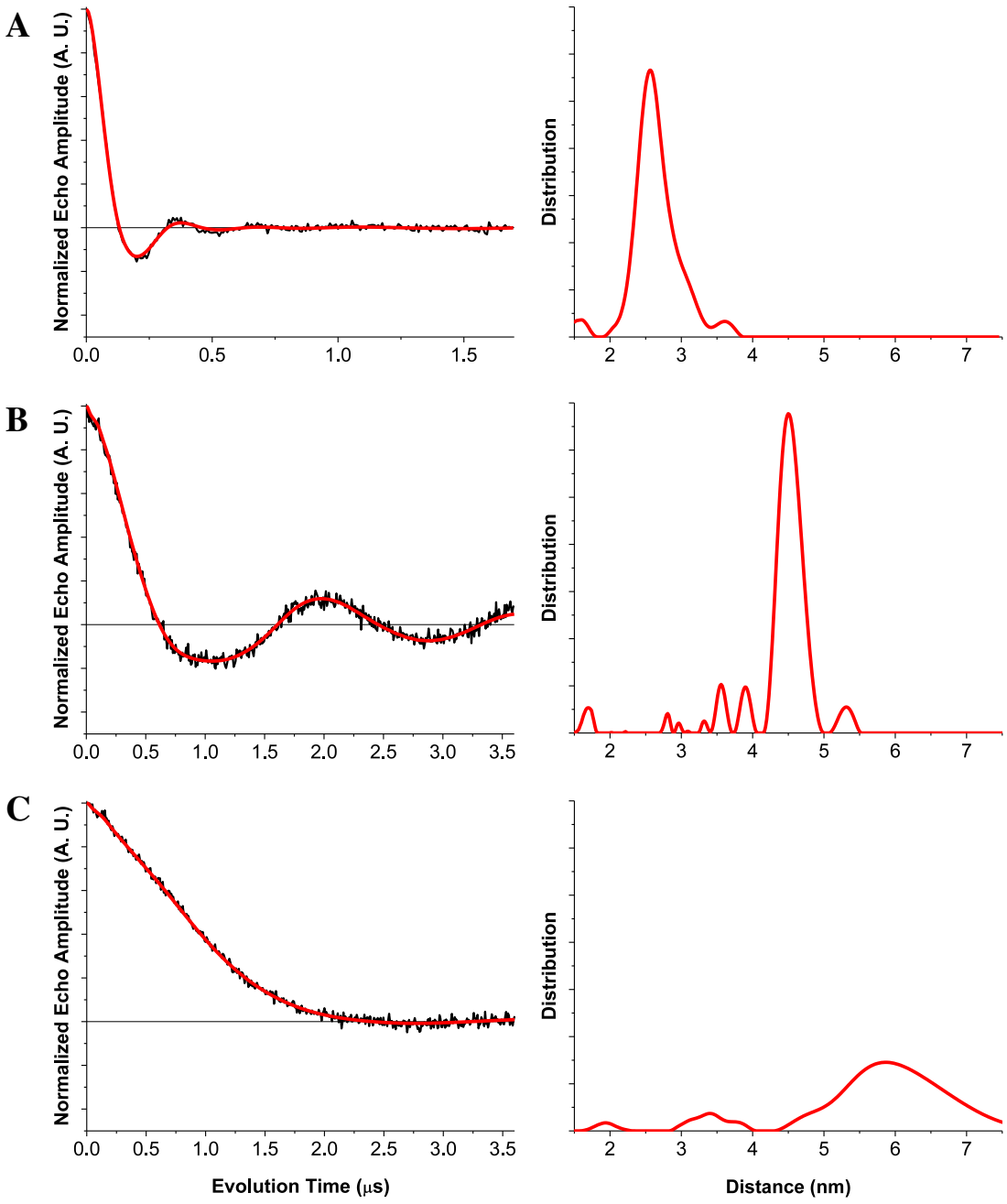

Figure 5.8. DEER for all three possible BSL site pairs, in the absence of actin and nucleotides. Left: Background-corrected DEER waveforms for 492.496.639.643-BSL (relay-to-HW, A), 325.329.639.643-BSL (HK-to-HW, B), and 325.329.492.496-BSL (HK-to-relay, C), normalized to modulation depth (horizontal line), with best-fit Tikhonov simulations overlaid (red). Right: Distance distributions corresponding to the Tikhonov-based simulations at left. While A and B give narrow distributions within the sensitive range of DEER, the distribution in C is unreliable, being highly susceptible to artifacts from background subtraction.

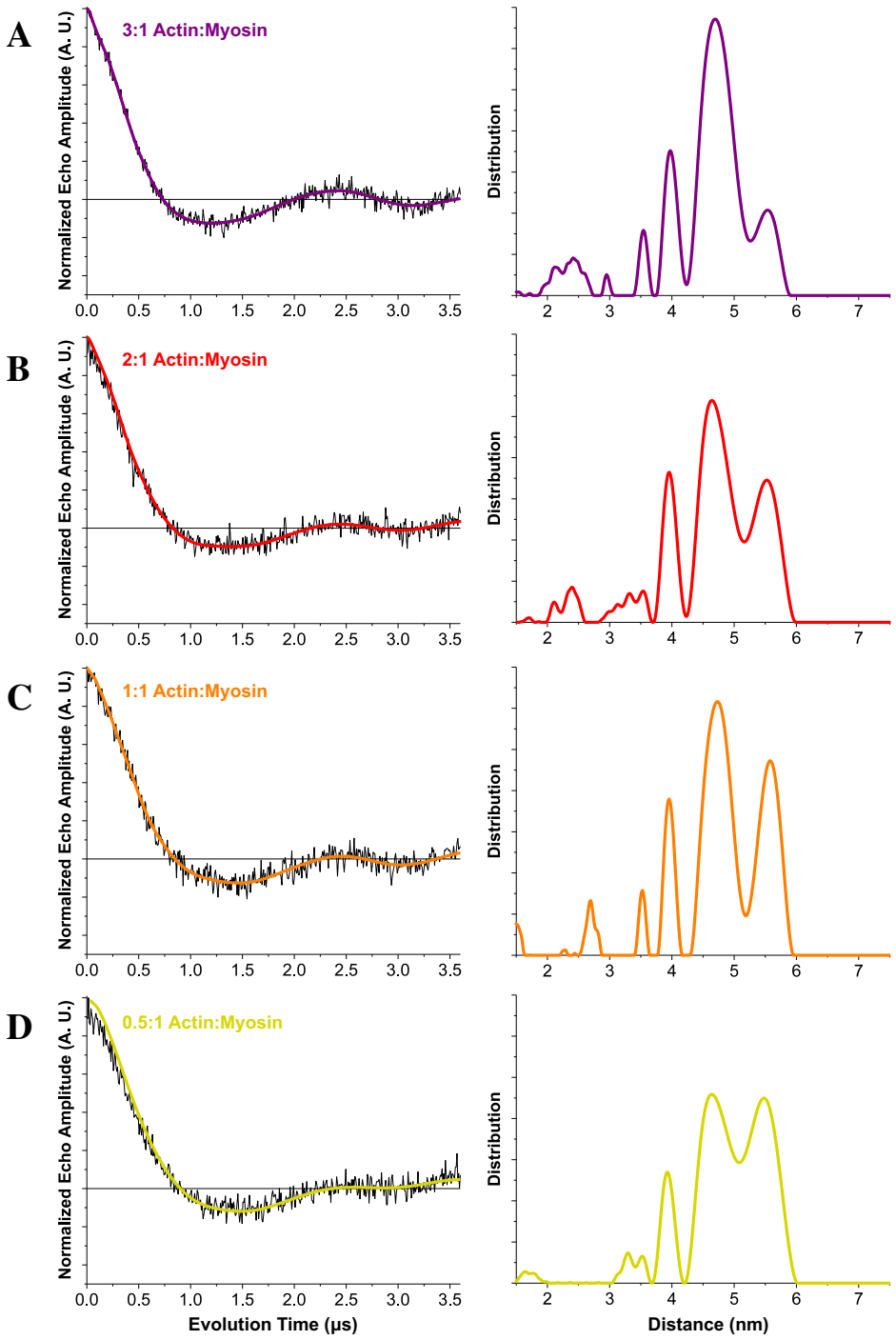

Figure 5.9. The effect of the actin-to-myosin ratio on DEER from the HK-to-HW construct. Left: Background-corrected DEER waveforms for 325.329.639.643-BSL (HK-to-HW), normalized to modulation depth (horizontal line), with best-fit Tikhonov simulations overlaid. Right: Distance distributions corresponding to the Tikhonov-based simulations at left. From top, data corresponds to samples made with 3:1 (A), 2:1 (B), 1:1 (C), and 0.5:1 (D) actin:myosin (mol/mol).

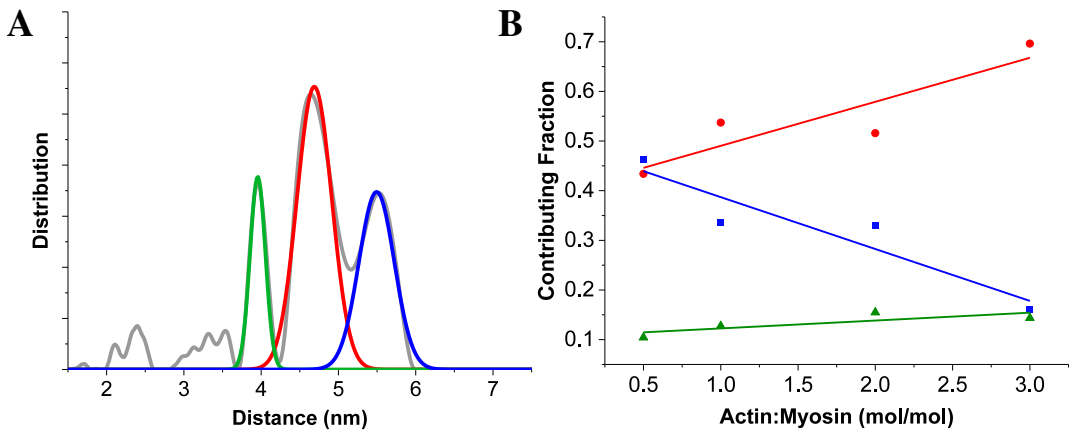

Figure 5.10. Contributions of distance sub-populations for the HK-to-HW construct, as a function of actin:myosin ratio. A: Representative distance distribution plot for HK-to-HW, showing the best-fit Tikhonov distribution (gray), and major sub-populations modeled as Gaussian fits to the Tikhonov (short distance, green; intermediate distance, red; long distance, blue). B: Scatter plot with linear fits, showing contributions of each sub-population from A to the overall distribution, as a function of the actin:myosin ratio. Contributing fraction was calculated by dividing the area under the fitted Gaussian by the total area under the Tikhonov for each distribution in Figure 5.9.

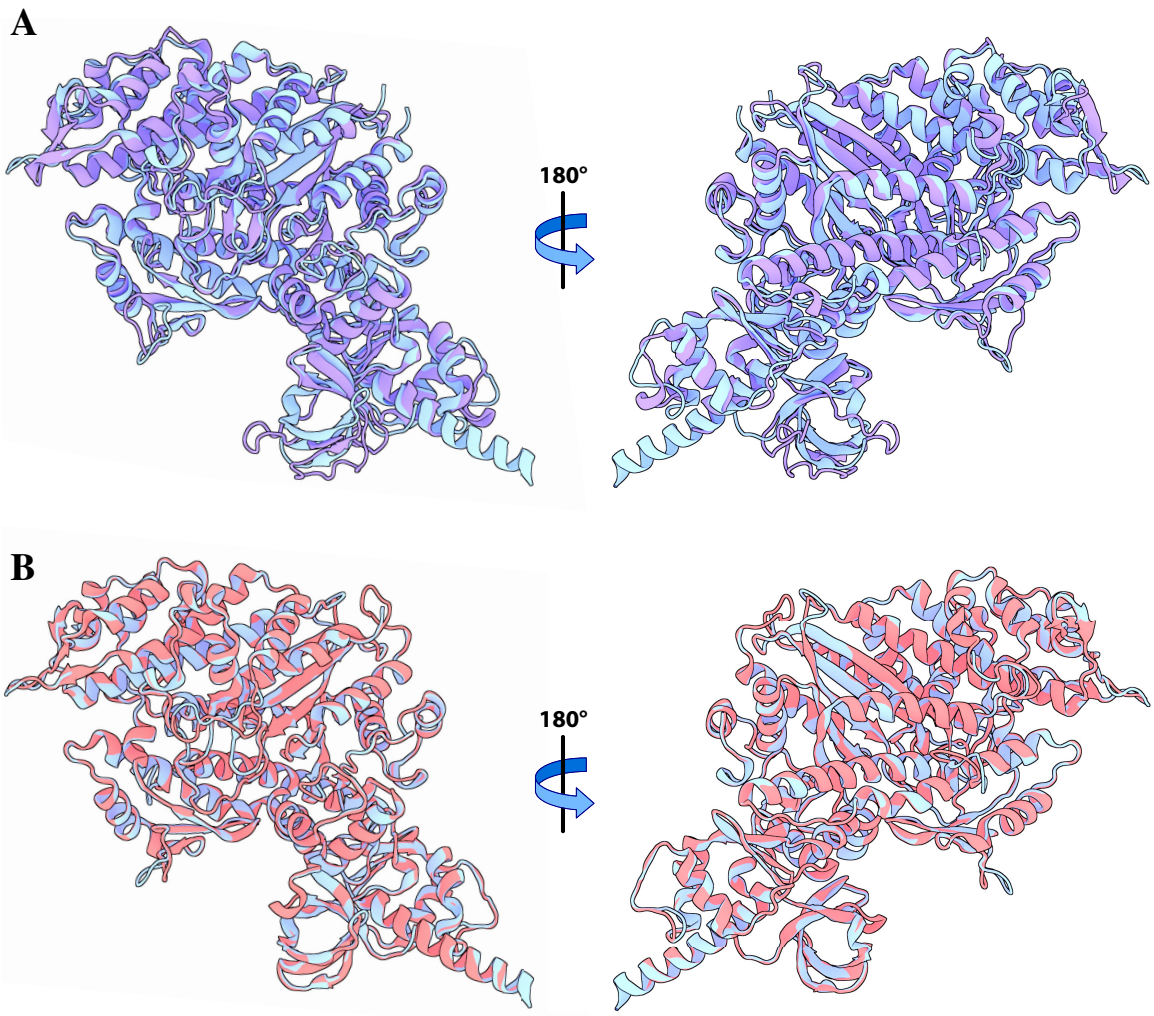

Figure 5.11. Structural alignments of rigor myosin models. A: Alignment of structure 5JLH (blue, derived from cryo-EM on a rigor complex of human cytoplasmic myosin IIc [69]) with structure 1W8J (purple, a myosin V structure which has been used as a model for the rigor state, and agrees well with previous cryo-EM data [45, 61, 114, 151]). B: Alignment of structure 5JLH (blue) with the homology model introduced in Section 5.4 (red, built from the *Dictyostelium* myosin motor domain sequence using 5JLH as a template [147–150]).

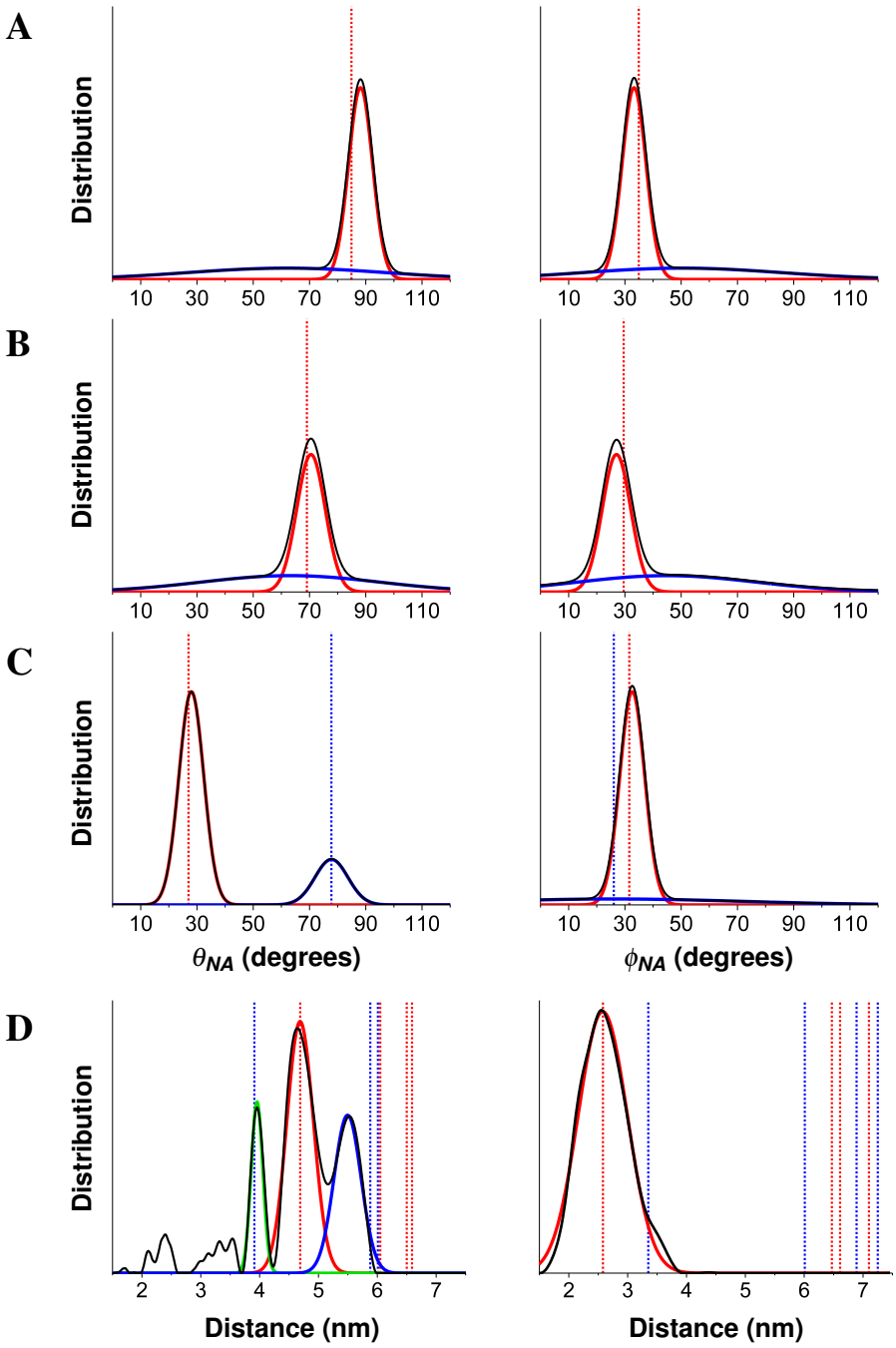

Figure 5.12. Agreement between experimental and model-calculated measurements of orientation and distance. A-C: Orientational distributions derived from EPR on oriented fibers, with BSL labels on helix K (A), the relay helix (B), or helix W (C). D: Distance distributions from the HK-to-HW construct (left) or the relay-to-HW construct (right). Distribution envelopes are solid black; primary, secondary, and tertiary Gaussian components are solid red, blue, and green, respectively. Dashed red lines represent model-calculated measurements from the primary BSL conformation; dashed blue lines represent measurements involving an alternate conformer on Helix W.

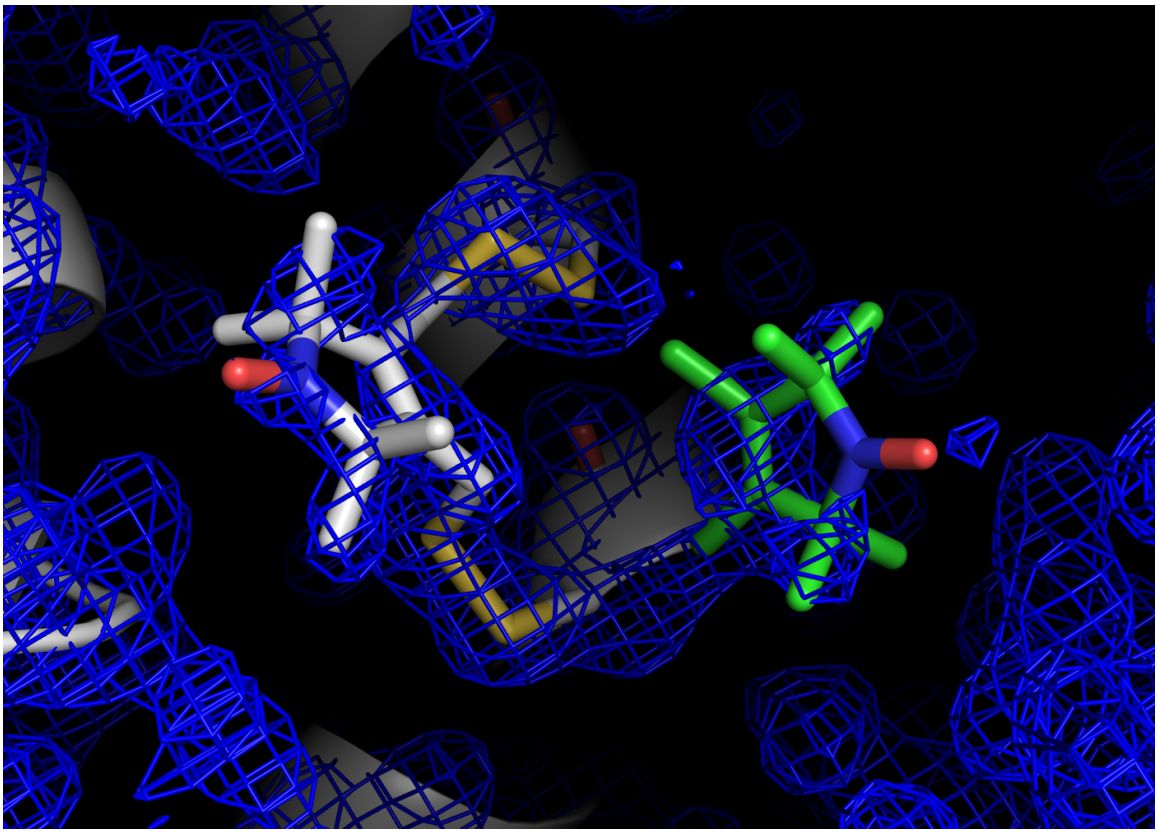

Figure 5.13. Alternate conformation of BSL, derived from electron density. White: Protein backbone structure (ribbons) and bifunctionally-attached BSL (sticks) from structure 3L2X [94]. Blue: Electron density map from which structure 3L2X was derived. Green: BSL's five-membered ring and primary substituents, duplicated using the 3L2X coordinates and positioned by rigid-body fitting into a pocket of unfitted density near the labeling site.

		Experiment	Model	Difference
Actin-BSL Axial Angle, θ_{NA} (°)	Helix W	77.8	77.8	0.0
Actin-BSL Azimuthal Angle, ϕ_{NA} (°)	Helix W	26.0	26.0	0.0
Intra-Helix Distances (nm)	HK-to-HW	3.95	3.91	0.04
	Relay-to-HW	–	3.35	–

Table 5.5. Comparison of EPR experimental constraints for the nucleotide-free actomyosin complex with measurements derived from an alternate conformation on Helix W. All experimental constraints listed correspond to the peak positions of secondary (or tertiary) sub-populations within the derived distribution (see accompanying Figure 5.12). An experimental relay-to-HW distance is not given here because the Tikhonov distance distribution could only be fit reliably to one Gaussian, and thus a secondary distance was not included in the minimization; however, the 3.35nm distance that arose spontaneously during the minimization aligns well with a shoulder in the Tikhonov distribution (Figure 5.12). The minimum depicted here was achieved with the following transformation parameters (Equation 5.2): $\alpha_N = 0.7°$, $\beta_N = 13.4°$, $\gamma_N = 0.4°$, $\psi = 29.3°$, $a = -1.2$Å, and $b = -0.8$Å.

	Yaw Angle, α_H (°)	Pitch Angle, β_H (°)	Roll Angle, γ_H (°)	u (Å)	v (Å)	w (Å)
Helix K	1.1	-3.2	-9.7	0.47	-0.82	0.58
Relay Helix	0.3	-15.1	-7.4	1.84	-0.36	0.26
Helix W	0.2	-7.4	2.3	-2.31	1.18	-0.32

Table 5.6. Optimal parameters for helix transformations in the refinement of the actomyosin MgADP-bound state. Parameters are defined in the main text with the discussion of Equation 5.4.

CHAPTER 6: FUTURE DIRECTIONS

6.1 Introduction

The work presented in Chapters 4 and 5 represents an ongoing fulfillment of the research motivations outlined in Chapters 2 and 3. Fundamental insight has been gained into the mechanism of myosin's mechanochemical coupling, and the use of BSL as a novel spectroscopic tool has been thoroughly explored. These projects have placed consistent, heavy emphasis on methods development, and thus opportunities for ongoing research follow from three general approaches.

First, as discussed particularly in Section 5.5, the elucidation of ADP-induced changes in actin-bound myosin can be enhanced through additional *in vitro* and *in silico* experiments. This approach amounts to a further extension of my previous efforts in biophysical methods development, aimed at answering a specific structural question at the greatest possible level of detail. Second, the methods and protein constructs developed for Chapters 4 and 5 can be readily applied to investigate other important questions related to the actomyosin complex. This approach relies on the work from Chapters 4 and 5 as effective proof of principle, and seeks to apply those same methods directly to a new series of inquiries. The third potential approach is the most personally intriguing option, and represents the greatest potential challenge. The spin-labeling methods and subsequent modes of analysis presented so far are not exclusively applicable to myosin, and their impact has even greater potential in systems for which no atomistic structures yet exist. In the following sections,

each of these potential approaches are discussed in detail.

6.2 Full Elucidation of the Strongly-Bound Structural States of Myosin

The effect of MgADP binding/release from the actomyosin rigor complex has been the primary focus of the research presented in Chapters 4 and 5, and it has so far served as a useful case study in the development of biophysical methods for structure elucidation in actomyosin. However, Section 5.5 points out multiple ways that the picture obtained from the current work can still be improved.

The ultimate end to which this work aspires is nothing less than a full atomistic model of the actomyosin complex, refined by results from EPR to represent different biochemical states. Probes placed in strategic locations would inform both the position *and* local disorder associated with individual helices, and experimental refinement of those helices would in turn influence the reported behavior of subdomains. Section 5.5 contains preliminary data and a brief discussion for how such a model could be obtained through the use of restrained molecular dynamics simulations (RMD). Indeed, a simple version of this approach is planned for inclusion in the final manuscript upon which Chapter 5 is based. As with most spectroscopic techniques in structural biology, data from additional labeling sites in the CD (either from DEER, oriented fiber EPR, or both) would greatly enhance the integrity of the final model. In particular, additional sites on the Upper and Lower 50kDa domains near the actin-binding cleft would allow for more comprehensive modeling of the MgADP-induced changes already observed.

Section 5.5 also acknowledges the potential effect of our construct's design on the interpretation of current results. Devoid of native cysteines and a short, crucial C-terminal extension, the "Cys-Lite" construct used in all experiments thus far has been shown to retain extremely high affinity for both actin and MgADP in a ternary complex (on the order of 1μM) relative to wild-type, suggesting that the effect of MgADP binding on CD structure is attenuated by these changes [52, 162–164]. On the one hand, this is an useful artifact because it stabilizes the ternary complex and enables reliable observation, but previous studies have shown that the reciprocal affinity relationship can be carefully tuned by selective incorporation and/or omission of individual cysteines [52]. Thus, further investigations of the actin-binding cleft would be greatly aided by a comparison with constructs which are either longer, or have one or more native cysteines restored.

The latter case necessarily creates challenges for our site-directed labeling approach, because additional cysteines would be susceptible to nonspecific labeling by BSL during sample preparation. However, some progress has already been made in this direction: preliminary studies on recombinant calmodulin constructs have shown that methanethiosulfonate (MTS) labels like BSL can completely react with cysteines even in the presence of significant amounts ($\sim$1mM) of mild reducing agents like TCEP. BSL is expected to have much greater affinity for di-Cys motifs than single cysteines, because the local effective concentration of its second MTS group is very large once the first MTS group forms its disulfide linkage. It is likely, therefore, that labeling conditions which preserve specificity in non-"Cys-Lite" constructs can be found. While helpful in the continued pursuit of our

studies in myosin, a successful protocol of this nature would be tremendously impactful for BSL's applicability in other systems as well. The ability to employ this label in proteins without first eliminating other reactive cysteines would circumvent a great hurdle that has plagued the field of site-directed spectroscopy since its inception.

6.3 Pathological Mutations and Small-Molecule Affectors

The MgADP case study pursued in Chapters 4 and 5 represents just one of a vast array of potential investigations involving the actomyosin complex, which directly apply the established methods to answer additional questions regarding function and pathology. The most readily feasible projects would retain existing labeling sites, alleviating the need to augment or restructure the analysis workflow detailed in Chapter 5. Two major avenues of future study are immediately apparent: investigation of disease-causing mutations in the CD, and evaluation of the effects of various small molecules on the structure of the complex.

Cardiac myosin is among the most heavily cited muscle proteins for inherited mutations which give rise to hypertrophic cardiomyopathy (HCM) [100, 167, 168]. Despite over 300 distinct mutations having been identified in myosin and its associated light chains, very little is understood about the structural repercussions of individual point mutations. The pool of potential candidates is very large, but fortunately, several of these mutations have already been shown to render conserved effects in *Dictyostelium* myosin CD [169, 170]. Existing myosin constructs engineered for the work in Chapters 4 and 5 represent an ideal

platform for the study of small modifications like these HCM mutations, and the library of "pre-vetted" options provided by previous studies in *Dictyostelium* myosin serves as an attainable initial goal. Because each mutation is correlated with a significant shift in myosin's enzyme kinetics, we hypothesize that each has a detectable effect on local protein structure, which can be measured using our approach.

Another immediate application lies in investigating the allosteric consequences of small molecule binding within the CD. Several compounds targeting myosin have been identified as potential therapeutic agents for the treatment of HCM and heart failure [171–174]. Intelligent, efficient design of small molecule drugs relies on the ability of synthetic chemists to optimize the structure of a compound for the greatest clinical benefit. This process is heavily dependent on a proper understanding of how each molecule binds myosin, and how that binding event renders a significant impact on structure and function. While in certain cases it has been possible to crystallize myosin in the presence of a given affector [175], traditional structural techniques are unlikely to provide timely, accurate results especially for actin-bound myosin, due to the inherent difficulty of preparing a homogenous ternary complex *in crystallo*. The methods described in Chapters 4 and 5 do not suffer from these issues, and thus EPR-based structural modeling could provide a much-needed platform for aiding drug discovery and refinement efforts. In fact, preliminary data in oriented fibers shows that this approach is indeed sensitive enough to detect small changes in protein structure upon drug binding: binding of the small molecule omecamtiv mecarbil causes a slight shift in the orientation of the relay helix (Figure 6.1). Such experiments do

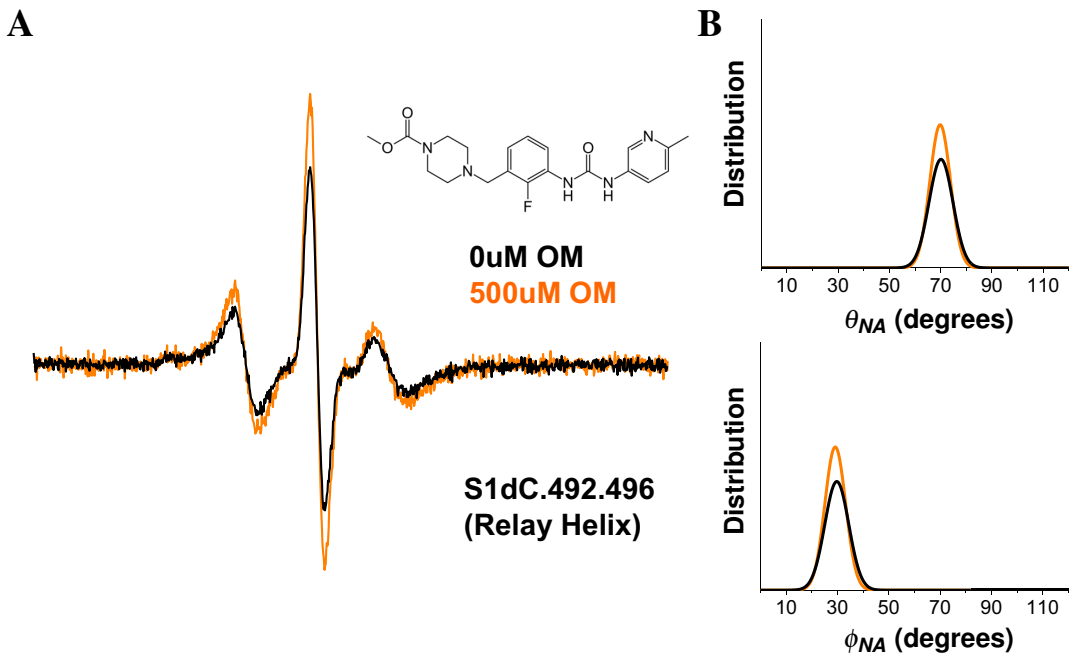

Figure 6.1. Preliminary study on the structural effects induced by binding of omecamtiv mecarbil to actin-bound myosin. A: Comparison of spectra from 492.496-BSL on parallel-oriented fibers, acquired in the presence of 0μM (black) and 500μM (orange) omecamtiv mecarbil (structure pictured above spectrum). B: Orientational distributions for θ_{NA} and ϕ_{NA} derived from the spectra in A. Distributions show a negligible shift in center, but a significant difference in width between the two conditions. Omecamtiv mecarbil appears to have ordering effect on the relay helix, which makes sense in the context of a recent crystal structure, which shows the drug binding near the relay helix [175]. Further studies could elaborate on the allosteric repercussions of this change.

not require any additional modification of methods or constructs, and thus represent the most attractive immediate application of the present work.

6.4 Structure Determination in Systems Beyond Myosin

Chapters 4 and 5 demonstrate the high precision and accuracy of an EPR-based approach to structure determination enabled by the use of BSL. These methods are effective

for detecting and modeling changes within actomyosin, but the myosin CD has a well-studied structure, and radical discoveries concerning the overall topology of the protein are not expected. The high resolving potential of the methodology, however, begs for further application where protein conformations and interactions are not so well-characterized.

In order to take full advantage of the approach, a chosen system must have the ability to become oriented about a symmetry axis in the laboratory frame—this is necessary for obtaining orientational distributions from CW-EPR. Proteins which bind to actin are the most obvious choice for new applications; indeed, there are many important cytoskeletal and sarcomeric proteins about which very little is known in terms of bound structure. Utrophin and dystrophin, myosin-binding protein C, α-actinin, and β-spectrin are all examples of actin-binding proteins studied by the Thomas Lab and its close collaborators, and each of these is lacking a high-resolution structural model in complex with actin. Study of the myosin light chain domain is also a potential target, through exchange of spin-labeled light chains onto endogenous myosin within skinned muscle fibers [176].

Proteins need not associate with a rigid polymer scaffold for orientation measurements. Much recent work has been accomplished in the development of oriented bicelle applications for EPR spectroscopy at conventional X-band frequencies [136, 177–180]. The technique relies on tuning the inherent magnetic susceptibility of lipid bicelles (bilayered micelles) so that they align either parallel or perpendicular to $\vec{B}$ in the EPR instrument. Doing so establishes a globally-consistent orientation for the membrane normal, allowing membrane-bound proteins to be studied in much the same way as actin-bound proteins in

oriented fibers. Indeed, we have employed this approach recently with BSL in the elucidation of structural states for phospholamban [153].

Thus, applications outside of the myosin CD for the methods presented in Chapters 4 and 5 are very broad. Considerable challenges may be inherent in the design of constructs compatible with site-directed labeling for some proteins, but for others, including some of the examples cited above, a lack of native cysteines avoids the issue entirely [79, 80]. The potential to characterize brand-new structural models for proteins without crystal structures is an especially appealing component of this future aim.

BIBLIOGRAPHY

1. Saladin, K. S. *Anatomy & physiology: the unity of form and function* (McGraw-Hill, 2014).
2. Alberts, B., Johnson, A., Walter, P., Lewis, J. & Raff, M. *Molecular biology of the cell* (Taylor & Francis Ltd., 2014).
3. Motta, P. M. *Ultrastructure of smooth muscle* (Springer US, 2012).
4. Lieber, R. L. *Skeletal muscle structure, function, and plasticity* (Lippincott Williams and Wilkins, 2009).
5. Maneski, L. Z. P., Maleevi, N. M., Savi, A. M., Keller, T. & Popovi, D. B. Surface-distributed low-frequency asynchronous stimulation delays fatigue of stimulated muscles. *Muscle Nerve* **48,** 930–937 (2013).
6. Zammit, P. S., Partridge, T. A. & Yablonka-Reuveni, Z. The skeletal muscle satellite cell: the stem cell that came in from the cold. *J. Histochem. Cytochem.* **54,** 1177–1191 (2006).
7. Winslow, R. L., Walker, M. A. & Greenstein, J. L. Modeling calcium regulation of contraction, energetics, signaling, and transcription in the cardiac myocyte. *Wiley Interdiscip. Rev. Syst. Biol. Med.* **8,** 37–67 (2016).
8. Huxley, A. F. & Niedergerke, R. Structural changes in muscle during contraction; interference microscopy of living muscle fibres. *Nature* **173,** 971–3 (1954).
9. Huxley, H. & Hanson, J. Changes in the cross-striations of muscle during contraction and stretch and their structural interpretation. *Nature* **173,** 973–6 (1954).
10. Huxley, H. E. Fifty years of muscle and the sliding filament hypothesis. *Eur. J. Biochem.* **271,** 1403–15 (2004).
11. Walklate, J., Ujfalusi, Z. & Geeves, M. A. Myosin isoforms and the mechanochemical cross-bridge cycle. *J. Exp. Biol.* **219,** 168–174 (2016).
12. Hartman, M. A. & Spudich, J. A. The myosin superfamily at a glance. *J. Cell Sci.* **125,** 1627–1632 (2012).
13. Sellers, J. R. Myosins: a diverse superfamily. *Biochim. Biophys. Acta* **1496,** 3–22 (2000).
14. Masters, T. A., Kendrick-Jones, J. & Buss, F. Myosins: Domain Organisation, Motor Properties, Physiological Roles and Cellular Functions. *Handb. Exp. Pharmacol.* (2016).
15. McIntosh, B. B. & Ostap, E. M. Myosin-I molecular motors at a glance. *J. Cell Sci.* **129,** 2689–2695 (2016).
16. Trybus, K. M. Myosin V from head to tail. *Cell. Mol. Life Sci.* **65,** 1378–1389 (2008).

17. Sweeney, H. L. & Houdusse, A. Myosin VI rewrites the rules for myosin motors. *Cell* **141,** 573–582 (2010).

18. Li, J., Lu, Q. & Zhang, M. Structural basis of cargo recognition by unconventional myosins in cellular trafficking. *Traffic* **17,** 822–838 (2016).

19. Gulick, A. M., Bauer, C. B., Thoden, J. B. & Rayment, I. X-ray structures of the MgADP, MgATPgammaS, and MgAMPPNP complexes of the Dictyostelium discoideum myosin motor domain. *Biochemistry* **36,** 11619–28. (1997).

20. Debreczeni, J. E. *et al.* Structural evidence for non-canonical binding of Ca2+ to a canonical EF-hand of a conventional myosin. *J. Biol. Chem.* **280,** 41458–41464 (2005).

21. Alamo, L. *et al.* Conserved Intramolecular Interactions Maintain Myosin Interacting-Heads Motifs Explaining Tarantula Muscle Super-Relaxed State Structural Basis. *J. Mol. Biol.* **428,** 1142–1164 (2016).

22. Blankenfeldt, W., Thom, N. H., Wray, J. S., Gautel, M. & Schlichting, I. Crystal structures of human cardiac beta-myosin II S2-delta provide insight into the functional role of the S2 subfragment. *Proc. Natl. Acad. Sci. U. S. A.* **103,** 17713–17717 (2006).

23. Geeves, M. A. Review: The ATPase mechanism of myosin and actomyosin. *Biopolymers* **105,** 483–491 (2016).

24. Lymn, R. W. & Taylor, E. W. Mechanism of adenosine triphosphate hydrolysis by actomyosin. *Biochemistry* **10,** 4617–24. (1971).

25. Houdusse, A. & Sweeney, H. L. How myosin generates force on actin filaments. *Trends in biochemical sciences* **41,** 989–997 (2016).

26. Muretta, J. M., Petersen, K. J. & Thomas, D. D. Direct real-time detection of the actin-activated power stroke within the myosin catalytic domain. *Proc. Natl. Acad. Sci. U. S. A.* **110,** 7211–6 (2013).

27. Muretta, J. M., Rohde, J. A., Johnsrud, D. O., Cornea, S. & Thomas, D. D. Direct real-time detection of the structural and biochemical events in the myosin power stroke. *Proc. Natl. Acad. Sci. U. S. A.* **112,** 14272–14277 (2015).

28. Veigel, C. *et al.* The motor protein myosin-I produces its working stroke in two steps. *Nature* **398,** 530–533 (1999).

29. Capitanio, M *et al.* Two independent mechanical events in the interaction cycle of skeletal muscle myosin with actin. *Proc. Natl. Acad. Sci. U. S. A.* **103,** 87–92 (2006).

30. Trivedi, D. V. *et al.* Direct measurements of the coordination of lever arm swing and the catalytic cycle in myosin V. *Proc. Natl. Acad. Sci. U. S. A.* **112,** 14593–14598 (2015).

31. Greenberg, M. J., Lin, T., Goldman, Y. E., Shuman, H. & Ostap, E. M. Myosin Ic generates power over a range of loads via a new tension-sensing mechanism. *Proc. Natl. Acad. Sci. U. S. A.* **109,** E2433–40 (2012).

32. Greenberg, M. J., Shuman, H. & Ostap, E. M. Inherent force-dependent properties of beta-cardiac myosin contribute to the force-velocity relationship of cardiac muscle. *Biophys. J.* **107,** L41–4 (2014).

33. Resnicow, D. I., Deacon, J. C., Warrick, H. M., Spudich, J. A. & Leinwand, L. A. Functional diversity among a family of human skeletal muscle myosin motors. *Proc. Natl. Acad. Sci. U. S. A.* **107,** 1053–1058 (2010).

34. Ausoni, S, Gorza, L, Schiaffino, S, Gundersen, K & Lmo, T. Expression of myosin heavy chain isoforms in stimulated fast and slow rat muscles. *J. Neurosci.* **10,** 153–160 (1990).

35. Reiser, P. J., Portman, M. A., Ning, X. H. & Schomisch Moravec, C. Human cardiac myosin heavy chain isoforms in fetal and failing adult atria and ventricles. *Am. J. Physiol. Heart Circ. Physiol.* **280,** H1814–H1820 (2001).

36. Beach, J. R. & Hammer, J. A. Myosin II isoform co-assembly and differential regulation in mammalian systems. *Exp. Cell Res.* **334,** 2–9 (2015).

37. Bosgraaf, L. & van Haastert, P. J. M. The regulation of myosin II in Dictyostelium. *Eur. J. Cell Biol.* **85,** 969–979 (2006).

38. Tee, Y. H. *et al.* Cellular chirality arising from the self-organization of the actin cytoskeleton. *Nat. Cell Biol.* **17,** 445–457 (2015).

39. Sasaki, N., Ohkura, R. & Sutoh, K. Dictyostelium myosin II as a model to study the actin-myosin interactions during force generation. *J. Muscle Res. Cell Motil.* **23,** 697–702 (2002).

40. Agafonov, R. V., Nesmelov, Y. E., Titus, M. A. & Thomas, D. D. Muscle and non-muscle myosins probed by a spin label at equivalent sites in the force-generating domain. *Proc. Natl. Acad. Sci. U. S. A.* **105,** 13397–402 (2008).

41. Manstein, D. J., Ruppel, K. M. & Spudich, J. A. Expression and characterization of a functional myosin head fragment in Dictyostelium discoideum. *Science* **246,** 656–658 (1989).

42. Mornet, D., Bertrand, R., Pantel, P., Audemard, E. & Kassab, R. Structure of the actin-myosin interface. *Nature* **292,** 301–6. (1981).

43. Mendelson, R. & Morris, E. P. The structure of the acto-myosin subfragment 1 complex: results of searches using data from electron microscopy and X-ray crystallography. *Proc. Natl. Acad. Sci. U. S. A.* **94,** 8533–8. (1997).

44. Andreev, O. A. & Reshetnyak, Y. K. Mechanism of formation of actomyosin interface. *J. Mol. Biol.* **365,** 551–554 (2007).

45. Klein, J. C. *et al.* Actin-binding cleft closure in myosin II probed by site-directed spin labeling and pulsed EPR. *Proc. Natl. Acad. Sci. U. S. A.* **105,** 12867–72 (2008).

46. Spudich, J. A. The myosin mesa and a possible unifying hypothesis for the molecular basis of human hypertrophic cardiomyopathy. *Biochem. Soc. Trans.* **43,** 64–72 (2015).

47. Hooijman, P., Stewart, M. A. & Cooke, R. A new state of cardiac myosin with very slow ATP turnover: a potential cardioprotective mechanism in the heart. *Biophys. J.* **100,** 1969–1976 (2011).

48. Nogara, L. *et al.* Spectroscopic studies of the super relaxed state of skeletal muscle. *PLoS One* **11,** e0160100 (2016).

49. Wulf, S. F. *et al.* Force-producing ADP state of myosin bound to actin. *Proc. Natl. Acad. Sci. U. S. A.* **113,** E1844–E1852 (2016).

50. Shih, W. M. & Spudich, J. A. The myosin relay helix to converter interface remains intact throughout the actomyosin ATPase cycle. *J. Biol. Chem.* **276,** 19491–19494 (2001).

51. Baumketner, A. The mechanism of the converter domain rotation in the recovery stroke of myosin motor protein. *Proteins* **80,** 2701–2710 (2012).

52. Guhathakurta, P., Prochniewicz, E., Muretta, J. M., Titus, M. A. & Thomas, D. D. Allosteric communication in Dictyostelium myosin II. *J. Muscle Res. Cell Motil.* (2012).

53. Cheung, H., Gonsoulin, F & Garland, F. An investigation of the SH1-SH2 and SH1-ATPase distances in myosin subfragment-1 by resonance energy transfer using nanosecond fluorimetry. *Biochim. Biophys. Acta* **832,** 52–62 (1985).

54. Mello, R. N. & Thomas, D. D. Three distinct actin-attached structural states of myosin in muscle fibers. *Biophys. J.* **102,** 1088–96 (2012).

55. Kintses, B., Yang, Z. & Mlnsi-Csizmadia, A. Experimental investigation of the see-saw mechanism of the relay region that moves the myosin lever arm. *J. Biol. Chem.* **283,** 34121–34128 (2008).

56. Agafonov, R. V. *et al.* Structural dynamics of the myosin relay helix by time-resolved EPR and FRET. *Proc. Natl. Acad. Sci. U. S. A.* (2009).

57. Greenberg, M. J., Lin, T., Shuman, H. & Ostap, E. M. Mechanochemical tuning of myosin-I by the N-terminal region. *Proc. Natl. Acad. Sci. U. S. A.* **112,** E3337–E3344 (2015).

58. Shuman, H. *et al.* A vertebrate myosin-I structure reveals unique insights into myosin mechanochemical tuning. *Proc. Natl. Acad. Sci. U. S. A.* **111,** 2116–2121 (2014).

59. Khner, S. & Fischer, S. Structural mechanism of the ATP-induced dissociation of rigor myosin from actin. *Proc. Natl. Acad. Sci. U. S. A.* **108,** 7793–7798 (2011).

60. Geeves, M. A., Fedorov, R & Manstein, D. J. Molecular mechanism of actomyosin-based motility. *Cell. Mol. Life Sci.* **62,** 1462–1477 (2005).

61. Lorenz, M. & Holmes, K. C. The actin-myosin interface. *Proc. Natl. Acad. Sci. U. S. A.* **107,** 12529–12534 (2010).

62. Prochniewicz, E., Katayama, E., Yanagida, T. & Thomas, D. D. Cooperativity in F-actin: chemical modifications of actin monomers affect the functional interactions of myosin with unmodified monomers in the same actin filament. *Biophys. J.* **65,** 113–23 (1993).

63. Sung, J. *et al.* Harmonic force spectroscopy measures load-dependent kinetics of individual human beta-cardiac myosin molecules. *Nat. Commun.* **6,** 7931 (2015).

64. Goldman, Y. E., Hibberd, M. G., McCray, J. A. & Trentham, D. R. Relaxation of muscle fibres by photolysis of caged ATP. *Nature* **300,** 701–705 (1982).

65. Hirose, K, Lenart, T. D., Murray, J. M., Franzini-Armstrong, C & Goldman, Y. E. Flash and smash: rapid freezing of muscle fibers activated by photolysis of caged ATP. *Biophys. J.* **65,** 397–408 (1993).

66. Sun, Y. *et al.* Single-molecule stepping and structural dynamics of myosin X. *Nat. Struct. Mol. Biol.* **17,** 485–491 (2010).

67. Goldman, Y. E. & Veigel, C. Drunk or sober? myosin V walks the (quantum) dotted line in cells. *Biophys. J.* **97,** 399–400 (2009).

68. Wang, Y., Ajtai, K. & Burghardt, T. P. The Qdot-labeled actin super-resolution motility assay measures low-duty cycle muscle myosin step size. *Biochemistry* **52,** 1611–1621 (2013).

69. Von der Ecken, J., Heissler, S. M., Pathan-Chhatbar, S., Manstein, D. J. & Raunser, S. Cryo-EM structure of a human cytoplasmic actomyosin complex at near-atomic resolution. *Nature* **534,** 724–728 (2016).

70. Tajsharghi, H. & Oldfors, A. Myosinopathies: pathology and mechanisms. *Acta Neuropathol.* **125,** 3–18 (2013).

71. Weil, J. A. & Bolton, J. R. *Electron paramagnetic resonance : elementary theory and practical applications* (Wiley-Interscience, 2007).

72. Peleg, Y., Pnini, R., Zaarur, E. & Hecht, E. *Quantum mechanics* (McGraw-Hill, 2010).

73. Libertini, L. J. & Griffith, O. H. Orientation dependence of the electron spin resonance spectrum of di-t-butyl nitroxide. *J. Chem. Phys.* **53,** 1359–1367 (1970).

74. Griffith, O. H., Cornell, D. W. & McConnell, H. M. Nitrogen hyperfine tensor and g tensor of nitroxide radicals. *J. Chem. Phys.* **43,** 2909–2910 (1965).

75. Ding, Z., Gullá, A. F. & Budil, D. E. Ab initio calculations of electric field effects on the g-tensor of a nitroxide radical. *J. Chem. Phys.* **115,** 10685–10693 (2001).

76. Earle, K. A. & Budil, D. E. in *Advanced ESR Methods in Polymer Research* 53–83 (John Wiley & Sons, Inc., 2006).

77. Milov, A. D., Ponomarev, A. B. & Tsvetkov, Y. D. Electron electron double-resonance in electron-spin echo - model biradical systems and the sensitized photolysis of decalin. *Chem. Phys. Lett.* **110,** 67–72 (1984).

78. Altenbach, C., Kusnetzow, A. K., Ernst, O. P., Hofmann, K. P. & Hubbell, W. L. High-resolution distance mapping in rhodopsin reveals the pattern of helix movement due to activation. *Proc. Natl. Acad. Sci. U. S. A.* **105,** 7439–44 (2008).

79. Lin, A. Y., Prochniewicz, E., James, Z. M., Svensson, B. & Thomas, D. D. Large-scale opening of utrophin's tandem calponin homology (ch) domains upon actin binding by an induced-fit mechanism. *Proc. Natl. Acad. Sci. U. S. A.* **108,** 12729–33 (2011).

80. Colson, B. A., Thompson, A. R., Espinoza-Fonseca, L. M. & Thomas, D. D. Site-directed spectroscopy of cardiac myosin-binding protein C reveals effects of phosphorylation on protein structural dynamics. *Proc. Natl. Acad. Sci. U. S. A.* **113,** 3233–8 (2016).

81. Emshwiller, M., Hahn, E. L. & Kaplan, D. Pulsed nuclear resonance spectroscopy. *Phys. Rev.* **118,** 414–24 (1960).

82. Pannier, M., Veit, S., Godt, A., Jeschke, G. & Spiess, H. W. Dead-time free measurement of dipole-dipole interactions between electron spins. *J. Magn. Reson.* **142,** 331–340 (2000).

83. Sale, K., Sar, C., Sharp, K. A., Hideg, K. & Fajer, P. G. Structural determination of spin label immobilization and orientation: a Monte Carlo minimization approach. *J. Magn. Reson.* **156,** 104–12 (2002).

84. Fajer, P., Fajer, M., Zawrotny, M. & Yang, W. Full atom simulations of spin label conformations. *Methods Enzymol.* **563,** 623–42 (2015).

85. Karim, C. B., Zhang, Z. & Thomas, D. D. Synthesis of TOAC spin-labeled proteins and reconstitution in lipid membranes. *Nat. Protoc.* **2,** 42–9 (2007).

86. Berliner, L. J., Grunwald, J., Hankovszky, H. O. & Hideg, K. A novel reversible thiol-specific spin label: papain active site labeling and inhibition. *Anal. Biochem.* **119,** 450–5 (1982).

87. Fawzi, N. L. *et al.* A rigid disulfide-linked nitroxide side chain simplifies the quantitative analysis of PRE data. *J. Biomol. NMR* **51,** 105–14 (2011).

88. Wilcox, M., Parce, J., Thomas, M. & Lyles, D. A new bifunctional spin-label suitable for saturation-transfer EPR studies of protein rotational motion. *Biochemistry* **29,** 5734–43 (1990).

89. Losel, R. M., Philipp, R., Kalai, T., Hideg, K. & Trommer, W. E. Synthesis and application of novel bifunctional spin labels. *Bioconjug. Chem.* **10,** 578–82 (1999).

90. Arata, T, Aihara, T, Ueda, K, Nakamura, M & Ueki, S. Calcium structural transition of troponin in the complexes, on the thin filament, and in muscle fibres, as studied by site-directed spin-labelling EPR. *Adv. Exp. Med. Biol.* **592,** 125–35 (2007).

91. Kalai, T., Balog, M., Jeko, J. & Hideg, K. Synthesis and reactions of a symmetric paramagnetic pyrrolidine diene. *Synthesis,* 973–980 (1999).

92. Thompson, A. R., Naber, N., Wilson, C., Cooke, R. & Thomas, D. D. Structural dynamics of the actomyosin complex probed by a bifunctional spin label that cross-links SH1 and SH2. *Biophys. J.* **95,** 5238–46 (2008).

93. Moen, R. J., Thomas, D. D. & Klein, J. C. Conformationally trapping the actin-binding cleft of myosin with a bifunctional spin label. *J. Biol. Chem.* **288,** 3016–24 (2013).

94. Fleissner, M. R. *et al.* Structure and dynamics of a conformationally constrained nitroxide side chain and applications in EPR spectroscopy. *Proc. Natl. Acad. Sci. U. S. A.* **108,** 16241–6 (2011).

95. Islam, S. M. & Roux, B. Simulating the distance distribution between spin-labels attached to proteins. *J. Phys. Chem. B* **119,** 3901–11 (2015).

96. Vanea, E., Gruian, C., Rickert, C., Steinhoff, H. J. & Simon, V. Structure and dynamics of spin-labeled insulin entrapped in a silica matrix by the sol-gel method. *Biomacromolecules* **14,** 2582–92 (2013).

97. Sahu, I. D. *et al.* DEER EPR measurements for membrane protein structures via bifunctional spin labels and lipodisq nanoparticles. *Biochemistry* **52,** 6627–32 (2013).

98. Preller, M. & Manstein, D. J. Myosin structure, allostery, and mechano-chemistry. *Structure* **21,** 1911–22 (2013).

99. Thomas, D. D., Prochniewicz, E. & Roopnarine, O. Changes in actin and myosin structural dynamics due to their weak and strong interactions. *Results Probl. Cell Differ.* **36,** 7–19 (2002).

100. Spudich, J. A. Hypertrophic and dilated cardiomyopathy: four decades of basic research on muscle lead to potential therapeutic approaches to these devastating genetic diseases. *Biophys. J.* **106,** 1236–49 (2014).

101. Thomas, D. D., Kast, D. & Korman, V. L. Site-directed spectroscopic probes of actomyosin structural dynamics. *Annu. Rev. Biophys.* **38,** 347–69 (2009).

102. Thomas, D. D., Muretta, J. M., Colson, B. A., Mello, R. N. & Kast, D. in *Comprehensive Biophysics* 226–250 (Elsevier, 2012).

103. Thomas, D. D., Ishiwata, S., Seidel, J. C. & Gergely, J. Sub-millisecond rotational dynamics of spin-labeled myosin heads in myofibrils. *Biophys. J.* **32,** 873–89 (1980).

104. Cooke, R., Crowder, M. S. & Thomas, D. D. Orientation of spin labels attached to cross-bridges in contracting muscle fibres. *Nature* **300,** 776–8 (1982).

105. Ostap, E. M., Barnett, V. A. & Thomas, D. D. Resolution of three structural states of spin-labeled myosin in contracting muscle. *Biophys. J.* **69,** 177–88 (1995).

106. McHaourab, H. S., Kalai, T., Hideg, K. & Hubbell, W. L. Motion of spin-labeled side chains in T4 lysozyme: effect of side chain structure. *Biochemistry* **38,** 2947–55 (1999).

107. Corrie, J. E. *et al.* Dynamic measurement of myosin light-chain-domain tilt and twist in muscle contraction. *Nature* **400,** 425–30 (1999).

108. Hopkins, S. C. *et al.* Orientation changes of the myosin light chain domain during filament sliding in active and rigor muscle. *J. Mol. Biol.* **318,** 1275–91 (2002).

109. Forkey, J. N., Quinlan, M. E., Shaw, M. A., Corrie, J. E. & Goldman, Y. E. Three-dimensional structural dynamics of myosin V by single-molecule fluorescence polarization. *Nature* **422,** 399–404 (2003).

110. Pace, C. J. *et al.* A flash-tetracysteine assay for quantifying the association and orientation of transmembrane alpha-helices. *Chembiochem* **12,** 1018–22 (2011).

111. Nesmelov, Y. E. *et al.* Structural kinetics of myosin by transient time-resolved FRET. *Proc. Natl. Acad. Sci. U. S. A.* **108,** 1891–6 (2011).

112. Fajer, P. G., Bennett, R. L. H., Polnaszek, C. F., Fajer, E. A. & Thomas, D. D. General method for multiparameter fitting of high-resolution EPR spectra using a simplex algorithm. *J. Magn. Res.* **88,** 111–25 (1990).

113. Enkhbayar, P., Damdinsuren, S., Osaki, M. & Matsushima, N. Helfit: helix fitting by a total least squares method. *Comput. Biol. Chem.* **32,** 307–310 (2008).

114. Holmes, K. C., Angert, I., Kull, F. J., Jahn, W. & Schroder, R. R. Electron cryo-microscopy shows how strong binding of myosin to actin releases nucleotide. *Nature* **425,** 423–7 (2003).

115. Fisher, A. J. *et al.* X-ray structures of the myosin motor domain of Dictyostelium discoideum complexed with MgADP.BeFx and MgADP.AlF4. *Biochemistry* **34,** 8960–72. (1995).

116. Smith, C. A. & Rayment, I. X-ray structure of the magnesium(II).ADP.vanadate complex of the Dictyostelium discoideum myosin motor domain to 1.9 Åresolution. *Biochemistry* **35,** 5404–17 (1996).

117. Bauer, C. B., Holden, H. M., Thoden, J. B., Smith, R. & Rayment, I. X-ray structures of the apo and MgATP-bound states of Dictyostelium discoideum myosin motor domain. *J. Biol. Chem.* **275,** 38494–9 (2000).

118. Columbus, L. & Hubbell, W. L. Mapping backbone dynamics in solution with site-directed spin labeling: GCN4-58 bZip free and bound to DNA. *Biochemistry* **43,** 7273–87 (2004).

119. Greene, L. E. & Eisenberg, E. Dissociation of the actin.subfragment 1 complex by adenyl-5'-yl imidodiphosphate, ADP, and PPi. *J. Biol. Chem.* **255,** 543–8 (1980).

120. Ritchie, M. D., Geeves, M. A., Woodward, S. K. & Manstein, D. J. Kinetic characterization of a cytoplasmic myosin motor domain expressed in Dictyostelium discoideum. *Proc. Natl. Acad. Sci. U. S. A.* **90,** 8619–23 (1993).

121. Iorga, B., Adamek, N. & Geeves, M. A. The slow skeletal muscle isoform of myosin shows kinetic features common to smooth and non-muscle myosins. *J. Biol. Chem.* **282,** 3559–70 (2007).

122. Albet-Torres, N. *et al.* Drug effect unveils inter-head cooperativity and strain-dependent ADP release in fast skeletal actomyosin. *J. Biol. Chem.* **284,** 22926–37 (2009).

123. Nyitrai, M. & Geeves, M. A. Adenosine diphosphate and strain sensitivity in myosin motors. *Philos. Trans. R. Soc. Lond. B. Biol. Sci.* **359,** 1867–77 (2004).

124. Whittaker, M. *et al.* A 35-a movement of smooth muscle myosin on ADP release. *Nature* **378,** 748–51 (1995).

125. Traaseth, N. J. *et al.* Spectroscopic validation of the pentameric structure of phospholamban. *Proc. Natl. Acad. Sci. U. S. A.* **104,** 14676–81 (2007).

126. Korman, V. L., Anderson, S. E., Prochniewicz, E., Titus, M. A. & Thomas, D. D. Structural dynamics of the actin-myosin interface by site-directed spectroscopy. *J. Mol. Biol.* **356,** 1107–17 (2006).

127. Prochniewicz, E. *et al.* Functional, structural, and chemical changes in myosin associated with hydrogen peroxide treatment of skeletal muscle fibers. *Am. J. Physiol. Cell Physiol.* **294,** C613–26 (2008).

128. Prochniewicz, E., Walseth, T. F. & Thomas, D. D. Structural dynamics of actin during active interaction with myosin: different effects of weakly and strongly bound myosin heads. *Biochemistry* **43,** 10642–52 (2004).

129. Prochniewicz, E. *et al.* Myosin isoform determines the conformational dynamics and cooperativity of actin filaments in the strongly bound actomyosin complex. *J. Mol. Biol.* **396,** 501–9 (2010).

130. De La Cruz, E. M. & Ostap, E. M. Kinetic and equilibrium analysis of the myosin ATPase. *Methods Enzymol.* **455,** 157–92 (2009).

131. Humphrey, W., Dalke, A. & Schulten, K. VMD: Visual Molecular Dynamics. *J. Mol. Graph. Model.* **14,** 33–38 (1996).

132. Huxley, H. E. The mechanism of muscular contraction. *Science* **164,** 1356–65 (1969).

133. Thomas, D. D., Ramachandran, S., Roopnarine, O., Hayden, D. W. & Ostap, E. M. The mechanism of force generation in myosin: a disorder-to-order transition, coupled to internal structural changes. *Biophys. J.* **68,** 135S–141S (1995).

134. Tanner, J. W., Thomas, D. D. & Goldman, Y. E. Transients in orientation of a fluorescent cross-bridge probe following photolysis of caged nucleotides in skeletal muscle fibres. *J. Mol. Biol.* **223,** 185–203 (1992).

135. Columbus, L. & Hubbell, W. L. A new spin on protein dynamics. *Trends Biochem. Sci.* **27,** 288–95 (2002).

136. Thompson, A. R., Binder, B. P., McCaffrey, J. E., Svensson, B. & Thomas, D. D. Bifunctional spin labeling of muscle proteins: accurate rotational dynamics, orientation, and distance by EPR. *Methods Enzymol.* **564,** 101–23 (2015).

137. Binder, B. P., Cornea, S., Thompson, A. R., Moen, R. J. & Thomas, D. D. High-resolution helix orientation in actin-bound myosin determined with a bifunctional spin label. *Proc. Natl. Acad. Sci. U. S. A.* **112,** 7972–7 (2015).

138. Harwood, A. J., Plyte, S. E., Woodgett, J, Strutt, H & Kay, R. R. Glycogen synthase kinase 3 regulates cell fate in Dictyostelium. *Cell* **80,** 139–148 (1995).

139. Prochniewicz, E., Zhang, Q., Janmey, P. A. & Thomas, D. D. Cooperativity in F-actin: binding of gelsolin at the barbed end affects structure and dynamics of the whole filament. *J. Mol. Biol.* **260,** 756–66 (1996).

140. Jeschke, G. *et al.* DeerAnalysis2006—a comprehensive software package for analyzing pulsed ELDOR data. *Appl. Magn. Reson.* **30,** 473–498 (2006).

141. MATLAB. *Version 7.10.0 (r2014a)* (The MathWorks Inc., 2014).

142. Schrödinger, LLC. The PyMOL molecular graphics system, version 1.8 (2015).

143. Pettersen, E. F. *et al.* UCSF Chimera–a visualization system for exploratory research and analysis. *J. Comput. Chem.* **25,** 1605–1612 (2004).

144. Jones, E., Oliphant, T., Peterson, P., *et al.* SciPy: open source scientific tools for Python (2001).

145. Van der Walt, S., Colbert, S. C. & Varoquaux, G. The NumPy array: a structure for efficient numerical computation. *Computing in Science Engineering* **13,** 22–30 (2011).

146. Rayment, I. *et al.* Three-dimensional structure of myosin subfragment-1: a molecular motor. *Science* **261,** 50–8. (1993).

147. Arnold, K., Bordoli, L., Kopp, J. & Schwede, T. The SWISS-MODEL workspace: a web-based environment for protein structure homology modelling. *Bioinformatics* **22,** 195–201 (2006).

148. Guex, N., Peitsch, M. C. & Schwede, T. Automated comparative protein structure modeling with SWISS-MODEL and Swiss-PdbViewer: a historical perspective. *Electrophoresis* **30,** S162–S173 (2009).

149. Kiefer, F., Arnold, K., Knzli, M., Bordoli, L. & Schwede, T. The SWISS-MODEL repository and associated resources. *Nucleic Acids Res.* **37,** D387–D392 (2009).

150. Biasini, M. *et al.* SWISS-MODEL: modelling protein tertiary and quaternary structure using evolutionary information. *Nucleic Acids Res.* **42,** W252–W258 (2014).

151. Coureux, P.-D., Sweeney, H. L. & Houdusse, A. Three myosin V structures delineate essential features of chemo-mechanical transduction. *EMBO J.* **23,** 4527–4537 (2004).

152. Emsley, P., Lohkamp, B., Scott, W. G. & Cowtan, K. Features and development of Coot. *Acta Crystallogr. D Biol. Crystallogr.* **66,** 486–501 (2010).

153. McCaffrey, J. E., James, Z. M., Svensson, B., Binder, B. P. & Thomas, D. D. A bifunctional spin label reports the structural topology of phospholamban in magnetically-aligned bicelles. *J. Magn. Reson.* **262,** 50–56 (2016).

154. Bloemink, M. J., Deacon, J. C., Resnicow, D. I., Leinwand, L. A. & Geeves, M. A. The superfast human extraocular myosin is kinetically distinct from the fast skeletal IIa, IIb, and IId isoforms. *J. Biol. Chem.* **288,** 27469–27479 (2013).

155. Jana, B. & Onuchic, J. N. Strain mediated adaptation is key for myosin mechanochemistry: discovering general rules for motor activity. *PLoS Comput. Biol.* **12,** e1005035 (2016).

156. Cremo, C. R. & Geeves, M. A. Interaction of actin and ADP with the head domain of smooth muscle myosin: implications for strain-dependent ADP release in smooth muscle. *Biochemistry* **37,** 1969–78 (1998).

157. Conibear, P. B. Kinetic studies on the effects of adp and ionic strength on the interaction between myosin subfragment-1 and actin: implications for load-sensitivity and regulation of the crossbridge cycle. *J. Muscle Res. Cell Motil.* **20,** 727–742 (1999).

158. Coureux, P. D. *et al.* A structural state of the myosin V motor without bound nucleotide. *Nature* **425,** 419–23 (2003).

159. Mnnich, S., Pathan-Chhatbar, S. & Manstein, D. J. Crystal structure of the rigor-like human non-muscle myosin-2 motor domain. *FEBS Lett.* **588,** 4754–4760 (2014).

160. Sun, M., Rose, M. B., Ananthanarayanan, S. K., Jacobs, D. J. & Yengo, C. M. Characterization of the pre-force-generation state in the actomyosin cross-bridge cycle. *Proc. Natl. Acad. Sci. U. S. A.* **105,** 8631–8636 (2008).

161. Sun, M. *et al.* Dynamics of the upper 50-kda domain of myosin V examined with fluorescence resonance energy transfer. *J. Biol. Chem.* **281,** 5711–5717 (2006).

162. Kurzawa, S. E., Manstein, D. J. & Geeves, M. A. Dictyostelium discoideum myosin II: characterization of functional myosin motor fragments. *Biochemistry* **36,** 317–323 (1997).

163. Woodward, S. K., Geeves, M. A. & Manstein, D. J. Kinetic characterization of the catalytic domain of Dictyostelium discoideum myosin. *Biochemistry* **34,** 16056–16064 (1995).

164. Batra, R, Geeves, M. A. & Manstein, D. J. Kinetic analysis of dictyostelium discoideum myosin motor domains with glycine-to-alanine mutations in the reactive thiol region. *Biochemistry* **38,** 6126–6134 (1999).

165. Roux, B. & Islam, S. M. Restrained-ensemble molecular dynamics simulations based on distance histograms from double electron-electron resonance spectroscopy. *J. Phys. Chem. B* **117,** 4733–4739 (2013).

166. Islam, S. M., Stein, R. A., McHaourab, H. S. & Roux, B. Structural refinement from restrained-ensemble simulations based on EPR/DEER data: application to T4 lysozyme. *J. Phys. Chem. B* **117,** 4740–4754 (2013).

167. Moore, J. R., Leinwand, L. & Warshaw, D. M. Understanding cardiomyopathy phenotypes based on the functional impact of mutations in the myosin motor. *Circ. Res.* **111,** 375–385 (2012).

168. Lopes, L. R. & Elliott, P. M. A straightforward guide to the sarcomeric basis of cardiomyopathies. *Heart* **100,** 1916–1923 (2014).

169. Fujita, H *et al.* Characterization of mutant myosins of Dictyostelium discoideum equivalent to human familial hypertrophic cardiomyopathy mutants. Molecular force level of mutant myosins may have a prognostic implication. *J. Clin. Invest.* **99,** 1010–1015 (1997).

170. Fujita, H, Sugiura, S, Momomura, S, Sugi, H & Sutoh, K. Functional characterization of Dictyostelium discoideum mutant myosins equivalent to human familial hypertrophic cardiomyopathy. *Adv. Exp. Med. Biol.* **453,** 131–137 (1998).

171. Teerlink, J. R. A novel approach to improve cardiac performance: cardiac myosin activators. *Heart Fail. Rev.* **14,** 289–298 (2009).

172. Malik, F. I. *et al.* Cardiac myosin activation: a potential therapeutic approach for systolic heart failure. *Science* **331,** 1439–1443 (2011).

173. Katayama, T. *et al.* Stimulatory effects of arachidonic acid on myosin ATPase activity and contraction of smooth muscle via myosin motor domain. *Am. J. Physiol. Heart Circ. Physiol.* **298,** H505–H514 (2010).

174. Green, E. M. *et al.* A small-molecule inhibitor of sarcomere contractility suppresses hypertrophic cardiomyopathy in mice. *Science* **351,** 617–621 (2016).

175. Winkelmann, D. A., Forgacs, E., Miller, M. T. & Stock, A. M. Structural basis for drug-induced allosteric changes to human beta-cardiac myosin motor activity. *Nat. Commun.* **6,** 7974 (2015).

176. Ling, N, Shrimpton, C, Sleep, J, Kendrick-Jones, J & Irving, M. Fluorescent probes of the orientation of myosin regulatory light chains in relaxed, rigor, and contracting muscle. *Biophys. J.* **70,** 1836–1846 (1996).

177. Traaseth, N. J., Buffy, J. J., Zamoon, J. & Veglia, G. Structural dynamics and topology of phospholamban in oriented lipid bilayers using multidimensional solid-state NMR. *Biochemistry* **45,** 13827–13834 (2006).

178. Ghimire, H. *et al.* Probing the helical tilt and dynamic properties of membrane-bound phospholamban in magnetically aligned bicelles using electron paramagnetic resonance spectroscopy. *Biochim. Biophys. Acta* **1818,** 645–650 (2012).

179. Durr, U. H. N., Soong, R. & Ramamoorthy, A. When detergent meets bilayer: birth and coming of age of lipid bicelles. *Prog. Nucl. Magn. Reson. Spectrosc.* **69,** 1–22 (2013).

180. McCaffrey, J. E., James, Z. M. & Thomas, D. D. Optimization of bicelle lipid composition and temperature for EPR spectroscopy of aligned membranes. *J. Magn. Reson.* **250,** 71–5 (2015).

181. Abragam, A. & Bleaney, B. *Electron paramagnetic resonance of transition ions* (Oxford University Press, 2012).

182. Schweiger, A. & Jeschke, G. *Principles of pulse electron paramagnetic resonance* (Oxford University Press, 2001).

APPENDIX A: DERIVATION OF THE EFFECTS OF NITROXIDE ORIENTATION ON THE EPR RESONANCE CONDITION

A.1 Introduction

In Section 3.2, the functions $g(\theta_{NB}, \phi_{NB})$ and $A(\theta_{NB}, \phi_{NB})$ were introduced to describe the orientation dependence of the effective g and A tensors (Equations 3.7a and 3.7b). These functions are of fundamental importance in the present work, where all analysis of EPR data from oriented fibers depends on the accurate derivation of θ_{NB} and ϕ_{NB} from least-squares fitting of a simulated spectrum to experimental data. In the following appendix, a full derivation of these functions is presented, and discussed in the context of building spectral simulations.

A.2 Representing Tensor Anisotropy

Recall from Section 3.2 that the g-factor (g) and hyperfine coupling constant (A) are actually second-rank tensors. Each may be represented by a 3x3 matrix, which becomes diagonal when considered in the *nitroxide frame* (also defined in Section 3.2) and displays its principle axis values along the diagonal. Because both tensors are anisotropic, determining the effective g and A values that give rise to unique resonance conditions in an EPR experiment requires defining the spatial relationship between the nitroxide frame and the external field.

Recall from Section 3.2 that the arbitrary reference frame used in modeling the EPR experiment is constructed by convention so that the external magnetic field vector $\vec{B}$ lies

along the positive z-axis. This reference frame will be referred to as the *laboratory frame*. When the laboratory and nitroxide frames are coincident, the matrix representations of g and A in the laboratory frame are diagonal:

$$g = \begin{bmatrix} g'_{xx} & 0 & 0 \\ 0 & g'_{yy} & 0 \\ 0 & 0 & g'_{zz} \end{bmatrix} \qquad A = \begin{bmatrix} A'_{xx} & 0 & 0 \\ 0 & A'_{yy} & 0 \\ 0 & 0 & A'_{zz} \end{bmatrix} \tag{A.1}$$

In general, of course, the nitroxide and laboratory frames have arbitrary orientation with respect to one another. General representations of the tensors in the laboratory frame can be obtained by employing the relation

$$g = Lg'L^{-1} \qquad A = LA'L^{-1} \tag{A.2}$$

where primes indicate the diagonal representations of the tensors, and L is the transformation matrix required to transform a vector representation from the nitroxide frame to the laboratory frame [73]. The matrix L is defined by a set of angles that relates the two coordinate systems, and three angles are required to define an unambiguous coordinate transformation in three dimensions; in magnetic resonance, it has become common to use Euler angles defined in the ZYZ-convention for this purpose [71, 181, 182]. When composed using this convention, the matrix L has the form

$$L = \begin{bmatrix} \cos\gamma\cos\beta\cos\alpha - \sin\gamma\sin\alpha & \cos\gamma\cos\beta\sin\alpha + \sin\gamma\cos\alpha & -\cos\gamma\sin\beta \\ -\sin\gamma\cos\beta\cos\alpha - \cos\gamma\sin\alpha & -\sin\gamma\cos\beta\sin\alpha + \cos\gamma\sin\alpha & \sin\alpha\sin\beta \\ \sin\beta\cos\alpha & \sin\beta\sin\alpha & \cos\beta \end{bmatrix} \quad \text{(A.3)}$$

where (α, β, γ) correspond to rotations applied about the z-axis, rotated y-axis, and rotated z-axis of the nitroxide frame, in that order.

Assuming at least one of the Euler angles is nonzero, the transformed g and A matrices will no longer be diagonal, and each of their components will consist of a mixture of principle axis values weighted by sines and cosines of the Euler angles. In general:

$$g = \begin{bmatrix} g_{xx} & g_{yx} & g_{zx} \\ g_{xy} & g_{yy} & g_{zy} \\ g_{xz} & g_{yz} & g_{zz} \end{bmatrix} \qquad A = \begin{bmatrix} A_{xx} & A_{yx} & A_{zx} \\ A_{xy} & A_{yy} & A_{zy} \\ A_{xz} & A_{yz} & A_{zz} \end{bmatrix} \quad \text{(A.4)}$$

A.3 The Effective g Value

Having thus obtained representations for both tensors in the laboratory frame, it is now possible to assess their effect on the resonance condition. Consider first the Zeeman interaction in the absence of hyperfine coupling. Recall from 3.2 that the Zeeman interaction energy of an electron spin with an external magnetic field is given by

$$E = -\vec{B}\cdot\vec{\mu}_s = -\vec{B}\cdot(\gamma\cdot\hat{\vec{S}}) = -\vec{B}\cdot\left(\frac{-\mu_B g}{\hbar}\cdot\hat{\vec{S}}\right) = -\left(\frac{-\mu_B}{\hbar}\right)\left(\vec{B}\cdot g\cdot\hat{\vec{S}}\right) \quad \text{(A.5)}$$

Note here that g is not treated like a scalar, as it was in Section 3.2, because we are now

considering g as a 3x3 matrix. $\vec{B} \equiv \begin{bmatrix} 0 & 0 & B_0 \end{bmatrix}$ and $\hat{\vec{S}} \equiv \begin{bmatrix} 0 & 0 & \hat{S}_z \end{bmatrix} = \begin{bmatrix} 0 & 0 & m_s\hbar \end{bmatrix}$ were defined in detail in 3.2, based on the assumption that the electron spin is quantized along the axis of $\vec{B}$; g in the laboratory frame is defined by Equation A.2. Performing the requisite matrix multiplication, we obtain:

$$\vec{B} \cdot g \cdot \hat{\vec{S}} = \begin{bmatrix} 0 & 0 & B_0 \end{bmatrix} \cdot \begin{bmatrix} g_{xx} & g_{yx} & g_{zx} \\ g_{xy} & g_{yy} & g_{zy} \\ g_{xz} & g_{yz} & g_{zz} \end{bmatrix} \cdot \begin{bmatrix} 0 \\ 0 \\ m_s\hbar \end{bmatrix} = B_0 g_{zz} m_s \hbar \tag{A.6}$$

Derivation of the Zeeman-induced resonance condition here follows the same steps as in Equations 3.4 and 3.5:

$$\vec{\mu}_s = -\left(\frac{-\mu_B}{\hbar}\right)(B_0 g_{zz} m_s \hbar) \implies E = m_s \mu_B B_0 g_{zz} \tag{A.7a}$$

$$\implies \Delta E = \mu_B B_0 g_{zz} \tag{A.7b}$$

$$\implies B_{\text{res}} = \frac{h\nu}{g_{zz}\mu_B} \tag{A.7c}$$

Thus, the only component of g that renders an effect on the EPR resonance condition is the zz-component of the transformed g tensor; in other words, $g_{\text{eff}} = g_{zz}$.

By explicitly performing the transformation prescribed in Equation A.2, the value of g_{zz} is obtained in terms of the principle g values and Euler angles:

$$g_{\text{eff}} = g_{zz} = g'_{xx} \sin^2\beta \cos^2\alpha + g'_{yy} \sin^2\beta \sin^2\alpha + g'_{zz} \cos^2\beta \tag{A.8}$$

Note that although L is defined using three Euler angles (α, β, γ), the value of g_{zz} only depends on α and β. This makes sense, because the rotation by γ in the ZYZ-convention spins the nitroxide frame about its local z-axis, which will not affect the value of any component of the nitroxide z-axis in the laboratory frame.

Up until now, this derivation has considered spatial relationships using the laboratory frame as the chosen frame of reference; this was done to provide the most straightforward derivation of the effective g value. It is easy to consider everything from the perspective of a fixed nitroxide frame, however: Equation A.8 can be rewritten in terms of the polar angles θ_{NB} and ϕ_{NB}, which describe the orientation of the magnetic field vector $\vec{B}$ in the nitroxide frame. Angles α and β will always have equivalent magnitude to ϕ_{NB} and θ_{NB}, respectively, and thus direct substitution yields the form presented in Equation 3.7a:

$$g_{\text{eff}} = g(\theta_{NB}, \phi_{NB}) = g'_{xx} \sin^2 \theta_{NB} \cos^2 \phi_{NB} + g'_{yy} \sin^2 \theta_{NB} \sin^2 \phi_{NB} + g'_{zz} \cos^2 \theta_{NB} \qquad \text{(A.9)}$$

A.4 The Effective A Value

Next, consider the nuclear hyperfine interaction. Section 3.2 outlined how hyperfine coupling splits the resonance of a nitroxide radical into three distinct conditions, each offset by a value of $m_I A$. In order to derive the orientation dependence of the effective A value, it is necessary to take a brief step back and examine the source of this contribution. The

Hamiltonian for the hyperfine interaction between an electron and a nucleus is written

$$\mathcal{H}_{\mathrm{HF}} = \hat{\vec{S}} \cdot A \cdot \hat{\vec{I}} \tag{A.10}$$

where $\hat{\vec{I}}$ is the nuclear spin operator [71]. We can begin by treating the nuclear spin operator in the same manner as the electron spin operator was treated above, neglecting the transverse components by making the assumption that the nuclear spin is quantized along the axis of $\vec{B}$, which is valid in the high field limit. Thus, $\hat{\vec{I}} \equiv \left[0\ 0\ \hat{I}_z\right] = \left[0\ 0\ m_I\hbar\right]$. Then, if A is treated like a scalar, as it was in Section 3.2, the Hamiltonian reduces to $m_s m_I A$ (the $\hbar$ terms serve as conversions and may be eliminated by expressing A in appropriate units) and therefore the hyperfine contribution to the energy gap between the $m_s = +½$ and the $m_s = -½$ is $m_I A$. When A is instead considered as a tensor, simplification has a similar result to the case involving g, outlined above:

$$\hat{\vec{S}} \cdot A \cdot \hat{\vec{I}} \quad = \quad \begin{bmatrix} 0 & 0 & m_s\hbar \end{bmatrix} \cdot \begin{bmatrix} A_{xx} & A_{yx} & A_{zx} \\ A_{xy} & A_{yy} & A_{zy} \\ A_{xz} & A_{yz} & A_{zz} \end{bmatrix} \cdot \begin{bmatrix} 0 \\ 0 \\ m_I\hbar \end{bmatrix} \quad = \quad m_s m_I A_{zz} \tag{A.11}$$

Thus, it appears that (just as with g), the only value in the A tensor necessary for calculating the resonance condition is A_{zz}, and therefore

$$A_{\mathrm{eff}} = A_{zz} = A'_{xx}\sin^2\beta\cos^2\alpha + A'_{yy}\sin^2\beta\sin^2\alpha + A'_{zz}\cos^2\beta \tag{A.12}$$

In practice, however, it is found that while the approximations made so far to simplify the Zeeman and hyperfine Hamiltonians produce negligible deviations in the calculated value of g_{eff}, the calculated and experimentally-determined values of A_{eff} can vary by as much as 4 G, which has a significant impact on spectral lineshape [73]. Therefore, it is standard to employ a more complex approximation for A_{eff}. The transverse components of the electron spin operator are still neglected, but the Hamiltonian is allowed to include all components of the nuclear spin operator, such that $\hat{\vec{I}} \equiv [\hat{I}_x \ \hat{I}_y \ \hat{I}_z]$. The resulting Hamiltonian is more complex, but the effective value of A that appears in the final expression for electron spin state energy still reduces to a function of the principle axis values of A, and the same two Euler angles:

$$A_{\text{eff}} = \sqrt{{A'_{xx}}^2 \sin^2\beta\cos^2\alpha + {A'_{yy}}^2 \sin^2\beta\sin^2\alpha + {A'_{zz}}^2\cos^2\beta} \tag{A.13}$$

This approximation is significantly more accurate, exhibiting variation from the experimental result by less than 0.1 G for nitroxides at X-band frequencies [73].

Just as before, this relationship may be considered from the perspective of a fixed nitroxide frame, where α is equivalent to ϕ_{NB}, and β is equivalent to θ_{NB}. Thus, the desired function for A_{eff} is obtained in terms of ϕ_{NB} and θ_{NB} (analogous to Equation 3.7b):

$$\begin{aligned} A_{\text{eff}} &= A(\theta_{NB}, \phi_{NB}) \\ &= \sqrt{{A'_{xx}}^2 \sin^2\theta_{NB}\cos^2\phi_{NB} + {A'_{yy}}^2 \sin^2\theta_{NB}\sin^2\phi_{NB} + {A'_{zz}}^2\cos^2\theta_{NB}} \end{aligned} \tag{A.14}$$

A.5 Practical Considerations

Before concluding this section, it is useful to consider how these relationships actually inform least-squares fitting of experimental EPR spectra. Remember that all equations presented in this section apply to EPR spectra of strongly immobilized molecules, with no significant nanosecond motion. The derivation presented above demonstrates that the calculation of resonance positions depends on several parameters, namely: the microwave frequency, ν; the principle axis values of g and A; and the angles θ_{NB} and ϕ_{NB}, which describe the orientation of the spin system relative to the external magnetic field.

When considering an oriented sample, the principle tensor values can be determined experimentally by directing the magnetic field along each of the molecular axes in turn, though such experiments require a pure crystalline sample ordered in all three dimensions [73, 74]. In practice, these values are often included as simulation variables in the simulated fitting of spectra from dry powder samples (or, in the equivalent context of the current work, samples consisting of a minced muscle fiber in a flat cell). Simulation of a powder spectrum requires an even smaller parameter space than that of an oriented sample, because a uniform random orientational distribution is assumed (eliminating θ_{NB} and ϕ_{NB}). Thus, the principle axis values for both g and A can be determined to a high degree of accuracy by powder spectrum fitting, allowing for their values in Equations A.9 and A.14 to be fixed *ab initio*.

As the microwave frequency is also well-defined in a given EPR experiment, the only variable parameters needed in the spectral fitting of resonance positions for a static, oriented

spin system are θ_{NB} and ϕ_{NB}. To calculate a full spectrum, resonance positions are convoluted with Gaussian and Lorentzian functions to represent homogeneous and inhomogeneous broadening, respectively; parameters specifying the width of these distributions are also typically allowed to vary in a simulated fit, as their values are dependent on the local environment of the spin system. In conclusion, however, it is remarkable how few variables are required in the simulated fitting of an unknown spectrum. When coupled with the acute sensitivity of the resonance positions to small changes in θ_{NB} and ϕ_{NB}, the resolving power of EPR may be fully appreciated.